עבודת גמר (תזה) לתואר
דוקטור לפילוסופיה

מוגשת למועצה המדעית של
מכון ויצמן למדע
רחובות, ישראל

Thesis for the degree
Doctor of Philosophy

Submitted to the Scientific Council of the
Weizmann Institute of Science
Rehovot, Israel

במתכונת "רגילה"
In a "Regular" Format

מאת
אלכסי ליאשנקו
המחלקה לפיסיקת חלקיקים

By
Alexey Lyashenko
Particle Physics Department

פתוח גלאי אור על בסיס הכפלה בגז רגישים בתחום הנראה

Development of gas-avalanche photomultipliers sensitive in the visible spectral range

מנחה: פרופ' עמוס ברסקין

Advisor: Prof. Amos Breskin

י"ט אייר תשס"ט

13 May, 2009

Summary

In this work we demonstrated, for the first time, the possibility of conceiving gas-avalanche photomultipliers (GPMs) for the visible spectral range, capable of operation at high multiplication gains, in a continuous (DC) mode. The novel GPMs combine thin-film alkali-antimonide photocathodes coupled to state-of-the-art cascaded gaseous electron multipliers.

These photon detectors, with single-photon sensitivity, have many attractive properties. Unlike vacuum PMTs, they operate at atmospheric pressure; this permits conceiving large-area detectors (up to m^2) with flat geometry; unlike vacuum, the gas multiplication provides immunity to high magnetic fields. The GPMs have a slower response (in the ns range), compared to PMTs, but a superior localization accuracy (~0.1mm for single photons with standard gas-detector readout). They naturally compete with solid-state detectors in size, possibly in noise characteristics, but not in quantum efficiency (QE). Their effective quantum efficiency is lower than that of vacuum devices, due to photoelectron losses by backscattering on gas molecules. Best expected values are about 80% of the vacuum QE ones.

The success of the present achievements, following a few decades of tedious R&D by numerous groups, is due, among others, to two major factors:

1. A better understanding and studies of the processes involved in the avalanche-ions transport and impact on the photocathodes, and
2. The breakthrough reached in this work in avalanche-ion blocking, without photoelectron losses, with novel cascaded hole-multipliers having patterned ion-defocusing electrodes.

Principal achievements:

A. Alkali-antimonide visible-sensitive photocathodes:

In the visible-sensitive GPM we employed alkali-antimonide photocathodes; they were laboratory-produced by chemical vapor deposition, suitable for large-area active surfaces. We found optimal conditions for producing high-QE (exceeding 50% in vacuum at 360-400 nm) K-Cs-Sb photocathodes, approaching sensitivity of the best industrially made ones. Other photocathodes, Cs-Sb and Na-K-Sb were produced and investigated.

B. Ion-induced secondary electron emission (IISEE) from alkali-antimonide photocathodes

Alkali-antimonide photocathodes have low emission threshold; therefore, operating under gas avalanche, theey are susceptible to ion-induced secondary-electron emission (IISEE), resulting in ion-feedback effects (secondary avalanches), imposing severe limits on the maximum reachable gains. Comprehensive studies of the photocathodes operation under gas-avalanche multiplication, performed in this work, yielded the absolute values of the IISEE coefficients (γ_+^{eff}= 0.02-0.03) for the three photocathode materials investigated. These permitted setting the necessary limits for the ion backflow fraction (IBF) to the photocathode, necessary for a feedback-free operation at GPM gains of 10^5 (needed for single-photon sensitivity). The resulting estimated IBF-value for stable operation in a continuous mode in Ar/5%CH4 is $3.3*10^{-4}$.

C. Electron multipliers with high ion-blocking capabilities

It was demonstrated that the required IBF value of $3*10^{-4}$ was reached with a three-element F-R-MHSP/GEM/MHSP cascaded electron multiplier operated in atmospheric-pressure Ar/CH_4 (95/5), at total gain of $\sim 10^5$. This record ion blocking, due to ion deflection by strip-electrodes patterned on hole-multipliers, was reached at full photoelectron collection efficiency.

D. High gain continuous-mode operation of visible-sensitive GPMs

This work proved for the first time, that a GPM with visible-sensitive bi-alkali photocathodes can be successfully operated in continuous mode, at gains suitable for single-photon imaging. A Visible-sensitive GPM with a F-R-MHSP/GEM/MHSP cascaded multiplier and a K_2CsSb photocathode, yielded, for the first time, stable operation at gains of 10^5 in continuous mode with full photoelectron collection efficiency and without any noticeable feedback effects. This validated our predicted necessary IBF values resulting from the IISEE measurements. The main goal of the research proposal - to combine thin-film photocathodes sensitive in visible-spectral range with fast cascaded micro-patterned gas avalanche multipliers sensitive to single charges - was therefore reached. This achievement can be considered as a major breakthrough in the field of photon detectors.

E. The GPM stability

A long-term stability under gas-avalanche conditions is naturally a concern for visible-sensitive GPMs. To avoid chemical degradation of the photocathodes, the detector components must be made of UHV-compatible materials; the detector must operate in sealed mode filled with an ultra-pure gases. In this work, the research has been carried out in difficult unsealed-detector conditions (detector placed within a large vacuum vessel). It was shown however that alkali-antimonide photocathodes are stable in ultra-pure gases for over a month period; by far better stability is expected in sealed devices. A deep concern was the photocathode's ageing under gas avalanche. Photocathode aging studies under avalanche-ion bombardment provided a basis for estimating the lifetime of visible-sensitive GPMs combining a F-R-MHSP/GEM/MHSP multiplier and a K_2CsSb photocathode. Our calculations indicate that a detector of this type will have a 20% QE decrease of its bialkali photocathode after an accumulated ion charge of ~2 $\mu C/mm^2$; this will however occur after ~40 years of constant operation under a gain of $\sim 10^5$ at a photon flux of 5 kHz/mm^2 (@ QE=30%). For comparison, in a GPM with a 4-GEM multiplier (IBF~$3*10^{-2}$) for the same operation conditions, the 20% PC aging will occur after ~150 days.

The extension of the present GPM concept towards large-area photon imaging detectors is a good challenge for industry. Large-area GPMs have many potential applications, particularly in large particle physics and astrophysics experiments; among them are imaging Cherenkov light and recording scintillation information; large-area photon detectors could be useful in medical imaging and in many other fields.

תקציר

בעבודה זו אנו מדגימים, בפעם הראשונה, יישום של מכפלי פוטונים מבוססי גז (Gaseous PhotoMultipliers - GPM) לתחום האור הנראה, המסוגלים לפעול בהגברה גבוהה, במצב DC. ה- GPM החדשני משלב פוטו-קתודות של אלקאלי-אנטימוניד (Alkali antimonide), מצומדות למכפל אלקטרונים רב-שלבי בגז.

לגלאי פוטונים אלו, הרגישים לפוטונים בודדים, יש תכונות אטרקטיביות רבות. בניגוד למכפלי-אור הפועלים בואקום (PhotoMultiplier Tubes-PMT), גלאים אלה פועלים בלחץ אטמוספרי, תכונה המאפשרת מימוש גלאים בעלי שטח פעיל רחב (מטר רבוע) בעלי גיאומטריה שטוחה. שלא כמו בואקום, הכפלת אלקטרונים בגז מעניקה חסינות בפני שדות מגנטיים גבוהים. ל- GPM יש תגובה איטית יותר (בתחום הננו-שניות) בהשוואה ל- PMT, אולם הינם מדוייקים יותר מבחינת מיקום מרחבי (כ- 0.1 מ"מ לפוטונים בודדים בשילוב עם אלקטרודות לקריאת האותות). הם מתחרים באופן טבעי בגלאי מצב-מוצק מבחינת גודל, ויתכן שאף מבחינת מאפייני הרעש, אולם לא מבחינת היעילות הקוונטית (QE). היעילות הקוונטית האפקטיבית שלהם נמוכה מזו של מכשירים הפועלים בואקום, בשל איבוד פוטו-אלקטרונים הנגרם מפיזורם לאחור ע"י מולקולות הגז. היעילות הקוונטית הגבוהה ביותר המצופה מGPM היא כ- 80% מזו של גלאים הפועלים בואקום.

ניתן לזקוף את ההצלחות שהושגו לאחרונה, אשר באו לאחר מספר עשורים של מחקר ופיתוח קדחתניים שבוצעו במספר קבוצות מחקר שונות, בעיקר לשני גורמים עיקריים:

1. מחקרים והבנה טובה יותר של התהליך המתרחש בעת מעבר היונים הנוצרים בתוך הגלאי תוך תהליך ההכפלה בגז, והשפעתם על הפוטוקתודות.
2. פריצת הדרך אשר הושגה בחסימת היונים הנוצרים בתהליך ההכפלה, ללא איבוד של פוטואלקטרונים. זאת בעזרת מספר שלבים של מכפלי אלקטרונים מחוררים חדשניים עליהם מוטבעות אלקטרודות המסיטות את היונים מהפוטוקתודה.

הישגים עיקריים

א. פוטוקתודות רגישות לאור נראה מאלקאלי אנטימונידים.

ב- GPM הרגיש לאור נראה השתמשנו בפוטו-קתודות העשויות מאלקאלי אנטימונידים.. הן יוצרו במעבדה ע"י ריבוץ כימי של אדים בואקום גבוה, תהליך המתאים ליצירת משטחים אקטיביים גדולים. מצאנו תנאים אופטימליים ליצירת פוטוקתודות העשויות מ- K-Cs-Sb בעלות יעילות קוונטית גבוהה (מעל 50% בואקום עבור אורכי גל בתחום 360-400 ננומטר). רגישות גבוהה זו מתקרבת לערכים הגבוהים ביותר שהושגו עד כה בתעשיה. כמו כן, יצרנו גם פוטוקתודות העשויות מ- Cs-Sb ומ- Na-K-Sb וחקרנו את ביצועיהן.

ב. פליטת אלקטרונים משנית הנגרמת מהיונים הפוגעים בפוטו-קתודות מאלקאלי אנטימונידים.

לפוטו-קתודות מאלקאלי אנטימונידים יש סף פליטת אלקטרונים נמוך. משום כך, בתהליך ההכפלה בגז, הן נוטות לפליטת אלקטרונים משנית הנגרמת מפגיעת היונים הנוצרים בהכפלה (Ion-induced secondary electron emission IISEE). כתוצאה מכך, מתרחש אפקט של משוב יוני (הכפלות משניות) המגביל משמעותית את ההגברה בה ניתן לפעול. בעבודה זו בוצע מחקר מעמיק של פוטוקתודות הפועלות בצמוד לתהליכי הכפלת אלקטרונים בגז, אשר הניב ערכים מוחלטים של מקדמי IISEE (γ_+^{eff}= 0.02-0.03) עבור שלושת החומרים שנבדקו לייצור פוטו-קתודות. ידיעת מקדמים אלה מאפשרת את קביעת החסמים על הזרימה של יונים לאחור (Ion Backflow Fraction-IBF) אל הפוטו-קתודה, הדרושים לפעולת ה- GPM ללא

משוב חוזר של יונים בהגברה של 10^5 (הדרושה לשם השגת רגישות לפוטונים בודדים). ערך ה- IBF המשוער לפעולה יציבה במצב DC בגז Ar/5% CH_4 הוא $3.3*10^{-4}$.

ג. מכפלי אלקטרונים החוסמים יונים ביעילות רבה

הדגמנו כי ניתן להשיג את ערך ה- IBF הדרוש של $3.3*10^{-4}$ באמצעות שלושה שלבים של מכפלי אלקטרונים מחוררים מהסוגים F-R-MHSP/GEM/MHSP הפועלים בגז Ar/CH_4 (95/5) בלחץ אטמוספרי בהגברה כוללת של כ- 10^5. שיא זה בחסימת יונים, הושג באמצעות הסטתם ע"י אלקטרודות בצורת פסים אשר הוטבעו על גבי מכפלי אלקטרונים מחוררים, וכל זאת תוך איסוף פוטו-אלקטרונים מלא.

ד. פעולת GPM הרגיש לתחום הנראה במצב DC בהגברה גבוהה

בעבודה זו הוכחנו לראשונה כי GPM בעל פוטו-קתודות בי-אלקאליות הרגישות לאור נראה, יכול לפעול בהצלחה במצב DC בהגברה המתאימה לגילוי של פוטונים בודדים. GPM הרגיש לאור נראה בעל שלושה מכפילי אלקטרונים מהסוגים F-R-MHSP/GEM/MHSP ופוטו-קתודה העשויה מ- K_2CsSb הופעל לראשונה באופן יציב בהגברה של 10^5 במצב DC ואיסוף פוטו-אלקטרונים מלא. זאת מבלי להבחין באפקטים של משוב יונים. תוצאה זו איששה את ערכי ה- IBF הנחוצים אשר צפינו ממדידות ה- IISEE. המטרה הראשית של הצעת המחקר - שילוב של פוטו-קתודות דקות הרגישות לאור נראה, ומצומדות לכמה שלבים של מכפלי אלקטרונים בגז הרגישים למטענים בודדים – הושגה לפיכך. הישג זה מהווה פריצת דרך חשובה בתחום גלאי הפוטונים.

ה. יציבות ה- GPM

פעולה יציבה לאורך זמן בתנאי הכפלת אלקטרונים בגז היא נקודה הראויה להתייחסות עבור GPM הרגישים לתחום הנראה. על מנת להמנע מבלאי כימי של הפוטו-קתודות, על חלקי הגלאי להיות עשויים מחומרים תואמי ואקום גבוה. על הגלאי לפעול כשהוא אטום ומלא בגז בטוהר גבוה. המחקר המוצג בעבודה זו נערך בתנאים קשים בגלאי שאינו אטום (הגלאי הורכב בתוך תא ואקום גדול). למרות זאת, הראינו כי פוטו-קתודות העשויות אלקאלי-אנטימוניד פועלות באופן יציב בגז טהור לאורך זמן ארוך מחודש. יציבות טובה בהרבה צפויה בתא אטום. קיים חשש מתהליכי הזדקנות של הפוטו-קתודה החשופה לתהליכי ההכפלה בגז. מחקרי הזדקנות של פוטו-קתודות אשר הופגזו ביונים סיפקו בסיס להערכה של זמן החיים של GPM רגיש לאור נראה המכיל מכפלי אלקטרונים מסוג F-R-MHSP/GEM/MHSP ופוטו-קתודה העשויה מ- K_2CsSb. חישובינו מראים כי לגלאי מסוג תהיה ירידה של 20% ביעילות הקוונטית של הפוטוקתודה הבי-אלקאלית לאחר חשיפה למטען יונים מצטבר של כ- 2 $\mu C/mm^2$. עם זאת, כמות כה גדולה של מטען תצטבר לאחר 40 שנות פעילות רצופה בהגברה של כ- 10^5 בחשיפה לשטף פוטונים של 5 kHz/mm^2 (ביעילות קוונטית של 30%). לשם השוואה, ב- GPM בעל ארבעה מכפילי אלקטרונים מסוג GEM (IBF~$3*10^{-2}$) באותם תנאי פעולה, הירידה ב- 20% תחול לאחר כ- 150 ימים.

הרחבת מושג ה- GPM הנוכחי בכוון של גלאי פוטונים בעלי שטח רב מהווה אתגר תעשייתי. לגלאי GPM בעלי שטח פעיל רחב ישנם יישומים פוטנציאליים רבים, בפרט בניסויים גדולי היקף בפיסיקה של חלקיקים ואסטרופיסיקה. לדוגמא, דימות של קרינת צ'רנקוב ואיסוף מידע מסינטילציה (scintillation). גלאי פוטונים בעלי שטח רב הינם שימושיים גם בדימות לצרכי רפואה ותחומים רבים אחרים.

Acknowledgements

I would like to express my deep gratitude to all those who advised, supported and helped me to carry out this work. In particular, I would like to extend special thanks:

to my advisor, Prof. Amos Breskin, for introducing me to the field of radiation detection physics. His vast knowledge, advise and encouragement were essential for the successful completion of this work.

to Dr. Rachel Chechik, my second advisor, for fruitful discussions and comments. Her conceptual and practical assistance contributed greatly to this work.

to Dr. Mark Prager for his priceless advises regarding fabrication technology of alkali-antimonide photocathodes.

to Marco Cortesi, my friend and lab mate, for his unique sense of humor and support over the entire duration of my PhD.

to Moshe Klin for his expert technical support throughout my PhD.

to Dr. Dirk Mörmann, Raz Alon, Chen Shalem, students, who passed through the radiation detector physics lab while I was there, for making the laboratory a pleasant environment.

to Dr. Sergei Shchemelinin, Dr. Sana Shilstein, Dr. Jun Miyamoto, my lab mates and colleagues, for their support and helpful discussions.

Last but not least I thank Dr. Vasily Kantsler, Dr. Timur Shegai, Maxim Naglis, Marija Vucelja, Liron Klipsan and Dmitry Milstein, my best friends, who made my stay in Israel unforgettable and who will always stay in my heart.

Contents

Abbreviations

- **AMPD**: Avalanche Microchannel Photo Diode
- **APD**: Avalanche Photodiode
- **EF**: Ethyl Ferrocene
- **F-R-MHSP**: Flipped Reversed-mode operating Micro-Hole and Strip Plate
- **FWHM**: Full Width Half Maximum
- **G-APD**: Geiger-mode operating Avalanche Photodiode
- **GEM**: Gas Electron Multiplier
- **GPM**: Gas Avalanche Photomultiplier
- **HPD**: Hybrid Photodiode
- **IBF**: Ion Back-flow Fraction
- **IISEE**: Ion-Induced Secondary Electron Emission
- **LAAPD**: Large Area Avalanche Photodiode
- **MCA**: Multi-Channel Analyzer
- **MCP**: Microchannel Plate
- **MHSP**: Micro-Hole and Strip Plate
- **MICORMEGAS**: Micromesh Gaseous Structure
- **MPPC**: Multi-Pixel Photon Counter
- **MRS APD**: Avalanche Photo-Diode with Metal-Resistance-Semiconductor structure

- **MSGC**: Microstrip Gas Counter
- **MWPC**: Multiwire Proportional Chamber
- **NEA**: Negative Electron Affinity
- **PC**: Photocathode
- **PET**: Positron Emission Tomography
- **PMT**: Photomultiplier Tube
- **QE**: Quantum Efficiency
- **RICH**: Ring Imaging Cherenkov
- **R-MHSP**: Reversed-mode operating Micro-Hole and Strip Plate
- **SiPMT**: Silicon Photomultiplier
- **SPECT**: Single Photon Emission Computed Tomography
- **SSPM**: Solid-State Photomultiplier
- **TEA**: Triethylamine
- **THGEM**: Thick Gaseous Electron Multiplier
- **TMAE**: Tetrakis(dimethylamine)ethylene
- **TPC**: Time Projection Chamber
- **UHV**: Ultra-High Vacuum

Abstract

The aim of the present research was the development of novel gaseous-photomultiplier (GPM) concepts for the visible spectral range. The goal was to conceive novel state-of-the-art gas-avalanche electron multipliers coupled to thin-film bi-alkali photocathodes, capable of high-gain stable long-term operation in continuous-mode. The main difficulties were blocking of avalanche-ions and the stability of the highly-sensitive UV-to-visible photocathodes under gas avalanche multiplication.
During this research, the following points were thoroughly investigated:

- R&D on novel gaseous electron multipliers
- Production and characterization of various alkali photocathodes
- Ion back-flow reduction in cascaded gaseous multipliers
- Photocathode ageing under the ion bombardment
- Ion-induced secondary electron emission from bi-alkali photocathodes
- Gaseous photon detectors assembly and operation

The most significant results obtained are:

A cascaded electron-multiplier structure with unprecedentedly reduced back-flow of avalanche ions to the photocathode permitted for the first time a stable high-gain, continuous-mode operation of a gaseous photomultiplier coupled to a visible-sensitive K_2CsSb photocathode.

Chapter 1

Introduction

Particle physics, astrophysics and medical imaging are the main branches of science in which photon imaging detectors are extensively employed. Examples in particle physics are the Ring Imaging Cherenkov (RICH) particle identification technique and photon recording from large arrays of scintillators or scintillating fibers, calorimeters or particle-tracking systems; in medical imaging are Gamma Cameras, SPECT and PET. In Astrophysics experiments, Mega-detectors often record Cherenkov and scintillation light from enormous volumes of water or noble-liquids. The operation of photon-detectors encompasses photon conversion into a photoelectron, collection or amplification of the photoelectrons, charge signals recording. The physics phenomena and concepts vary according to the detector type. The development of a new detector concept is dictated by experimental needs and requirements; these can be: detection area (could be square meters!), high detection rates (in some cases MHz/mm^2), precise localization (e.g. sub-mm scales), fast timing (sub-ns scales), sensitivity to single photons, capability of working at high magnetic fields and cost.

Most of the existing photon detectors do not fulfill all requirements. Standard and large Photomultiplier tubes (PMT) are expensive, have limited spatial resolution and cannot operate at high magnetic fields; large area PMTs are very bulky, due to mechanical constrains; Hybrid photodiodes (HPDs) [1] combining photocathodes, accelerating fields and electron sensors are limited in size, are not immune to high magnetic fields and are very costly. Solid-state based devices with charge multiplication, like avalanche photodiode

(APD) arrays [2], are still relatively small and do not have single-photon sensitivity; the more recent Geiger-mode APDs [3], often named Si-Photomultipliers with single-photon sensitivity (high gain) become very popular in many applications but have even smaller surfaces; this prevents their use over very large areas.

Gas-filled photon detectors seem to be an attractive and suitable solution in many applications. Capability of operation at atmospheric gas pressure makes possible the production of flat devices with sensitive area of several square meters. Gaseous avalanche detectors have a well known effect of impact ionization upon application of strong electric field in the medium; this provides the possibility for considerable avalanche multiplication (in some cases $>10^6$) of the initial photoelectrons and therefore sensitivity to single photons. Modern avalanche detectors, e.g. of the type developed in this work, are fast (ns range for single photons) and permit single-photon localization with resolutions in the 100 microns range.

A large variety of gaseous photomultipliers (GPM) sensitive to UV-photons combining CsI photocathodes with gaseous electron multipliers - have been developed in recent years [4]. They have been successfully employed in many modern particle physics experiments for Cherenkov Ring Imaging; examples are: in ALICE (CERN-LHC relativistic heavy ion experiments) [5], PHENIX experiment at Relativistic Heavy Ion Collider (RHIC) [6], COMPASS experiment at the Super Proton Synchrotron (SPS) at CERN [7] and others. There are dark matter experiments planning the use of UV-GPMs [8].

An extension of the sensitivity range of gaseous detectors towards visible wavelengths would be a significant step forward, extending the area of applications of GPMs. This project, under investigations at our Laboratory over the past decades, is very challenging due to the many physical processes and technological barriers involved. Our works towards the realization of visible-sensitive GPMs were devoted to the surface protection of chemically-sensitive photocathodes [9], development of gaseous electron multipliers [10, 11, 12] and, finally, the first proof-of-principle of visible-sensitive GPMs [10, 13].

Chapter 2

Objective of the research

The present challenging research was devoted to the understanding and resolution of the physical limitations of visible-sensitive GPMs that would permit conceiving efficient large-area photon detectors with single-photon sensitivity, capable of high-rate operation also in magnetic fields and with good localization and timing properties.

The main goal of this research was to combine thin-film photocathodes sensitive in visible-spectral range, with fast cascaded micro-patterned gas avalanche multipliers sensitive to single charges. This required extensive research of numerous physical processes involved, e.g. photoemission into gas, electron and ion transport in a gas media, avalanche processes in cascaded multipliers, ion-induced secondary effects on the photocathode and their reduction etc.

Chapter 3

Scientific background

3.1 Photoemission from metals and semiconductors

An incident photon interacting with the photosensitive material of the detector, results in a conversion of the photon into an electron via the *photoelectric effect*. This electron is then extracted from the photosensitive material, amplified and subsequently recorded.

The energy of the photoelectrons depends on the frequency of the incident radiation - the higher the frequency, the greater the energy of its photons. This effect was first observed in 1887 by Heinrich Hertz [14], who showed that electric sparks occur more easily when the electrodes are illuminated with ultraviolet light. At the time it was thought to be due to the ejection of electrons by light. The theory of the photoelectric effect, a quantum theory of radiation, was formulated by Albert Einstein 1905 [15]. In 1921 Einstein received the Nobel Prize for the discovery of the law of the photo-electric effect which can be formulated as follows:

$$E_k = h\nu - E_{pe}\,, \tag{3.1}$$

where E_k is the kinetic energy of the photoelectron, $h\nu$ is the energy of the incident photon and E_{pe} is the photoemission threshold or the minimal energy needed to remove an electron from a solid. The number of electrons emitted depends on the intensity of radiation. The most important characteristic of the photoemissive material is its Quantum Efficiency

(QE), defined as the average number of photoelectrons realized per incident photon. It depends on the properties of the irradiated material and on the energy of the incident photons. The variations of QE values for different materials were explained by Edward Spicer in 1958, see [16]. According to Spicer's model the photoemission process occurs in three independent steps: (1) absorption of the incident photon by a photosensitive material, followed by photoexcitation of an electron, (2) electron diffusion inside the material towards the material-vacuum interface, and (3) the escape of the electron over the surface barrier (electron affinity) into the vacuum. This model provides a quantitative description of photoemission, it relates the photoemission characteristics of a material to parameters of the emitter, such as the optical absorption coefficient, electron scattering mechanisms in the bulk and the height of the potential barrier at the surface.

Each step of the photoemission process is accompanied by energy losses. In the first step, only the absorbed portion of the incident light may excite an electron and thus losses by light transmission and reflection reduce the quantum efficiency. In the second step, the photoelectrons may lose energy by collisions with other electrons (electron scattering) or with the lattice (phonon scattering). In the third step, the surface barrier prevents the escape of some electrons. Therefore, the most effective photoemissive materials are those that provide less energy losses in each step of the photoemission process.

Metals are known to be inefficient photo-emitters due to many loss mechanisms occurring at each step of photoemission. First of all, the mechanism of electron excitation by photon is not efficient in metals because of its high optical reflectivity. Second, the excited electrons moving through a metal bulk towards the metal's surface rapidly lose their kinetic energy in electron-electron collisions. Thus only electrons exited in the vicinity of the metal surface have a chance to escape as shown in figure 3.1(a). The average escape depth for photoelectrons is about $10 \div 50$ $\mathring{A}$, while the photons of visible and near Ultra-Violet (UV) spectral range can penetrate into the metal up to a depth of 100 $\mathring{A}$. Last, the surface barrier in metals is determined by the work function (in most metals its above 2 eV). The process of photoemission in metals is schematically depicted in the energy diagram of figure

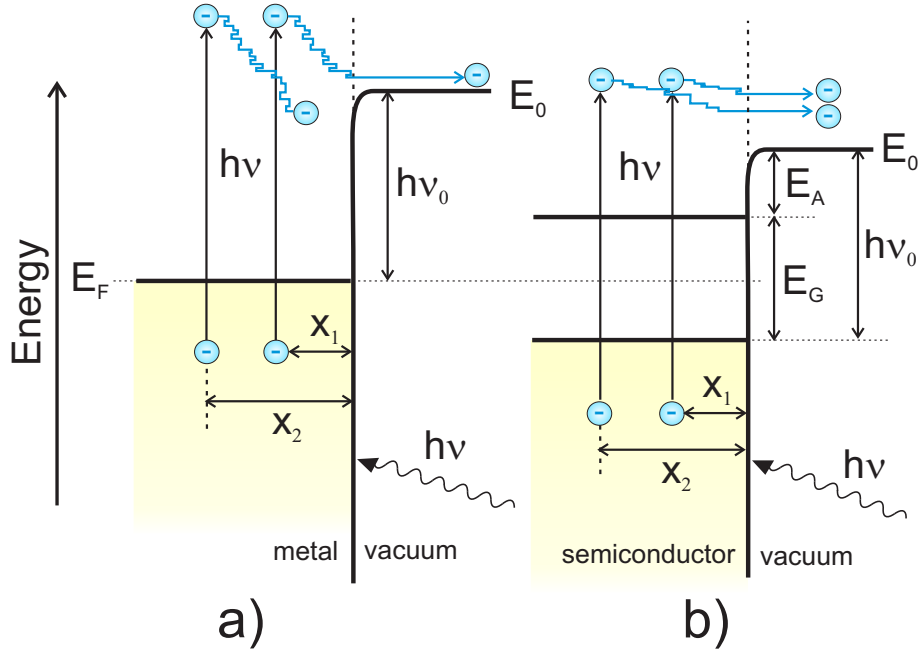

Figure 3.1: Simplified energy-bands diagram for a metal a) and a semiconductor b) both having the same photoemission threshold $h\nu_0$. An incident photon of energy $h\nu$ excites an electron at a distance x_1 or $x_2 > x_1$ from the surface. In the semiconductor, the energy losses for excited electrons as they move to the surface are rather small. The electrons excited at distances x_1 and x_2 both have sufficient energy to escape into vacuum. In the metal, the exited electrons rapidly lose their kinetic energy in electron-electron collisions. Thus only electrons excited in the vicinity of the surface could escape into vacuum. Here E_F is the Fermi level, E_0 is the energy of vacuum potential barrier, E_G is the bandgap of the semiconductor and E_A is its electron affinity.

3.1(a). The photoemission threshold in metals is given by the work function Φ defined as:

$$E_{pe} = \Phi = E_0 - E_F = h\nu_0 \,, \tag{3.2}$$

here E_F is the Fermi level which determines the thermionic work function of the metal, E_0 is the energy of vacuum potential barrier and E_k is the kinetic energy of photoelectrons.

It is easy to define the threshold wavelength for photoemission in metals:

$$h\nu_0[nm] = \frac{ch}{E_{pe}} = \frac{1236}{E_{pe}[eV]}. \tag{3.3}$$

where c is the speed of light and h is the Plank constant. The photoemission threshold for pure metals is between 2 eV and 6 eV. The boundaries of visible spectral range correspond to wavelengths between 380 nm and 780 nm, i.e. to photon energies between 1.6 - 3.25 eV. The majority of metals have the photoemission threshold $E_{pe} < 3.25$ eV [17]. The short-wavelength photoemission threshold lies beyond the visible spectra, namely in the Ultra-Violet (UV) spectral range. Such metals are not sensitive to visible-light radiation. Among the variety of metals, only alkali and some alkali-earth metals have the photoemission threshold $E_{pe} < 3.25$ eV in the middle of the visible-spectral range. Also there are no metals sensitive to radiation with a wavelength longer than 640 nm.

Unlike metals, semiconductors constitute the most efficient photo-emitters. The reflection coefficient in semiconductors is usually low, while the penetration depth for photons with energies above the bandgap energy is often high. For semiconductors, a typical penetration depth for photons of the visible spectral range is between $1000 - 10000\mathring{A}$, it is by several orders of magnitude higher than that for metals. Therefore, the conversion of photon's energy into the energy of an electron, in the optical range is more efficient for semiconductors than for metals. In semiconductors, the excited electron moving towards surface-vacuum interface, scatters preferably on phonons (lattice vibrations) and the energy losses through phonon scattering are rather small. Usually, in semiconductors the photoelectrons, which are created at a distance of few hundred angstroms from the surface, have sufficient energy to escape into vacuum. This distance is by a factor of 10 larger than the typical values for metals. The role of the surface barrier in semiconductors is best understood in terms of the band model diagram (see figure 3.1(b)). It should be emphasized that figure 3.1(b) represents bands in an idealized case. This figure ignores that the shape of the bands is determined by the density of states. Likewise it ignores the presence of defect levels in the forbidden gap and band-bending effects near the surface.

As already mentioned above, if a photon's energy exceeds E_G this photon can be absorbed and converted into a free electron, i.e. raised from the valence band into the conduction band (figure 3.1(b)). To escape into the vacuum the electron must have sufficient energy to overcome the electron affinity E_A, represented on figure 3.1(b) by the distance between conduction band bottom and vacuum level. Hence, the minimum energy required for a photon to produce photoemission (photoemission threshold E_{pe}) is

$$E_{pe} = E_G + E_A = h\nu_0. \tag{3.4}$$

For the PCs sensitive to visible light, this sum must therefore be less than 3.25 eV (less than 1.6 eV to cover the whole visible region up to 780 nm). This condition is fulfilled in some complex semiconductors has made modern PCs possible.

The Fermi level in figure 3.1(b) is drawn at halfway between valence band top and conduction band bottom assuming an intrinsic semiconductor. In a semiconductor the Fermi level determines the thermionic work function (hence the thermionic emission), which on **??** corresponds to $E_G/2 + E_A$.

Abundance of previous experimental observations from different groups have shown that high QE and long threshold wavelengths can only be achieved in semiconductors. The sensitivity of metals in the visible spectral region is limited by losses that accompany the process of absorption of the incident photon and losses due to electron-electron collisions, as well as the threshold limitation, imposed by the work function. The highest sensitivity of metals in the visible region is only of the order of 10^{-4} electrons per incident photon. Contrary to this, in semiconductors, the absorption of a photon and electron diffusion through a semiconductor lead to negligible losses. Thus the QE of some semiconductors, at photon energies that exceed the photoemission threshold $E_G + E_A$, is close to its maximum.

3.1.1 On the efficiency of semiconductor photo-emitters

N- and P-type semiconductors: Surface band-bending

In vicinity of the vacuum-semiconductor interface, the symmetry of the crystal lattice is violated, the periodic boundary conditions can not be applied anymore to the electron wave functions. This influences the distribution of forbidden and allowed electron states near the surface. It was shown in 1937 by Tamm, that the termination of a semiconductor material with a surface leads to appearance of new electronic states, so called "Tamm's levels" or surface levels [18]. His theoretical calculations showed that for intrinsic semiconductor, the highest concentration of surface levels is observed close to the middle of the band-gap and that approximately a half of these levels is filled. The Fermi level in this case is located between the topmost filled level and the lowest empty level (figure 3.2 (i)). In the case of a n-doped semiconductor, the Fermi level is shifted towards the bottom of the conduction band. The equilibrium of the system is reached as a part of the electrons leaves the bulk donor-levels to fill empty surface levels located below the Fermi level (figure 3.2 (n)). Due to the loss of electrons by the bulk, the surface charges negatively, while the bulk material near the surface charges positively forming a surface dipole. The thickness of positively charged near-surface layer depends on the dopant concentration. As a consequence of surface charging, the energy levels in the semiconductor bulk shift downwards with respect to the vacuum level. The energy diagram of such semiconductor is shown in figure 3.2 (n). In this figure the x-axis directed from the vacuum-surface interface towards the semiconductor bulk. If the photoelectron escape depth l_e is considerably larger than the width of band-bending x_0, $l_e \gg x_0$ (mainly the photoelectrons created inside the bulk participate in photoemission), then the vacuum level for such electrons appears to be higher by a value of ΔE due to presence of a decelerating electric field induced by the surface dipole. Therefore, the photoemission threshold becomes larger by a value of ΔE for photoelectrons created at distances larger than x_0 from the surface, resulting in a PC with poor QE.

The energy bands of a p-doped semiconductor are shown in figure 3.2 (p); they are bent downwards unlike in n-doped semiconductor. This results in lowering of the vacuum level

by a value of ΔE. The emission of electrons from the p-doped semiconductor goes easier due to presence of accelerating electric field at the surface; it pulls the electrons from the bulk to the surface. The evolution of the photoemission threshold value $h\nu_0$ with the type of dopant is also shown in figure 3.2. It is clear that *p-doped semiconductors* are the best photo-emitters as they are characterized by a lower photoemission threshold value.

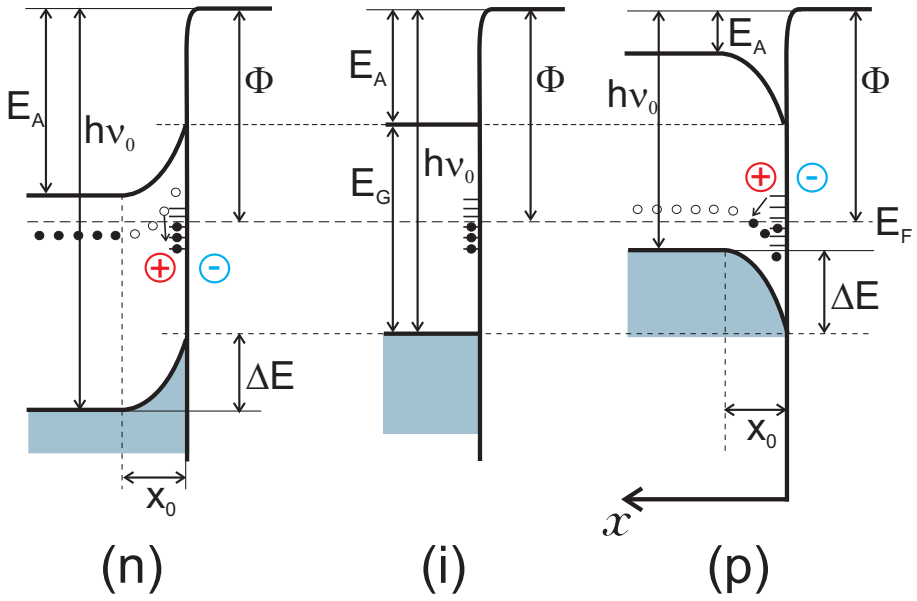

Figure 3.2: Energy band diagrams in the near surface region for n-doped (n), intrinsic (i) and p-doped (p) semiconductors

The role of the band-gap energy and the electron affinity

The efficiency of photoemission for a majority of semiconductors depends on the ratio between the energy of the band-gap E_G and the electron affinity E_A. Suppose we have an incident photon with energy slightly higher than $(E_G + E_A)$. Such a photon is able to rise an electron from the top of the valence band to the vacuum level. Upon reaching the conduction band, i.e. after spending the energy E_G, the electron is a so called *hot electron* with the excess energy E_A. Next, there are two possible scenarios. If $E_G/E_A > 1$ the electron has a high probability of escaping into vacuum, because the only other alternative

would be energy loss by phonon scattering, which is observed to be inefficient. If, on the other hand, $E_G/E_A < 1$, the electron raised to the conduction band has sufficient energy either to escape or to raise another electron from the valence band into the conduction band. In the second case neither of the two electrons has sufficient energy to escape into vacuum. Experiments have shown that the electron-hole pair production is a more probable process, than the emission into vacuum. Thus semiconductors with $E_G/E_A > 1$ tend to have higher QE, than those with $E_G/E_A < 1$. Summarizing the discussion of this section, we conclude that in order to be an effective photo-emitter the semiconductor must fulfill the following requirements:

- it has to be p-doped,
- the ratio of band-gap value E_G to electron affinity value E_A has to be greater than unity.

3.2 Photocathodes for the visible-light detection

Practical photo-emitters are usually called photocathodes (PCs). Visible sensitive PCs are photo-emissive materials exhibiting high QE ($\sim 30\%$) in the visible spectral range, typically 380 nm to 780 nm. Therefore, as noted above the photoemission threshold $E_G + E_A$ for a visible-sensitive PC should be less than 3.25 eV or less than 1.6 eV to cover the whole visible region. A comprehensive review on the PCs sensitive in near-UV to visible spectral range can be found in [17].

3.2.1 Reflective and semitransparent PCs

A PC in most of photo-sensors is usually a thin layer of semiconductor photo-sensitive material deposited either onto a transparent substrate or reflective (metal) substrate. One distinguishes reflective (or opaque) from semi-transparent (or transmissive) photocathodes according to their mode of operation. In reflective photocathodes, light is incident on a thick photoemissive film and the electrons are emitted backwards (figure 3.3(a)), while in

semitransparent photocathodes the photoemissive material deposited onto a transparent substrate is illuminated from the substrate side and the electrons are emitted forwards (figure 3.3(b)).

For semitransparent PCs the thickness of the cathode film has a critical optimum value. If the thickness exceeds the escape depth of photoelectrons, the sensitivity is unnecessarily reduced, because photoelectrons produced by light absorbed beyond the escape depth cannot be emitted into vacuum. On the other hand, if the thickness is much smaller than the escape depth the sensitivity may be reduced, since a fraction of the incident light is transmitted rather than absorbed.

For reflective PCs, the cathode thickness is less critical. If the cathode is deposited onto a reflective (usually metal) substrate, the incident light which was not absorbed in the cathode is reflected back by the substrate and could be absorbed when passes the PC for the second time (figure 3.3(b)). The reflective PCs exhibit higher QE values due to an efficient light absorption and are simpler in fabrication due to the absence of strict requirements on the thickness, the reflective PCs are simpler in fabrication. However, the coupling of reflective PCs of large area to electron multipliers is more difficult.

The optimal thickness of a semitransparent PC is not a unique number, characteristic for a particular PC material. In semiconductors the absorption constant and the photoelectron escape depth are both wavelength dependent; they increase with decreasing wavelength. That means, the light of shorter wavelength produces not only more electrons within a given distance from the surface of incidence, but also electrons which have a greater escape depth. Therefore, the optimum thickness represents the compromise between loss of light by transmission and loss of those electrons that can not escape; it is wavelength dependent. As a result, the spectral response of a semitransparent PC can be modified to a certain extent by using the optimum thickness for the spectral region in which maximum sensitivity is required. For instance, because of low light absorption near the threshold wavelength, increased PC thickness tends to enhance long wavelength response at the expense of sensitivity in shorter wavelengths.

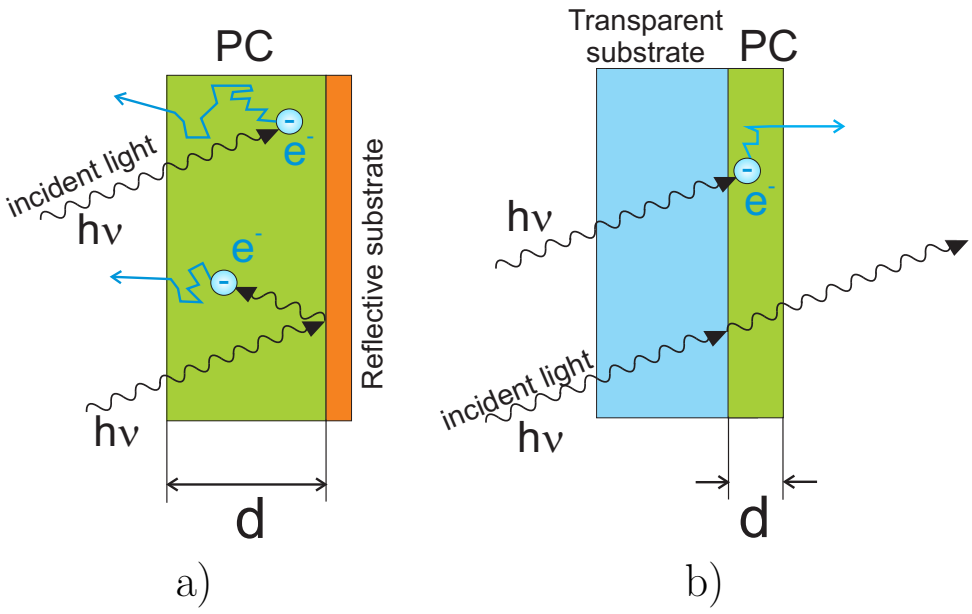

Figure 3.3: Reflective a) and semitransparent b) PCs

3.2.2 Semiconductors with Negative Electron Affinity (NEA)

The band-bending near the surface shown in section 3.1.1 (figure 3.2 (p)) for p-doped semiconductor could be further increased if one deposits onto the surface a molecular layer of, the so called *electro-positive* material. A layer of polarized or ionized atoms of such substance, with its positive pole directed towards vacuum, acts as a surface dipole, the electric field of which considerably reduces the vacuum potential barrier for photoelectrons in the bulk. Known electro-positive materials are Ba-O, Cs-F, Cs, Cs-O. The dipole moment of O-Cs chemical bond is known to be the strongest, therefore a molecular layer of Cs-O deposited onto the surface of heavily doped p-type semiconductor considerably reduces the work function of the material. For some semiconductor materials covered with such dipole layer, the vacuum level could be pulled down below the bottom of the conduction band resulting in a Negative Electron Affinity (NEA), as shown on figure 3.4. The photoemission threshold in NEA PCs is equal to the band-gap. In the PCs without NEA, a photoelectron excited to conduction band travels in the bulk loosing its energy in

phonon-scattering, once its energy is reduced below the vacuum level it cannot escape the PC anymore; therefore it travels rather short distance (typically about $100 - 200\,\text{Å}$) until it recombines with a hole. In NEA PCs, once the photoelectron energy approached the conduction band minimum, the photoelectron can not longer lose small amounts of energy in electron-phonon interactions, due to a lack of energy states in the band gap. It continues to stay in the conduction band minimum for a long time, it typically travels 10^5 Å before it recombines with a hole. The photoelectron escape depth is greatly increased in NEA PCs resulting in an increase of the PC's QE to more than 50%. NEA has been reported for many semiconductor materials like silicon [19], diamond [20] and III-V semiconductors (GaAs, GaP, InSb, InP, InAs etc.) [21]. Photo-sensors equipped with NEA PC are widely used and commercially available [22, 23, 24]. However, NEA PCs are generally fairly small due to complex fabrication process involving the epitaxial deposition of several layers of single crystal semiconductors. Moreover these PCs should be kept in an extremely clean vacuum environment to retain their properties; fabrication of large $> 10cm^2$ area NEA PCs seems unrealistic.

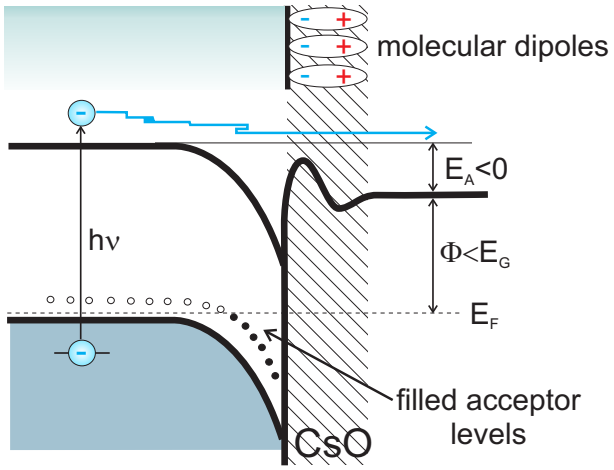

Figure 3.4: Semiconductor energy-band model showing negative electron affinity

3.2.3 Alkali-antimonides

PCs based on alkali-antimonide compounds are widely employed in many commercially-available photo-detection devices like Vacuum Photo Multipliers, Hybrid Photo-Detectors, Night-vision Devices etc., because of their good photoemission characteristics in the UV-to-visible-spectral range and relatively simple fabrication technology. Good photoemission properties of alkali-antimonides are consequence of the low work function of alkali metals and the related antimonide compounds. The alkali-antimonide PCs are usually fabricated by vacuum evaporation of a thin ($\sim 100\mathring{A}$) Sb layer and its successive treatment in alkali metal vapors. A detailed description of procedures used in our laboratory for fabrication of various alkali-antimonide PCs can be found in section 4.3 of this thesis work. The methods for production of alkali-antimonide PCs were well established [9, 10, 17, 25] in the past, though, there is still a room for optimization of technological processes in order to improve the PC's emission properties, e.g. Hamamatsu Photonics [26] advertises the vacuum PMTs equipped with "ultra bi-alkali" PCs which have a peak QE of 43%.

One distinguishes three main types of alkali-antimonide PCs depending on their spectral characteristics: blue-sensitive (Cs_3Sb, K_2CsSb, Na_2KSb), green-enhanced (Rb_2CsSb) and red-enhanced ($(Cs)Na_2KSb$). The spectral characteristics of these PCs are presented in figure 3.5 of ref. [27]. They exhibit typical QE values of 20-30% at maximum, located in the blue or green spectral regions.

3.2.4 PCs for large-area visible-sensitive Gaseous Detectors

Photocathodes employed in a large-area visible-sensitive gaseous detectors should have a large active area (up to 1 m^2). This implies production by chemical evaporation and activation techniques. Alkali-antimonide PCs described in the previous section would be the right choice.

There are few important remarks one should take into account when dealing with alkali-antimonide PCs. First, they are chemically reactive with limited (few minutes) lifetime even at 10^{-5} Torr of oxygen and moisture [28]. Therefore, detectors comprising alkali-

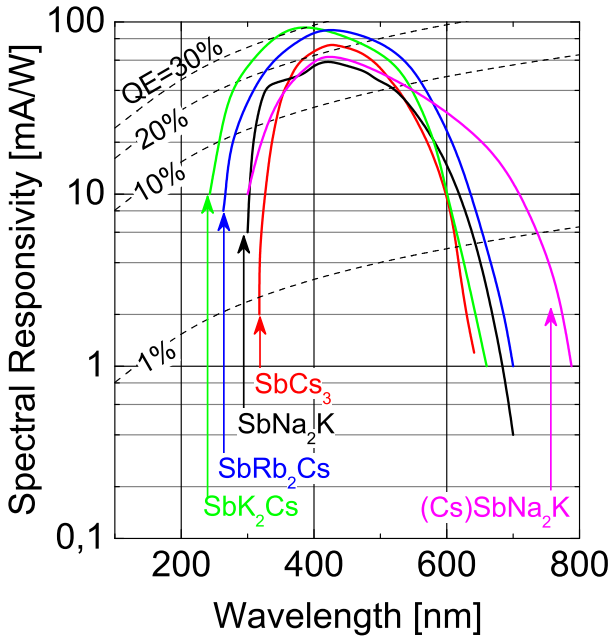

Figure 3.5: Typical spectral characteristics of the most common alkali-antimonide PCs

antimonide photocathodes must operate in a sealed-mode with multipliers made of pure (ultra-high vacuum compatible) materials and preferably with a getter installed inside the detector housing. Second, the PC has to retain its high photoemission properties in gas environment over a long period of time. The stability of alkali-antimonide PCs in gas environment was studied in the past [10, 11, 25, 29]. A K_2CsSb PC sealed in a Kovar envelop showed stable behavior at 680 Torr of pure argon during half year period [11]; both Cs_3Sb and K_2CsSb PCs showed no deterioration during two-days storage in a vacuum chamber filled with pure methane at 760 Torr [25]. A stable operation of a Cs_3Sb PC in pure Xe during 45 days was reported in [29]. Additional studies of the PC stability in Ar/CH_4 (95/5) mixture and in pure CH_4 were performed within this work (see section 5.1.2 for details).

3.3 Photon detectors, other than Gaseous Photomultipliers

One distinguishes two types of photodetectors: devices utilizing *internal* and *external* photoelectric effects. The first are solid-state devices where the photons are absorbed and detected within the same solid medium. The second are vacuum and gaseous devices where the photoelectrons from the PC are emitted into vacuum or gas media and subsequently recorded. A photodetector could operate either in *pulsed mode* if it is illuminated with bunches of photons (or single photons) or in *continuous mode* under constant illumination at a given photon flux. The electron signal is recorded with a proper electronic circuit. Single- or even few-electrons do not constitute a sufficient charge for detection at room temperature, due to thermal noise of the electronics. **Typically, a minimal light signal that can be detected by readout electronics is equivalent to a charge of about 10^3 electrons.** In order to extend sensitivity of a photon detector to single photons or to very low photon fluxes primary photoelectrons must be multiplied before being recorded in the readout circuit. Photodetectors without photoelectron multiplication are not sensitive to low light levels. The detection of the latter can thus be subdivided in three steps:

- photon absorption followed by an electron excitation in the PC or in another solid medium,
- photoelectron multiplication,
- recording and processing of the multiplied charge.

In this work, we focused at the fast detection of low light levels in the visible spectral range with gaseous photomultipliers. The following sections provide an overview of alternative detection methods of light with very low intensity as well of the current status of gas avalanche photon detectors.

3.3.1 Solid-state devices

Solid-state photodetectors [30] utilize internal photoelectric effect; a single crystal semiconductor bulk acts as an active detection medium. Solid-state photon-detectors are sensitive devices due to a very low photoemission threshold equal to the band-gap of the semiconductor material, high photon absorption and QE values approaching 100% over the entire visible spectral range. The solid-state detectors are immune to magnetic fields, though suffer from substantial temperature dependent dark currents, temperature dependance of some output characteristics and small active area.

Avalanche Photodiode (APD)

Unlike PIN diodes, APD's have internal multiplication [30]. An avalanche photodiode is a silicon-based semiconductor containing a thin p-n junction, consisting of a positively doped p layer and a negatively doped n layer followed by a thick intrinsic layer. Photons entering the diode are absorbed in the intrinsic layer, where they excite free electrons and holes, which then migrate towards the p-n junction. Upon application of a reversed bias across the diode, a strong electric field is established in the p-n junction. The electrons reaching the p layer continue to gain energy as they undergo multiple collisions with the crystalline silicon lattice causing further impact ionization liberating other electrons and subsequently resulting in an electron avalanche. The multiplication factor (gain) of the APD can be tuned by changing the reverse-bias voltage. A larger reverse-bias voltage results in a larger gain. However, a larger reverse-bias voltage also results in increased noise levels. Excess noise resulting from fluctuations in the avalanche multiplication process places a limit on the useful gain of the APD. In operation, very high reverse-bias voltages (up to 2500 volts) are applied across the device.

Avalanche photodiodes are capable of a modest gain (500-1000), but exhibit substantial dark current, which increases markedly as the bias voltage is increased. They are compact and immune to magnetic fields, require low currents, are difficult to overload, and have a high QE, that can reach up to 90 percent in the visible spectral range. Avalanche

photodiodes are now being used in place of photomultiplier tubes for many low-light-level applications like scintillating fibre [31, 32] and scintillator [33] readout and detection of scintillation light of liquid xenon [34]. However, APDs are not capable of detection of single photons because of insufficient internal gain. Typically, APDs have rather small sensitive area of 25-100 mm^2 and, therefore, they should be used in arrays of many elements [32].

In Large-Area Avalanche Photo-Diodes (LAAPDs) the sensitive area of the device reaches about 5 cm^2, though at the expense of higher noise levels. LAAPDs can be used both for visible-light and X-ray detection; they can operate in strong magnetic fields up to 5 T with negligible performance degradation [35].

Geiger-mode Avalanche Photodiode (G-APD)

In Geiger-mode operating APD (G-APDs) [3, 36] also known as SiPMs, SSPMs, MRS APDs, AMPDs, MPPCs, the modest gain of an APD is increased to a level sufficient for single-photon detection. In G-APDs, the electric field, as described above, increases with increasing the applied voltage, thereby increasing the APD gain. At some operating voltage, either photo- or thermal-electron entering the avalanche region in the semiconductor junction could initiate a breakdown and the APD will become a conductor - this is known as a Geiger discharge. In fact, the APD is stable above this breakdown voltage until an electron enters the avalanche region. The number of electrons in an avalanche initiated by a single photon in the breakdown regime typically reach values of 10^5 - 10^7. This breakdown could be controlled by placing a resistor in series with the detector. When the junction breaks down, large current flows through the resistor, resulting in a voltage drop across the resistor and in the APD. If the voltage drop is sufficient, the APD voltage will drop below the breakdown voltage and the current flow through the device will be terminated. The APDs utilizing discharge-and-reset cycle are known as the Geiger mode APD (G-APD). Nowadays G-APD is called a multi-pixel device in which every pixel acts as an independent Geiger mode APD; the pixels are connected in parallel via individual limiting resistors.

Due to their high gain, G-APD have a very good signal-to-noise ratio and perform

best for photon counting. G-APDs exhibit high photon detection efficiency: 30-40% for blue/green light and not less than 15% over the whole visible spectral range. They are low power consumers (typically less than 50 μV/W). G-APDs are intrinsically very fast due to the small depletion region and the extremely short Geiger-type discharge. Time resolutions of $\sim$120 ps FWHM were obtained with single photoelectrons. Also they are insensitive to magnetic fields up to 15 T and have very small sensitivity to charged particles traversing the device.

Despite the fact that some characteristics of G-APDs are superior to those of many conventional photo-sensors (such as vacuum Photo-multipliers, that are described in next section), they have few considerable drawbacks. The sensitive area of G-APDs does not exceed 25 mm^2. G-APD are characterized by high dark count rates at room temperature due to thermally- or field-assisted generation of the free carriers which can trigger a breakdown in the range of several hundred kHz to several MHz per square millimeter sensor area and that is by several orders of magnitude higher than that of vacuum devices.

In each Geiger avalanche occurring in a single pixel of a G-APD, few photons can be emitted. Those photons could trigger a breakdown in a neighboring pixel of a G-APD resulting in a after-pulse. This process of involuntary triggering of neighboring pixels is called *optical cross-talk*. In commercially-available G-APDs, the probability for a neighbor pixel to be triggered is about 10%.

Some time is needed to fully recharge the pixel after the breakdown. During this time the signal amplitude is reduced and might be below the threshold of the readout electronic. In addition, the breakdown probability, which depends on the over-voltage, is reduced and the detection efficiency is diminished even more. Typical recovery time for a single G-APD's pixel could reach 100 μS. A long recovery time drastically reduces rate capability of G-APDs; they, simply, can not be used in high rate applications.

G-APDs will be employed in Super BELLE experiment for readout of scintillator strip detectors [37], CMS electromagnetic calorimeter [38], MAGIC telescope for detection of Cherenkov light from cosmic gamma-rays [39] etc. They have many other potential applications.

3.3.2 Vacuum Photodetectors

Vacuum photodetectors utilize the external photo-effect; the incident photon is converted to a photoelectron in a thin-film photocathode and subsequently released into the vacuum inside the device's case. As mentioned above, the QE of common PCs is limited to $\sim$ 30-45% at maximum, usually located in the blue spectral range. The PCs in photo-detectors are usually less sensitive in green and red spectral ranges. The amplification is achieved by accelerating the photoelectrons released from the PC to high kinetic energies in a strong electric field, resulting in the generation of secondary electrons on series of dynodes or within semiconductors.

Photo Multiplier Tube (PMT)

Vacuum Photo-Multipliers (PMTs) are still the most popular and versatile photo-detectors. They exhibit high sensitivity to single photo-electrons at gains exceeding 10^7, are capable of high counting rate operation and have good time resolutions. There is an enormous experience in PMT applications in various fields. However, PMTs have some drawbacks like sensitivity to magnetic field, bulky shape and low granularity, high operation voltage. They are also quite expensive. These drawbacks can be partially cured. Multi-anode PMTs (MAPMTs) offer higher granularity and position sensitivity with a smallest available pixel size of 2x2 mm^2 [23], but they suffer from limited sensitive area and high cost. Costly, Micro-channel plate PMTs (MCP-PMTs) utilizing Micro-Channel Plates as electron multipliers can work to some extent in magnetic fields. In MCP-PMTs the PC is placed in proximity to the MCP dynodes resulting in very good timing properties and largely decreased sensitivity to magnetic fields. It was shown in [40] that these devices can operate in magnetic fields up to 2 T with an appropriate orientation. A cutting-edge approach has been proposed by the Belle Collaboration through the development a GaAsP photo-cathode MCP-PMT characterized by a QE of about 40% at 500 nm, and sensitivity extended to the longer wavelength (up to 700 nm) [41]. However, the cost-per-piece of this new MCP-PMTs is expected to rather high due to a very complicated production process

of GaAsP PC. Also the lifetime of a PMT equipped with such PC could be rather short due to very strict vacuum requirements.

Recently PMTs with high QE have been developed. The high QE PMTs by Hamamatsu Photonics Inc. equipped with "ultra bi-alkali" PCs which have a peak quantum efficiency (QE) of 43% are available on the market [26]; however, the cost of these PMTs is rather high. It was reported [30] that, Photonis Inc. is expected to announce PMTs with the regular bi-alkali photocathode, but with drastically improved quantum efficiency (QE) of about 55% at 380 nm, which is almost twice higher than that of a standard device.

Hybrid Photo Detector (HPD)

A hybrid Photo Detector (HPM) has a semitransparent photocathode; the photoelectrons induced by the incident photons are accelerated in a high electric field $\sim$ 20 kV towards a silicon diode, producing electron-hole pairs due to multiple ionization collisions with bulk. The number of secondary electrons liberated within the silicon diode is determined by the energy the primary electron gained in the electric field divided by 3.6 eV, the energy needed in average to create an electronhole pair (amplification). The amplification gain is typically $\sim$5000 [30].

HPDs have a quantum efficiency comparable to photomultipliers. The proximity-focused type HPDs can operate in axial magnetic fields up to 1.5 T [42]. The energy resolution is suitable for single-photon counting [43] since the statistical fluctuations in the "amplification" are small compared to the signal.

The anode made of a silicon diode can be segmented into many elements providing position sensitivity to the device. A prototype with 208 anode pixels designed for an axial PET is currently under construction at CERN [44]. HPDs will be soon employed for the ring imaging Cherenkov (RICH) detector for particle identification in the CERN-LHCb experiment. These HPDs have 80 mm photocathode diameter. The electrons are focused onto a pixellized silicon diode with 1024 pixels of $0.5 \times 0.5\,\mu\mathrm{m}^2$ size each. A large area spherical shape HPD 43 cm in diameter is currently under development for deep-sea

neutrino experiments [45].

3.4 Gas-avalanche Photo-Multipliers (GPMs)

In GPMs (figure 3.6) a solid-state photocathode serves as photon-to-electron converter. It is coupled within a gas medium to an avalanche electron multiplier and a readout electrode. An electric field is applied between the PC and the multiplier; it has as a role of the extraction of photoelectrons from the PC and their transport into the multiplier. In the multiplier, the photoelectron gets accelerated by a strong electric field and looses energy in collisions with the gas molecules. If the energy acquired by field acceleration is larger than the ionization threshold of the gas molecules, ionizing collisions will occur, resulting in more electrons and ions created in the gas. This is the avalanche multiplication process. In the simplest GPM (see figure 3.6) a strong electric field is applied in the gap separating the PC and the anode; the electrons are accelerated within this gap creating an avalanche, so that the gas medium with the electric field acts as an electron multiplier.

The multiplication process in GPMs could be quantitatively described as follows. We consider an electron liberated in an ionization collision in a region between the PC and the anode, under high electric field (see figure 3.6). After mean free path α^{-1} one electron pair will be produced and two electrons will be accelerated by the electric field to generate, again after the mean free path, two other ion-electron pairs and so on. Here the mean free path, α^{-1}, otherwise known as the *first Townsend coefficient*, represents the number of ion-electron pairs produced per unit length. The number of electrons n at a given position x, after a path dx increases as $dn = n\alpha dx$. Thus by integration we get

$$G \equiv \frac{n}{n_0} = e^{\alpha x}\,, \tag{3.5}$$

where G represents the multiplication factor, the *gain*. It was shown in [46], that the gain depends on the voltage V_0 applied between the PC and the anode (see figure 3.6) as follows

$$G = Ke^{CV_0}\,, \tag{3.6}$$

here K and C are some constants, that depend on the multiplier geometry and the gas properties. The requested gain is dictated by light level and by the sensitivity of the readout electronics; for most applications, such as single-photon detection, it has to be higher than 10^4, as was already mentioned above.

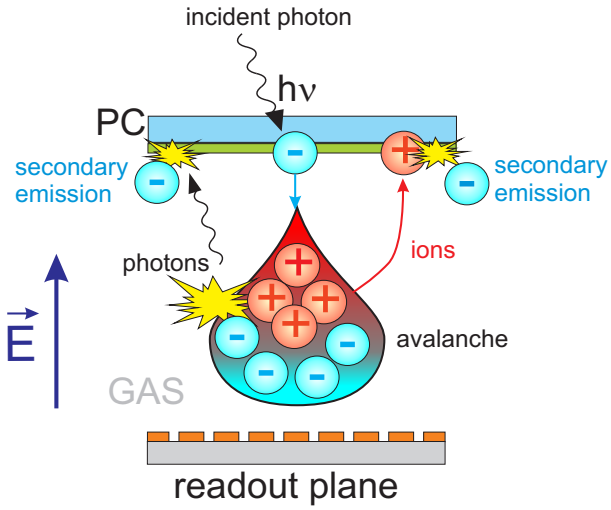

Figure 3.6: The concept of gaseous photon detectors comprising an avalanche multiplier coupled to a solid photocathode

Among the other useful properties, the gas avalanche detectors photon detectors exhibit advantageous features that are not reached by any other photo-detector. High gains guarantee sensitivity to single photoelectrons, which makes GPMs suitable for photon counting. Due to the fast pulse generation times of the order of ns in modern micro-pattern gaseous detectors, excellent time resolution in sub-ns scale and high rate capability exceeding 1 MHz/mm^2 can be achieved. An excellent spatial resolution of about 100 μm for single photoelectrons were recorded for some GPMs [47]. The GPM are immune to magnetic fields up to 5 T [48]. Furthermore, the presence of magnetic field could improve some device's characteristics [49]. The main advantage of GPMs is that they are capable of operation at atmospheric pressure; they can be constructed very large with an active area exceeding a m^2 in flat geometry, limited only by the photocathode manufacturing process. This gives them a distinct advantage over semiconductor and vacuum devices.

A main drawback of GPMs the considerable avalanche fluctuations. In particular, for the case of a single initial charge, the avalanche size is distributed according to Furry probability [50]:

$$P_{Furry}(n,x) = \frac{1}{\overline{n}}\left(1-\frac{1}{\overline{n}}\right)^{n-1}, \tag{3.7}$$

here P_{Furry} is the probability to have a certain number of electrons in an avalanche, $\overline{n}$ is the mean avalanche size or multiplier gain. In the case of a uniform electric field the multiplier gain is $\overline{n} = \exp(\alpha x)$, where α is the first Townsend coefficient and x is the distance from the cathode. In the limit of high gain or $\overline{n} \gg 1$, which is usually the case in gaseous detectors, the equation (3.7) transforms into a simple exponential distribution:

$$P_{Furry}(n,x) \cong \frac{1}{\overline{n}}\exp\left(-\frac{n}{\overline{n}}\right), \tag{3.8}$$

which shows that the $P_{Furry}(n,x)$ exponentially decreasing with n and the avalanche size fluctuations of n from the average value $\overline{n}$ are large.

In case of very high fields, liberation of two or more electrons in one ionization collision is possible, there the avalanche size is distributed according to a Polya distribution [51]. An asymptotic form of Polya distribution for a large avalanche size n (large is already $n > 100$) is given by:

$$P_{Polya}(n,x) \cong \frac{1}{(b-1)!}\frac{b}{\overline{n}}\left(\frac{bn}{\overline{n}}\right)^{b-1}\exp\left(-\frac{n}{\overline{n}}\right), \tag{3.9}$$

here the b is an empirical constant. This empirical constant is related to the first Townsend coefficient α, as follows $\alpha' = \alpha[1 + (b-1)/n]$. Equation (3.8) can be obtained from the Polya distribution, equation (3.9) by choosing $b = 1$.

In GPMs a vast majority of avalanches will contain a small number of electrons. However, in most of GPMs, it is possible to find operation conditions at which most of the avalanches (>95%) will contain more electrons than the threshold value for the readout electronics (10^4) and thus are detectable. Large avalanche fluctuations will also affect signal monitoring, as the signal amplitudes will vary for different single photoelectron events.

The photon detection efficiency depends on three factors: the PC's QE, the loss of photoelectrons by their scattering on gas molecules and the electron detection efficiency

ε_{det} of the gas avalanche electron multiplier (geometry and gain dependent). The single-photon detection efficiency ε_{photon} of GPMs can thus be described as:

$$\varepsilon_{photon} = QE \cdot \varepsilon_{det}. \tag{3.10}$$

Besides efficiency, another important parameter is the long-term stability. Ageing of the multiplier elements and of the PC are the key factors affecting the stability. While the detector components can be made of stable materials and the choice of appropriate non-aging gases are known in the literature, the most sensitive element is the photocathode. Its ageing depends on both: chemical surface degradation by gas impurities and physical degradation by avalanche-induced ions [52]. The latter cause also the emission of unwanted secondary electrons, causing severe gain limitations (see discussion below).

3.4.1 GPM types

GPMs with Multi-Wire Proportional Chamber (MWPC)

Multiwire Proportional Chambers (MWPCs) [53] (e.g. ALICE RICH [5]) have been the most extensively employed large area photo-detectors in particle physics for Cherenkov light detection [54, 55]. A MWPC consists of a set of thin, parallel and equally spaced anode wires, symmetrically sandwiched between two cathode planes; figure 3.7(a) depicts a schematic cross-section of the GPM with MWPC. For proper operation, the gap d is normally 3-4 times larger than the wire spacing s. When a negative potential is applied to the cathodes, the anodes being grounded, an electric field develops as indicated in figure 3.7(b). Suppose now that a photoelectron is emitted from the PC; conditions are set such that photoelectrons will drift along field lines until they approach the high-field region, very close to anode wires, where avalanche multiplication occurs.

While first large area UV detectors employed photosensitive gases [56], more modern wire chambers employed CsI photocathodes figure 3.7(a), e.g. the proximity focusing CsI-RICH detector of ALICE [5]. These GPMs can be made very large ($\sim$m^2) in flat geometry and are envisaged or successfully employed in many particle physics experiments [55, 57].

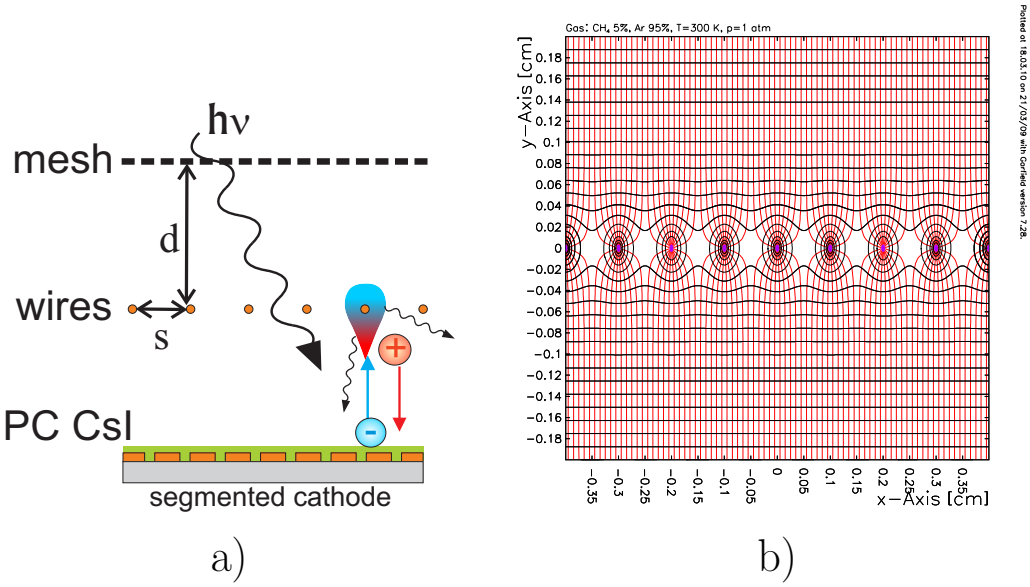

Figure 3.7: a) A scheme of MWPC GPM with a CsI PC deposited onto the bottom cathode. The electron avalanche around a wire, paths of avalanche ions and secondary photons are also shown. b) Electric field configuration (red lines) and equipotential lines (black) inside the MWPC.

Due to their open geometry, namely the photocathode is fully exposed to the avalanche photons and ions figure 3.7(a), MWPC-based GPMs suffer from severe photon- and ion-feedback and their gain is limited to well below 10^5 [57]. Half of the avalanche-generated ions are collected at the photocathode, inducing ion feedback effects and photocathode aging; this limits the choice of the photocathode to UV-sensitive ones (generally CsI) and the gas mixtures to that with low photon emission. Therefore, new gaseous multiplier types have been developed by us and by other teams for visible-sensitive GPMs.

GPMs with MIcro MEsh GAseous Structure (MICROMEGAS)

The MICROMEGAS (MICRO-MEsh GAseous Structure) [58] detector was proposed just about 10 years ago by Charpak an Giomataris [58]; it is a very asymmetric parallel-plate chamber separated into two regions called drift and amplification. A concept of MICROMEGAS GPM with a semitransparent PC is presented in figure 3.8(a). The two

regions are separated by a very thin (4-5 μm) metal micromesh, with square 20-40 μm side holes with 50 μm pitch. Photoelectrons from the PC drift through a few mm wide drift gap in an electric field of about 0.4 - 1 kV/cm towards the micromesh. The avalanche process takes place in a very narrow amplification gap of about 100 μm, where the electric field is much higher, reaching over 50 kV/cm in some gases [59].

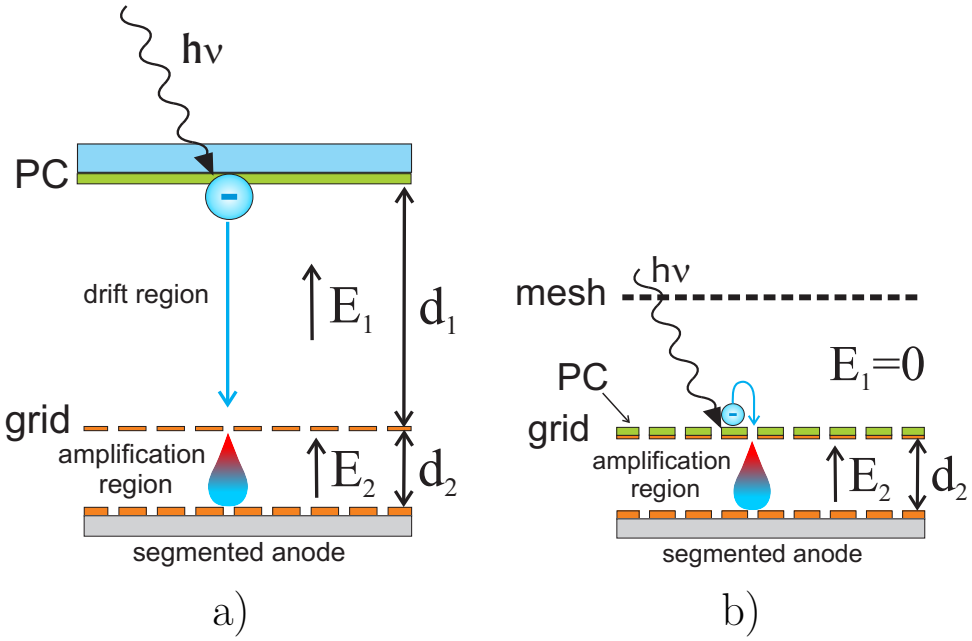

Figure 3.8: A concept of MICROMEGAS GPM with a semitransparent PC a) and with a reflective PC b).

In MICROMEGAS GPM with a reflective CsI figure 3.8(b) PC evaporated onto the top face of the micromesh, high multiplication factors of about 10^6 were reached in He/Isobutane gas-mixtures [59, 60]. Providing sensitivity to single photons [59]; some evidences of efficient photoelectron extraction from the PC were also demonstrated [59]. The MICROMEGAS with reflective photocathodes are immune to photon feedback, could have low 36% optical transparency leaving relatively large 64% fraction of the surface for the PC. The narrow amplification gap, assures very fast collection of the ions. Due to the small ion drift distance, the width of the induced signal is greatly reduced, thus high rates could

be sustained. Large active surfaces are easily reachable with MICROMEGAS: 36 x 34 cm^2 MICROMEGAS are going to be used in T2K experiment [61], 40 x 40 cm^2 MICROMEGAS detectors are being made and tested [62] for the COMPASS experiment at CERN.

Currently, the use of MICROMEGAS for visible-light-sensitive GPMs is prohibited due to relatively large flux of ions back-flowing to the PC. The studies of ion back-flow in MICROMEGAS showed that it is proportional to the inverse of the electric field ratio between the amplification and the drift gaps [63]. It was also found that the ion back-flow suppression in MICROMEGAS depends on the pitch distance between the holes in the micromesh; the MICROMEGAS with smaller pitch showed better ion back-flow suppression. Using results of [63], the average fraction of ions of the total avalanche charge flowing back to the PC in a configuration with a semitransparent PC shown in figure 3.8(a) is estimated to be about 1% at a drift field E_1=0.5 kV/cm and amplification field E_1=50 kV/cm for MICROMEGAS with 17 μm pitch. Applying these conditions in He/Isobutane (94/6) gas-mixture will result in 4000 ions per average avalanche of $4 \cdot 10^5$ electrons [59] flowing back to the PC. In MICROMEGAS with reflective PC the ion back-flow is expected to be even higher. Therefore, as discussed below (see section 3.6), the MICROMEGAS GPM can not be used with visible-sensitive PCs. While the effective QE of this detector with semitransparent PC's should depend only on effective QE, that of detectors with reflective PC's deposited on the mesh would be low due to the mesh geometry in present devices. The MICROMEGAS could be employed as a last element in cascaded micro-patterned detectors to improve their performance in terms of ion blocking.

GPMs with Gaseous Electron Multipliers (GEMs)

The GEM [64] is one of the most versatile hole-multipliers, belonging to the family of "Micro-Pattern Gaseous Detectors" (MPGD) [65]. It is made of $50\mu m$ thick Kapton (polyamide) foil with $5\mu m$ copper cladding on both sides. A dense array of single- or double-conical holes is etched in the foil. The holes, with diameters in the range between 40 and $140\mu m$ are arranged in hexagonal pattern with a pitch ranging between 90 and

$200\mu m$ (figure 3.9).

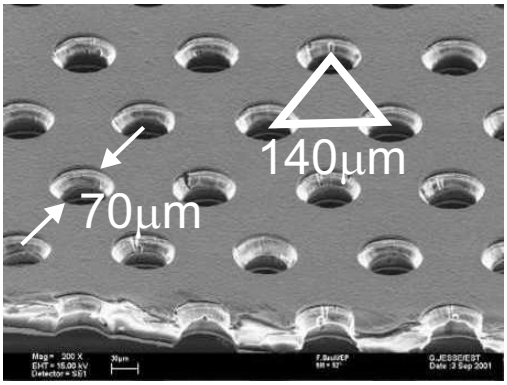

Figure 3.9: A microphotograph of a GEM.

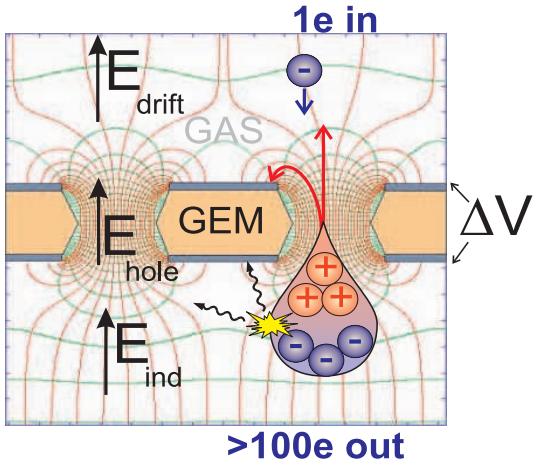

Figure 3.10: Typical equipotential and electric field line configuration in the GEM holes for optimal operation conditions. The electrons are focused into the apertures where they undergo amplification under the high local field.

A voltage difference applied between the top and bottom electrodes of the GEM creates a dipole field, resulting in very high field-values (typically 30-100kV/cm) within the holes (figure 3.10),leading to avalanche multiplication of electrons.

The gain is about few 1000 for a single GEM, insufficient for single-photoelectron detection. Therefore cascaded-GEM structures were proposed [11]. In figure 3.11 a schematic view of a triple-GEM detector with semitransparent (figure 3.11(a)) and reflective (figure 3.11(b)) PCs is depicted. Photoelectrons emitted from the photocathode are focused into the GEM apertures. Photoelectrons experience avalanche multiplication In the successive GEM holes (figure 3.11). The multiplier gain depends on the voltage applied across the holes. The gaps between two successive multipliers are the transfer regions where the electrons are extracted from one element and are guided into the next amplifier stage. The last gap, between the last multiplier and readout anode is the induction gap, where the avalanche electrons are extracted and collected by the readout anode. The cascaded-GEM structures provide rather high gas gains, exceeding 10^6 [11, 66] for single electron without

applying excessive voltage across each single element, which significantly increases the stability of the detector. The photoelectron collection efficiency into the holes was studied in detail and was shown to be close to unity [67, 68, 69]. The photoelectron detection efficiency in cascaded multipliers is fully dependant on the collection and multiplication at the first element of the cascade and the good transfer to the second one. It will be discussed in details in section 3.6.

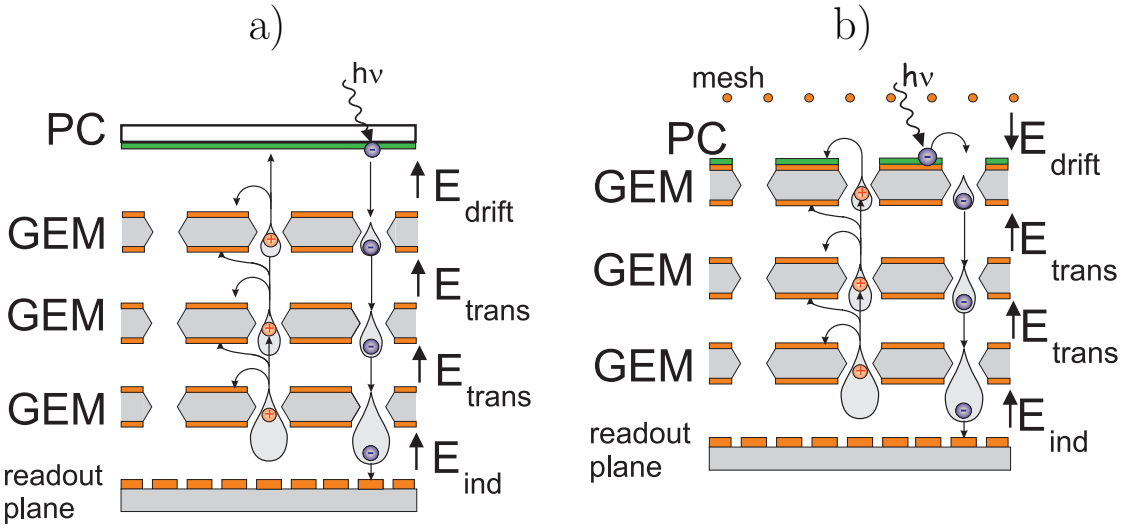

Figure 3.11: Schematic view of cascaded 3-GEM detector coupled with a) semitransparent PC, b) reflective PC. Multiplication mechanism of electrons and possible paths of back flowing ions are shown.

The high gain and the effective transfer between successive GEMs ensure high detection efficiency of single photons. Moreover, the photon feedback in cascaded GEM structures is significantly suppressed due to the avalanche confinement within the holes and to the low optical transparency of each GEM-electrode in the cascade. These multipliers can operate in a large variety of gases, including noble-gas mixtures [66]. GEMs are very fast; they provide ns time resolutions for single photons [11] and have high-rate detection capability, MHz/mm^2 [70]. Multi-GEM photomultipliers with reflective photocathodes, due to the field configurations, figure 3.11(b) have low sensitivity to background of charged particles.

Multi-GEM photomultipliers with UV-CsI photocathodes are a mature technique, already employed in Cherenkov detectors designed for relativistic heavy-ion physics experiments (PHENIX-RHIC/BNL) [71].

Due to insufficient ion-blocking capabilities (IBF values of 10% at best [10]), cascaded-GEM GPMs with bi-alkali PCs could be operated so-far only in a pulse-gated ion-blocking mode [11].

GPMs with Micro-Hole and Strip Plates (MHSPs)

A new recently introduced multiplier is the Micro Hole & Strip Plate (MHSP) [72]; it has a hole-structure, like the GEM, with additional thin strip-electrodes (anode and cathodes) etched on one face. The microphotograph of the top a) and bottom b) MHSP electrodes with their dimensions is shown in figure 3.12. The same technology and materials as for GEM are used for the manufacture of the MHSP. It is made of 50μm Kapton foil with 5μm copper coating from both sides. The 50-70 micron diameter holes are arranged in hexagonal pattern. While the perforated metalized insulator foil (figure 3.12(a)) has a continuous surface, narrow anode strips, surrounded by broader perforated cathode strips are etched on the other side (figure 3.12(b)). The structure of a MHSP gaseous photomultiplier and its mechanism of operation are shown in figure 3.12(c). Photoelectrons from a photocathode are preamplified in the holes; the resulting avalanche electrons are multiplied on the thin anode strips. The strip-gain depends upon the potential difference between anode and cathode strips. The electric field established between the cathode and anode strips at the MHSP bottom side, and the reversed field to the bottom cathode mesh diverts a large fraction of the final-avalanche ions, reducing ∼5-fold their probability to drift back through the holes to the photocathode - compared to GEM [12]. In cascaded multipliers, the MHSP can only be employed as a final amplification stage. The MHSP element can be operated in other modes with strip electrodes polarized to repel ions, as described below.

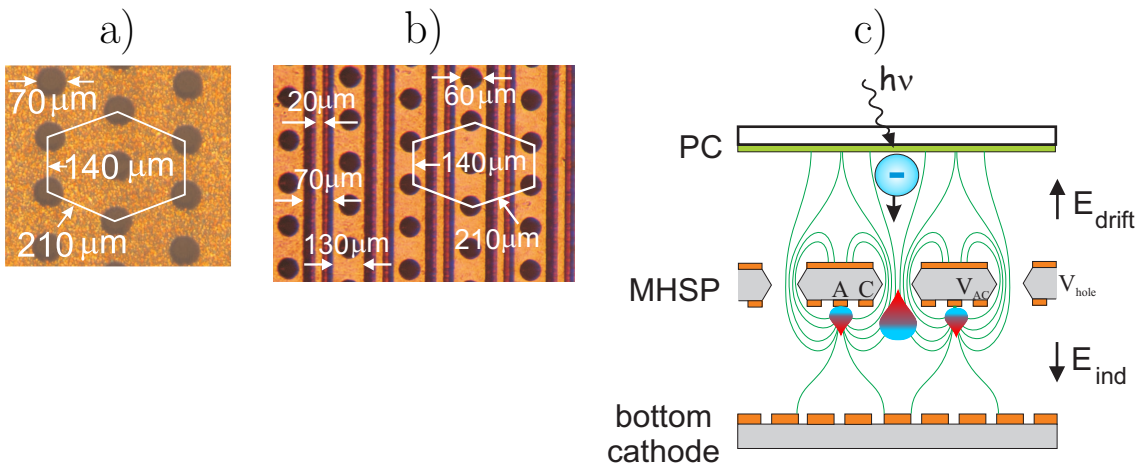

Figure 3.12: A microscope photograph of an MHSP electrode with 30μm anode strips and 100μm cathode strips. a) top view, b) bottom view. Schematics of the single MHSP detector coupled to a semi-transparent photocathode c); the electric field configuration in the MHSP and the mechanism of two-stage multiplication are also shown.

3.5 Limiting processes in GPMs

3.5.1 Photoelectron backscattering

The photoelectron emission into gas media differs from that into vacuum as a photoelectron extracted from the PC with the electric field is subject to backscattering from gas molecules. The scattering could be either inelastic or elastic. In the latter case, a chance that the photoelectron retaining its initial kinetic energy in the collision will be scattered back to the PC, is higher than in the case of inelastic scattering. The effect depends on the gas type, due to difference in the scattering cross-sections for various gases, on the kinetic energy distribution for photoelectrons leaving the PC as the scattering cross-sections are functions of electron energy and on the electric field strength in the vicinity of the photocathode. The photoelectron backscattering is quantitatively characterized by the photoelectron backscattering probability ε_{bs}, which is the fraction of total number of photoelectrons that scattered back to the PC and were not re-emitted. The fraction of pho-

toelectrons that surmount backscattering is called photoelectron extraction efficiency and we denote it as ε_{extr}. Obviously, the relation between extraction efficiency and backscattering probability is expressed by the simple equation:

$$\varepsilon_{extr} = 1 - \varepsilon_{bs} \,. \tag{3.11}$$

Due to backscattering, the QE of a PC operated in a gas media is less than that in vacuum. The effective quantum efficiency QE_{eff} of a photocathode operated in gas compared to the vacuum value QE can be described as follows:

$$QE_{eff} = QE \cdot \varepsilon_{extr}. \tag{3.12}$$

The photoelectron emission into gas media from UV-sensitive CsI PCs was thoroughly studied both theoretically [73] and experimentally [66, 74] in various gas mixtures and at different values of extraction field. The studies revealed that the backscattering is strong in atomic gases and less pronounced in gases with more complex molecular structure (like hydro-carbons). This is explained by the fact that in atomic gases the photoelectrons are preferably scattered in elastic collisions; the photoelectron's kinetic energy after the collision remains large enough to overcome resistance of the electric field, so that the photoelectron could return back to the PC having a very small energy, not sufficient to be re-emitted. In molecular gases the photoelectrons might lose their kinetic energy in elastic collisions with gas molecules; for some photoelectrons their kinetic energy left after the collision might be not sufficient to overcome deceleration in the electric field and they can not reach the PC. It was also shown [73] that the photoelectron extraction efficiency is a function of photon wavelength of incident radiation; the general trend was the following: the shorter the wavelength, the higher the backscattering efficiency.

There has been just one study performed so far [10] on the measurement of backscattering with visible-sensitive bi-alkali PC operated in a gas. The photoelectron extraction probability ε_{extr} as a function of electric field E_{drift} was measured for visible-sensitive K_2CsSb PC illuminated with a UV-LED at 375 nm photon wavelength in various Ar/CH_4 gas mixtures at atmospheric pressure. These results are shown in figure 3.13. An electric

field strength of at least 0.4 kV/cm is required to minimize photoelectron backscattering. It is clear from figure 3.13, that the backscattering reduces with the increase of methane concentration in the gas mixture. The studies of the photoelectron emission into gas media from visible-sensitive alkali-antimonide PCs at different illumination wavelengths were performed in the present thesis work (see section 5.1.3).

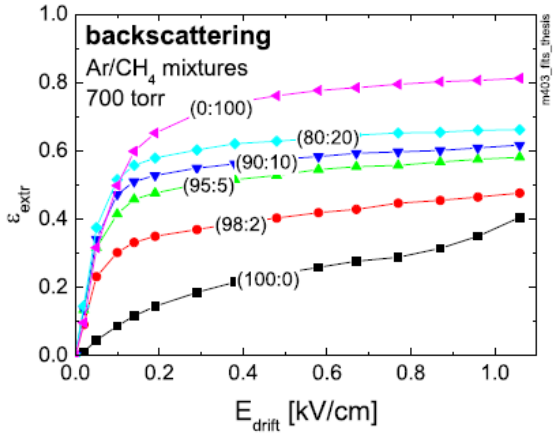

Figure 3.13: The photoelectron extraction efficiency ε_{extr} for K_2CsSb PC as a function of E_{drift} in various Ar/CH_4 mixtures. The pressure in all cases was 700 Torr. The PC was illuminated with UV-LED (peak wavelength 375 nm). Taken from [10].

3.5.2 Photon feedback

In the avalanche process a large number of ions and photons are created (figure 3.6), which are the source of yet another problem. The secondary photons impinging on the PC can induce secondary photoemission, and therefore generate new avalanches, resulting in so-called photon-feedback pulses. The intensity of the effect depends on the gas (emission wavelength) and on the spectral sensitivity of the photocathode material. The photon feedback, besides gain limitations, leads to the deterioration of the space and time accuracies. However, the photon-feedback can be significantly suppressed by a proper choice of the electron multiplier geometrical design and its operation conditions (e. g. gas filling).

It is practically suppressed in hole-multipliers: cascaded-GEMs (gas electron multipliers) [67], in GEM-cascades followed by a Microhole & Strip Plate (MHSP) multiplier [12] and in other configurations investigated in this work.

3.5.3 Ion feedback

The secondary avalanche-induced ions, drifting back to PC in opposite direction to the emitted photoelectrons, impinge on the PC surface releasing secondary electrons figure 3.6. The latter initiate secondary avalanches, known as ion-feedback, limiting the gain by diverging into discharge. **This is one of the most severe limitations of GPMs, and finding adequate solutions to it was one of the major subjects of this research.**

There are principally two ways ions can cause secondary electron emission (SEE) from photocathodes [75].

- **Kinetic Emission:** For ion kinetic energies exceeding 400-500 eV [75], impact of ions can lead to secondary electron emission (SEE). This effect is mostly observed in strong electric fields and at low pressures. At atmospheric pressure and typical applied fields of a few kV/cm, kinetic electron emission is normally not observed.

- **Auger Neutralization:** For slow ions, the SEE probability is almost independent from the ion's kinetic energy; the process is governed by the potential energy, the ionization energy E_i, of the ion. The process of neutralization can be described as follows:

$$A^+ + Ne^-_{PC} \longrightarrow A + (N-1)e^-_{PC} + e^- \tag{3.13}$$

  where A^+ denotes the incident ion, N the total number of electrons in the PC and A the neutral atom formed.

The process of Auger neutralization is the most favorable process to cause IISEE in GPMs; it was thoroughly evaluated theoretically and determined experimentally as discussed in section 5.2.

Two examples of ion feedback in a GPM comprised of a visible-sensitive K_2CsSb PC followed by a Gas Electron Multiplier (GEM) (see section 3.4.1) are shown in figure 3.14. In a single-GEM GPM, the ion back-flow is poorly suppressed; a large fraction of the avalanche ions could reach the PC initiating secondary electrons. In figure 3.14(a) the GPM was operated under illumination with light flashes of many photons; one can see a primary pulse and successive avalanche ion-induced after-pulses. In figure 3.14(b) a gain-voltage curve of the GPM operated under continuous light illumination (squares) is presented; a significant deviation from exponential behavior is observed. A gain-voltage curve for the GPM with a UV-sensitive CsI PC (triangles), for which ion feedback effects are not observed (lower emission probability) obeys usual exponential behavior (see equation 3.6 in section 3.4) is also shown for comparison.

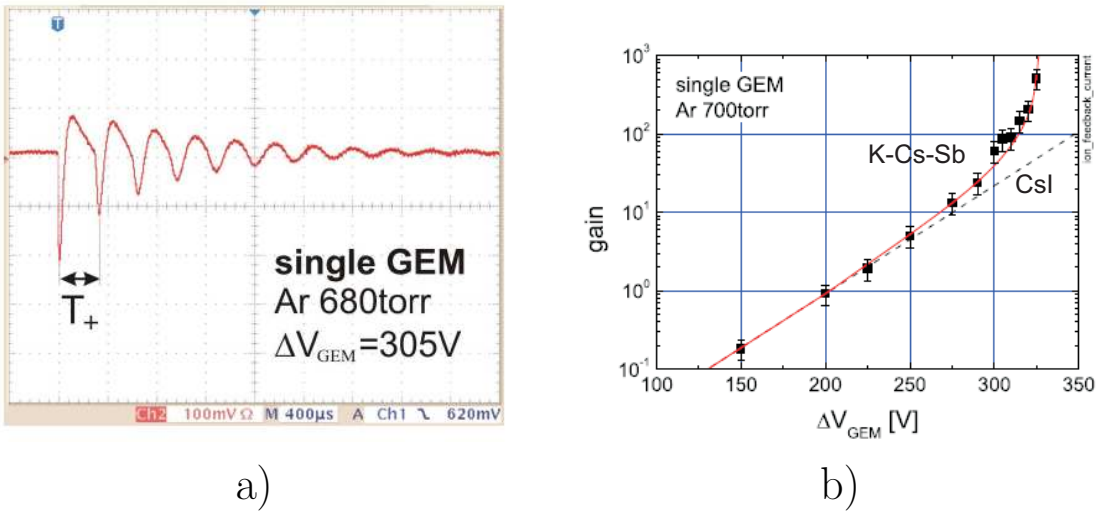

Figure 3.14: An illustration of the effect of ion feedback in a single-GEM GPM with visible-sensitive K_2CsSb PC. a) the GPM is operated in pulsed-mode illuminated with light flashes of many photons; one can see a primary pulse and successive avalanche ion-induced after-pulses. b) a gain-voltage curve of the GPM operated under continuous light illumination (squares); a significant deviation from exponential behavior is observed. A gain-voltage curve for the GPM with UV-sensitive CsI PC for which ion feedback effects are not observed obeys usual exponential behavior (dashed line). (both figures were taken from [10])

The back-flowing ions have further severe consequences, of physical and chemical damage to the PC surface, leading to the degradation of its quantum efficiency (QE) [76, 52] as discussed in the next section.

3.5.4 PC ageing

The dominant decay mechanism of photocathodes operated in GPMs is due to avalanche ions impact on the photocathode [52]. For example, it was found that semitransparent CsI PCs operated at a moderate gain of 10^3 in parallel-plate configuration lose as much as 20% of their sensitivity after an accumulated ion charge of $\sim$8 μC/mm^2 [52]. The exact nature of photocathode aging is not completely understood; obviously ion sputtering causes surface modifications and lattice defects in the photocathode that may reduce the electron escape length and modify the electron affinity. Despite the unexplained nature of ageing, it is clear that in order to reduce PC aging caused by ion impact, the flux of avalanche-ions back-flowing from the electron multiplier to the PC should be minimized.

3.6 Ion back-flow reduction in gaseous multipliers

The ion back-flow to the PC is qualitatively characterized by **Ion Back-flow Fraction** (IBF) being the average fraction of avalanche induced ions flowing back to the PC.

It was demonstrated in our previous works [13, 77] on visible-sensitive GPM that the ion back-flow and the resulting secondary feedback signals, limited the detector's gain to values in the 10^2 range. On the other hand, gains approaching 10^6 could be reached in gated bialkali/cascaded-GEM photomultipliers; the latter incorporated dedicated pulsed ion-gating electrodes that blocked the ions back-drifting towards the photocathode [76, 78]. Though inconvenient in many applications the successful pulsed-gate operation was a real breakthrough in the field of photon detection reaching IBF values of $\sim 10^{-4}$ and charge gain $\sim 10^6$ with a 4-GEM gated GPM [76]. One of the major aims of the proposed research has therefore been the **operation of gas photomultipliers in a continuous mode**.

In the continuous-operation mode, the IBF reduction in cascaded micro-hole structures required better understanding and mastering of electron and ion transport in gas media. While in vacuum, electrons and ions follow exactly the field-lines, in gas their behavior is significantly different. The electron's mass being 1000 times smaller than the ion's one, its elastic collisions with the gas molecules (at energies below ionization), will result in diffusion; therefore electrons do not follow exactly the electric-field lines. A much lower diffusion occurs with the more massive ions. The RMS of the radial charge displacement by diffusion is a function of the gas composition and the electric field; for instance, for a 1cm of drift it is about $5 \cdot 10^{-3}$ cm for Ar^+ ions and $8 \cdot 10^{-2}$ cm for electrons at electric field 5kV/cm in Argon at normal conditions (calculated using [46, 79, 80, 81, 82]). It is this large difference in diffusion that allowed for our considerable reduction of the IBF value in cascaded multipliers.

A straight forward way to reduce the IBF is by lowering the drift field, since IBF decreases linearly with the drift field [83]. However, in GPMs the drift field could not be set to low values because it controls the photoelectron extraction into the gas (see section 5.1.3); drift field values of the order of 0.5kV/cm [10] were generally applied in our GPMs filled with Ar/CH_4 (95/5).

In our previous works [10, 76] the cascaded-GEM photon detector was found to have a limited possibility of reducing the flow of back-drifting avalanche ions. The lowest IBF values reported so far with semi-transparent photocathodes, at gas gains of 10^5), were of the order of 3-5 $\cdot 10^{-2}$ at drift fields of 0.5 kV/cm [83, 84]. An operation of a 4-GEM detector with a reflective PC provided at best IBF values of $\sim$0.1 at a gain of 10^5-10^6 [78].

Attempts were made to reduce the IBF-value by thereby diverting a fraction of the avalanche ions by replacing the last GEM in the cascade with a MHSP multiplier [72]. The electric field established between the anode strips, the cathode strips and the additional cathode plane (figure 3.12(c)) blocked a large fraction ($\sim$95%) of the final-avalanche ions from back flowing through the hole, as shown in [12]. Moreover, the two-stage multiplication of the MHSP permitted further optimization of the multiplier: by setting a small transfer field above the MHSP, the flow of both ions and electrons between the GEMs and

the MHSP was reduced; the loss in gain was recovered by the additional strip multiplication in the MHSP. Using such a scheme in a gaseous photomultiplier comprising 3-GEMs, a reflective CsI PC evaporated on the top GEM and an MHSP at the end [12], the IBF value was measured to be at best $\sim 3 \cdot 10^{-2}$ at a total gain of 10^5 [12, 85]. It could be further reduced employing a semitransparent PC instead of a reflective one; with part of the back-flowing ions being diverted to the top face of the first GEM.

The optimized transfer- and induction-field configurations for a triple-GEM detector were suggested in [48, 49]. It was found that with a very low second transfer field ($\sim$ 60 V/cm) and rather high amplification in the last GEM, the IBF could be reduced down to 0.5% at a gain of 10^4 and a drift field of 0.2 kV/cm. At higher drift field of 0.4 - 0.5 kV/cm required for the efficient photoelectron extraction in GPMs (see section 5.1.3), this IBF value will be doubled as it is proportional to the drift field.

The above discussion clearly demonstrates the potential for IBF reduction by creating different paths for electrons and ions. However, as explained below (see section 5.3), even the lowest IBF-values reached so far, were by two orders of magnitude above the ones required for stable operation of visible-sensitive GPMs. This constituted the principle obstacle for development of visible-light sensitive GPMs and called for a thorough search for novel viable solutions for substantial IBF reduction.

Naturally, ion blocking should not affect the collection efficiency of the single photoelectron; this makes the task by far more complex. One should be aware that in order to achieve full detection efficiency of single photoelectrons emitted from the photocathode, or of ionization electrons radiation-induced within the drift volume, two conditions have to be fulfilled: 1) the electron's collection efficiency into the first element holes, particularly in the application to single-photon GPMs, has to be close to unity; this was indeed confirmed for GEMs [84, 69]; 2) the amount of the avalanche charge extracted from the first element in the cascade should be large enough to ensure full event's detection efficiency, including the case of exponential pulse-height distribution of single photoelectrons. The two conditions are of prime importance, because an electron lost at the first multiplication element due to inefficient focusing, insufficient multiplication or inefficient extraction cannot be

recovered.

It should be noted here that blocking avalanche ions is recognized as one of the most important general issues in gaseous avalanche detectors. E.g., in large particle-tracking detectors (like Time Projection Chambers (TPCs)), ions flowing back from the multiplier into the conversion/drift region temporarily and locally modify the electric field, resulting in dynamic track distortions [86]. This seriously affects the tracking properties of TPCs in high-multiplicity experiments, e.g. in present and future particle-collider experiments, including relativistic heavy-ion physics applications.

Chapter 4

Experimental setups and methods

4.1 Experimental setup for GPM operation in gas-flow mode with CsI PC

The experiments related to the optimization of electron multiplier's characteristics such as IBF, gain and single-electron detection efficiency were carried out in a dedicated setup with various multipliers coupled to a UV-sensitive CsI PC. The CsI PCs are quite robust, can withstand several short (few min.) exposures to air without any noticeable degradation, and are capable of operation in gas-flow mode [87]. This allows fast and frequent replacement, removal or addition of various electron multiplier elements without a significant loss in PC QE. The setups for production of CsI PCs and for operation of GPMs with CsI PCs in a gas-flow mode are described below.

The setup for GPM operation in gas-flow mode with CsI PC is shown in figure 4.1. It is comprised of an aluminium cylindrical vessel evacuated with a turbo-molecular pump to about 10^{-5} Torr; the detector is mounted on one of the flanges. The gas flow in the vessel is regulated by two mass-flow controllers (MFC1 and MFC2); alowing to modify the gas mixture. The differential gas flow is regulated by a needle-valve followed by a diaphragm-pump. The system permits automatic pressure and flow control utilizing MKS type 146A multiple-purpose control unit.

The detector elements forming the GPM are mounted on a flange, carrying also the

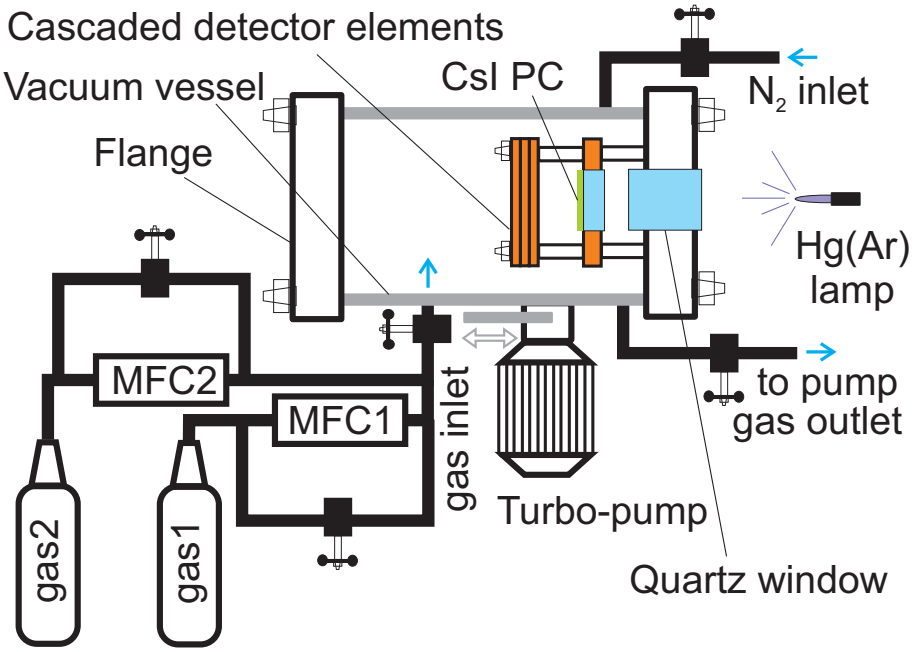

Figure 4.1: Schematic view of the experimental setup for GPM operation in gas-flow mode CsI PCs.

high-voltage feedthroughs; it has a central UV transparent quartz window for the GPM illumination with UV light. An Ar(Hg) light source was usually employed for both current recording and single photon counting operation modes. The light level of the Ar(Hg) lamp was modified by putting absorbers. The GPM could also be illuminated with fast multiple-photon flashes using a H_2 discharge lamp.

Multiplier elements were mounted onto 40 x 40 mm^2 square frames, machined from 1.6 mm thick G-10 material. Their central 28 x 28 mm^2 opening defined the active area of the detector. The MHSP and GEM electrodes studied in this work, of 28 x 28 mm^2 effective area, were produced at the CERN printed circuit workshop, from 50 μm thick Kapton foil with 5 μm copper clad on both sides. The etched double-conical 70/50 μm (outer/inner) diameter GEM holes are arranged in hexagonal pattern of pitch 140 μm figure 3.9. The MHSP pattern and dimensions are shown in figure 3.12(b). All electrodes were attached to the G-10 frames with "3M" mylar adhesive tape; their small size provided them with sufficient rigidity. Contacts to electrodes were made with thin gold-coated copper wires.

The semitransparent PCs were made of 300$\mathring{A}$ thick layers of CsI, evaporated on a UV-transparent substrate window, pre-coated with a 40$\mathring{A}$ thick Cr film. The detailed procedures for CsI and Cr films deposition are described in ref. [10]. The substrate window was embedded in a G-10 frame; the contact between the PC and the frame was established with conductive silver paint.

Individual frames with the detector elements were stacked with nylon screws; the distances between the elements could be adjusted with spacers. This modular assembly allowed for a very convenient detector modification. During the installation of the GPM and the photocathode inside the vessel, it was continuously flushed with N_2, minimizing damage to the CsI photocathode by moisture.

In the present setup, the GPM could be operated either in *continuous* illumination or in *pulsed* illumination mode. In the *continuous* operation mode, the CsI PC of the GPM was illuminated by a Hg(Ar)lamp (Ortec model 6035). Each of GPM's electrodes was biased independently with a CAEN N471A or CAEN N126 power supply. The current after multiplication was recorded on a biased electrode of the cascaded multiplier as a voltage-drop on a 40 MΩ resistor, with a Fluke 175 voltmeter of 10 MΩ internal impedance. The combined resistance was 8 MΩ, from which the recorded current was calculated. The avalanche-induced currents were always kept well below 100 nA by attenuating the Hg(Ar)lamp photon flux, to avoid charging-up effects. The currents on grounded electrodes were recorded with a Keithley 485 picoamperemeter. Detailed schemes of electrical connections are presented below for each detector configuration.

In the *pulsed* operation mode the light from the Hg(Ar)lamp was attenuated by adding some light absorbers, down to the single-photon level. Capacitively decoupled from the high-voltage bias applied to a corresponding electrode, the charge signal was recorded by the Ortec 124 charge-sensitive preamplifier followed by a pulse-shaping linear amplifier Ortec 571. The pulses were either observed on a digital oscilloscope or fed into a multi-channel analyzer (Amptek MCA2000) for obtaining pulse-height spectra. The single-photoelectron pulse-height distribution usually obeyed an exponential law, as discussed in section 3.4.

4.2 Experimental setup for production and testing of visible-sensitive GPMs

We describe below the methods and apparatus for photocathode production and characterization, detector assembly and its operation in an unsealed gas-photomultiplier prototype.

4.2.1 General overview

A dedicated, 3-chamber ultra-high vacuum (UHV) transfer system was designed and built for the production and characterization of alkali-antimonide photocathodes and their transfer to electron multipliers. The system permits to seal photocathodes to detector packages, with hot indium-bismuth alloy, as described in [10, 13]. The research results presented here were obtained in a non-sealed detector setup.

A schematic illustration and a photograph of this setup are shown in figure 4.2. The three ultra-high vacuum chambers are separated by gate valves; each chamber is evacuated by a separate turbo-molecular pump and baked out for >48 hours prior to operation. The load-lock chamber is used for introducing and baking out photocathode-substrates prior to their transfer into the second, activation chamber. Here, the alkali-metals are evaporated onto the glass substrate to form a semiconductor photocathode. In the same chamber, the QE of the photocathode is measured in-situ. In the third detection chamber, the electron multiplier is introduced, tested and baked before it is sealed, in gas, to a photocathode. The photocathode substrate is transferred between the chambers by magnetic manipulators. In this work, the detection chamber was used for the characterization of electron multipliers in combination with alkali-antimonide photocathodes - without sealing the two components. The individual elements of the system and the respective methodologies are described in detail in the following sections.

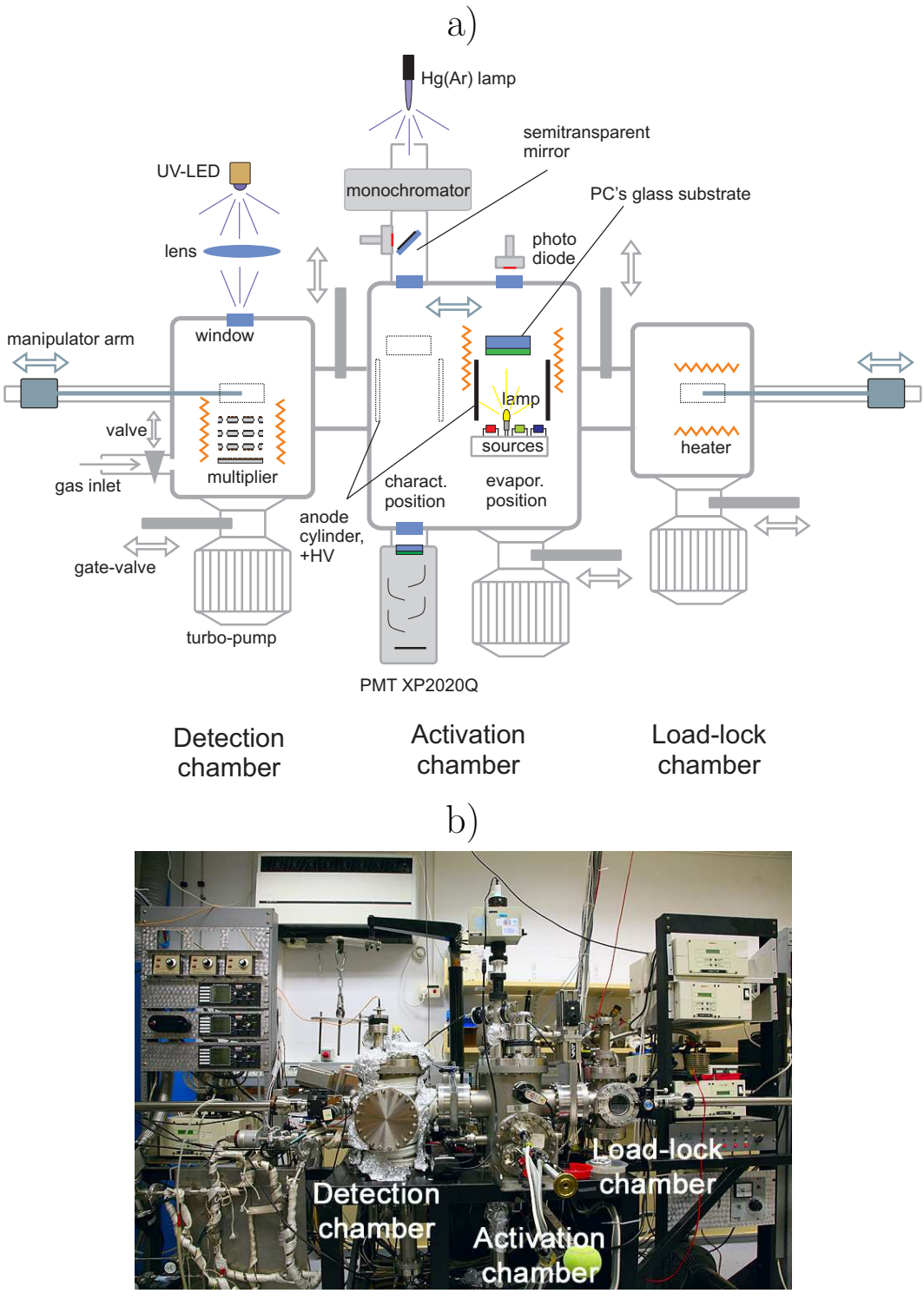

Figure 4.2: a) The 3-chamber UHV setup for gaseous-photomultiplier studies. From right to left: a *load-lock chamber* for the photocathode-substrate baking; an *activation chamber* for the photocathode preparation and characterization; the *detection chamber* for the characterization of a gaseous multiplier coupled to the photocathode (also including a detector sealing facility). b) A photograph of the UHV setup.

4.2.2 Load-lock chamber

Designed for introducing and baking out of photocathode glass-substrates prior to their transfer into the activation chamber, the load-lock chamber is baked out with internal quartz lamps up to 220^0C and is pumped by a turbo-molecular pump, backed by a dry diaphragm pump. Typically, a pressure of $\sim 5 \cdot 10^{-8}$ Torr is reached after a bake-out at 200^0C for 48 hours. The temperature of the chamber is monitored by a thermocouple, which is positioned in the vicinity of the photocathode holder.

4.2.3 Activation chamber

Photocathode production and characterization takes place inside the activation chamber. It is baked out internally by quartz lamps before photocathode production and pumped by a turbo-molecular pump backed by a scroll pump. A base pressure of $3 \cdot 10^{-10}$ Torr is typically reached after a bake-out at 250^0C for 48 hours. Additional quartz lamps are located close to the photocathode substrate holder and allow for local heating during the photocathode production process. The temperature in the chamber is monitored with thermocouples placed close to the substrate holder.

The *evaporation position* (figure 4.2(a)) consists of three separate evaporation stations placed on a moving arm; each of them permits the production of two-three bi-alkali photocathodes. Each station contains Sb, K and Cs (or Na) evaporation sources and a small incandescent lamp used for light transmission measurement during the photocathode processing. Antimony shot is placed in a small Ta evaporation boat and pre-melted in high vacuum before installation in the activation chamber. K, Cs and Na evaporation sources are provided by the manufacturer (SAES Getters S. p. A.) in form of small dispensers, three of each are interconnected in series by spot-welding and are placed in the respective source holders. All sources are out-gassed during the bake-out process by resistive heating. A shutter above the evaporation sources allows quick terminating the evaporation during photocathode processing. A sapphire window in the activation chamber above the evaporation position allows the illumination of the photocathode during processing (figure

4.2(a)).

The *characterization position* (figure 4.2(a)) allows the in-situ measurement of the absolute QE of the photocathode: a calibrated photomultiplier operated in photodiode mode (gain=1) is placed on the sapphire window below the characterization position, a monochromator is placed on the top sapphire window. A Hg (Ar) lamp is used as light source for the monochromator; it exhibits narrow spectral lines in the sensitivity range of bi-alkali photocathodes (254.6, 312.5, 365.0, 404.6, 435.8, 546.0 nm). A fraction of the light on the path from the monochromator to the sapphire window is reflected by a semi-transparent mirror onto a photodiode; the role of the latter is to monitor eventual light intensity fluctuations of the Hg(Ar)-lamp.

Inside the activation chamber, the substrate and its holder are placed on top of a glass cylinder with a cylindrical stainless steel anode inside. The PC substrate in the evaporation position is shown in figure 4.3(a). In some cases, a fine stainless steel mesh can be placed on top of the anode cylinder (figure 4.3(a)), e.g. for creating a high homogenous electric field to reach charge multiplication for photocathode-aging studies (see section 5.1.4). The substrate together with the anode can be displaced between the evaporation and characterization positions of the activation chamber by means of a small manipulator arm. The glass cylinder confines the evaporation vapors, preventing contamination of the chamber and protecting the photocathode form eventual pollutants out-gassing from the vacuum-chamber walls. The photocathode-holder and the anode-cylinder are electrically connected to the outside of the chamber for current measurements or for applying a high voltage.

4.2.4 Detection chamber

The detection chamber is baked out externally by heating tapes and internally by quartz lamps; it is evacuated by a turbo-molecular pump backed by a dry scroll pump. An additional titanium sublimation pump was often used to further improve the vacuum, particularly for reducing the partial pressure of water. A base pressure of $5 \cdot 10^{-9}$ Torr

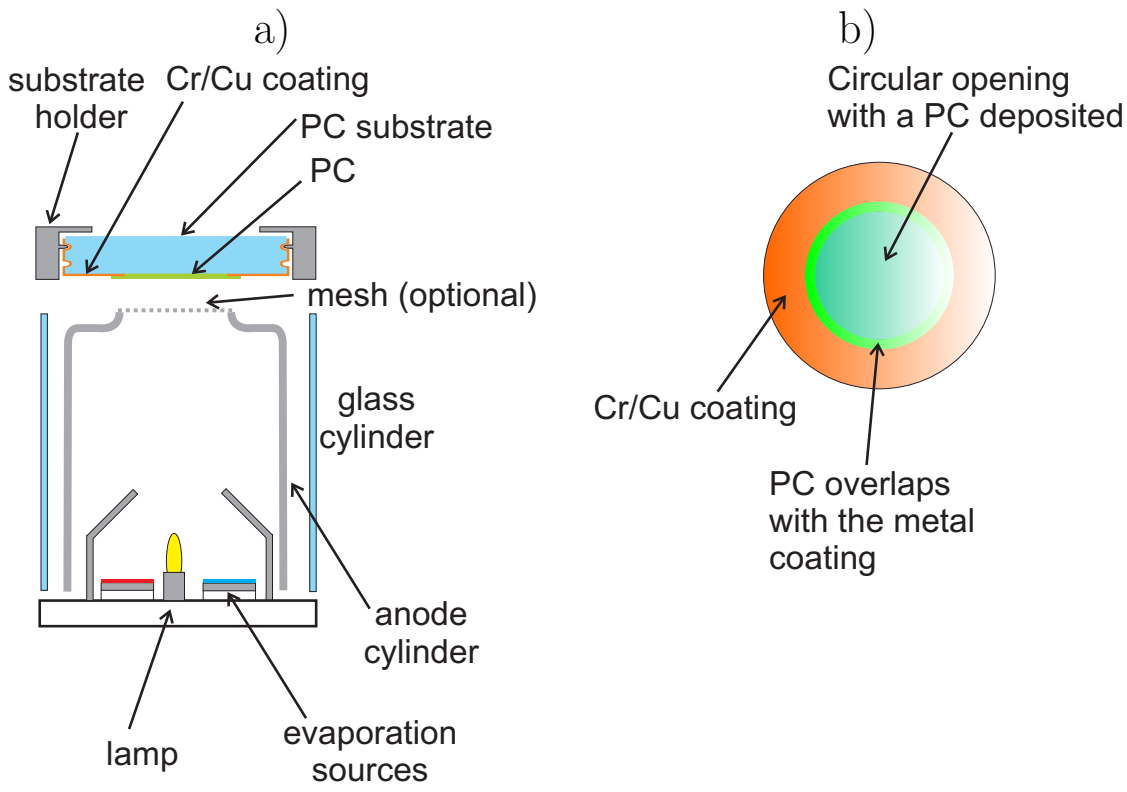

Figure 4.3: a) Schematic side view of the photocathode (PC) substrate placed in the evaporation position within the activation chamber. The PC substrate is shown with the Cr/Cu metal coating to provide electrical contact between the PC and the substrate holder; it has grooves for a good grip of the PC substrate by the substrate-holder. b) Sketch of the top view of the PC substrate showing the metal contact and the evaporated PC surface.

was typically reached after a 3 days of bake-out at 160^0C. A residual gas analyzer (SRS model RGA200) monitored the vacuum quality. The detector package was fixed to a dedicated holder, establishing the electrical contacts between the detector's electrodes to the electrical feedthroughs to external electronic circuitry. The photocathode-detector assembly was illuminated from top through a quartz window. The detector assembly within the detection chamber is shown in figure 4.4. This detector assembly is different than the one described in [13]; it does not allow for detector sealing.

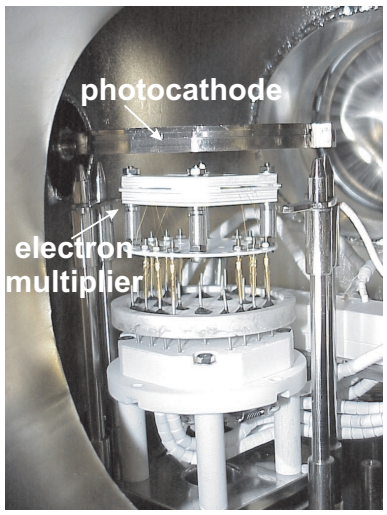

Figure 4.4: A photograph of the detector-holder, the multiplier-assembly and the photocathode - as mounted within the detection chamber.

4.2.5 Gas system

The gas system allows filling the detection chamber with high-purity two-component gas mixtures. Prior to gas filling, the gas manifold is evacuated for 48 hours with a turbo-molecular pump, under bake out at 200^0C, down to $3 \cdot 10^{-6}$ Torr. The gas flow and the mixture ratio are regulated by mass-flow controllers. In all experiments Ar of 99.9999% purity and CH_4 of 99.9995% purity were used, filled into the detection chamber through a filter; the latter (GateKeeper 35K, Aeronex Inc.) is capable of purifying noble gases, N_2 and CH_4 to ppb levels at a maximum flow of 1 liter per minute.

4.2.6 The electron multiplier

The cascaded electron multiplier, mounted in the detection chamber, comprised of GEM, MHSP and Cobra elements, of 28 x 28 mm^2 effective area, produced at the CERN printed circuit workshop, from 50 μm thick Kapton foil with 5 μm Au-coated copper cladding on both faces; their dimensions are shown in figure 3.9, figure 3.12 and figure 5.19 correspondingly. All the components of the multiplier were UHV-compatible, including MHSP

and GEM electrodes; the latter are known to be compatible with bi-alkali PCs, at least for over few months [13]. The multiplier elements were held in place and separated from each other by 1 mm thick alumina-ceramic frames with a central opening of 20 x 20 mm^2, defining the active area of the electron multiplier. Details about the detector-components mounting can be found in [10].

Three adjustable voltages were supplied to the MHSP, F-R-MHSP and Cobra electrodes and two to the GEM electrode, all tuned to provide the multiplication fields inside the holes and the appropriate voltage drop between the strips. They were connected independently to HV power supplies (type CAEN N471A) through 40MΩ resistors; the PC was kept at ground potential. The assembled multiplier was mounted on a holder in the detection chamber of the UHV system as shown in figure 4.4.

Following the introduction of the multiplier into the detection chamber, the entire system was baked at 160^0C for 5 days in high vacuum; the temperature was limited by the multipliers' Kapton substrate. After the PC deposition and characterization in the activation chamber in vacuum, both the activation and detection chambers were filled, through the purifier, with Ar/CH_4 (95/5) gas mixture to a pressure of 700 Torr. The PC substrate was transferred in-situ and placed at 8 mm above the multiplier's top element with a linear manipulator.

The GPM investigations in the detection chamber were carried out with a UV-LED light source (NSHU590A, Nishia Corp.), whose narrow spectral emission around 375 nm coincides with the sensitivity peak of mono- and bi-alkali photocathodes. The LED's light was transmitted with an optical fiber and focused onto the PC of the GPM by means of a small lens through a quartz window. The GPM could be operated either in *continuous* illumination mode or in *pulsed* illumination mode depending on the powering scheme of the UV-LED.

In the *continuous* illumination mode, a forward bias was applied to the UV-LED. The current after multiplication was recorded on a corresponding biased electrode of a cascaded multiplier as a voltage-drop across a 40 MΩ resistor, with a Fluke 175 voltmeter having 10 MΩ internal impedance. The combined resistance was 8 MΩ, from which the anode

current was calculated. The avalanche-induced currents were always kept well below 100 nA by attenuating the UV-LED photon flux, to avoid charging-up effects. The currents on grounded electrodes were recorded with a Keithley 485 picoamperemeter.

The *pulsed* illumination mode was realized by applying short voltage pulses to the LED; the emitted light intensity could be conveniently controlled by adjusting the height and width of the voltage pulses and/or adding light absorbers, down to the single-photon level. The UV-LED was powered by a pulse generator (Hewlett Packard 8012B) with square pulses having typically an amplitude of 6 V, a width of 2 μs, a period of 1 ms and rise and fall times of about 10 ns. Capacitively decoupled from the anode high voltage, the charge signal was recorded by a charge-sensitive preamplifier (typically ORTEC 124) followed by a pulse-shaping linear amplifier (ORTEC 571). The pulses were either observed on a digital oscilloscope or fed into a multi-channel analyzer (Amptek MCA2000), providing pulse-height spectra.

4.3 Fabrication and characterization of the semitransparent alkali-antimonide PCs

The production of K_2CsSb photocathodes in laboratory conditions was successfully established in our group [10, 13, 25] and by others [88]. It requires a careful choice and design of the experimental equipment and materials used within the vacuum chambers, due to the high chemical reactivity of alkali-antimonide photocathodes. UHV conditions with very low residual-moisture content are required for the successful production of stable high-QE photocathodes. The dedicated system described above allows for the production of several semi-transparent Cs_3Sb or K_2CsSb or Na_2KSb photocathodes per week.

The detailed procedures of Cs_3Sb, K_2CsSb and Na_2KSb photocathodes fabrication presented below, were optimized and continuously refined - resulting in high-QE photocathodes with good reproducibility.

4.3.1 PC substrate preparation

The photocathode substrate is made from Kovar-glass, ø 64 x 5 mm thickness. Its thermal expansion coefficient matches that of the Kovar-made detector packages, previously used for sealed GPMs [13]. Two grooves were machined on the window's edge, required for fixing it to the stainless-steel substrate-holder (figure 4.3(a)). A thin metal layer with a 20 mm circular opening in the center was evaporated onto one of the substrate's faces and onto the substrate's edge (figure 4.3(a) and figure 4.3(b)); it provided electrical contact to the photocathode (deposited on the central non-metallized surface); in sealed GPMs, it was required for sealing the substrate to the Kovar package. The metal layers were electron-gun deposited in vacuum; they comprised a first chromium (100 nm) film, covered by a copper (200 nm) one; the metal sources had purity of 99.999%. The photocathode partly overlapped with the metal, ensuring good electrical contact (figure 4.3(b)). Following evaporation, the windows were either immediately installed in the load-lock chamber or stored under vacuum. The photocathode substrates were mounted in their dedicated holders during the whole process of photocathode production and characterization, including their positioning above the multiplier within the detection chamber. The holder permitted transporting the substrate among the three chambers with the magnetic manipulators.

The substrate was first baked in the load-lock chamber, under vacuum, by the internal quartz lamps at $> 200^0$C for 48 hours. After cooling to room temperature, the baked substrate was transferred into the activation chamber with the magnetic manipulator at a pressure of typically $5 \cdot 10^{-8}$ Torr.

It was first placed in the characterization position and its light transmission characteristic was evaluated (figure 4.5), as required for the calculation of the photocathode's absolute QE. The substrate was illuminated by the monochromator and the light transmitted through the substrate was measured with the PMT. The photocurrent $I_{PMTtrans}(\lambda)$ was recorded by the Keithley 485 picoamperemeter for the different characteristic wavelengths of the Hg (Ar)-lamp; the lamp's intensity was monitored by the photodiode current $I_{PDtrans}(\lambda)$, used for photon-flux compensation if required.

4.3.2 Cs_3Sb photocathodes

The production process of Cs_3Sb PC's is rather simple; it consists mainly of the activation of a thin antimony film in cesium vapors at high temperature. The first step was the evaporation of an antimony film onto the PC substrate. Prior to this step, the substrate was heated to 170-180^{0}C by the internal quartz lamps; after reaching this temperature, the heating was switched off. A photodiode was then placed on the top sapphire window, illuminating the photocathode substrate from below with the incandescent lamp of the evaporation station (figure 4.3(a) and figure 4.2). The initial photodiode current recorded defined the substrate's transmission (I_0). By applying a current through the dispenser antimony was evaporated onto the substrate; it was empirically found, that an optimal thickness of the antimony film corresponded to a reduction of the substrate's light transmission to about 75-85% of its initial value I_0 measured before deposition. Once the transmission dropped to that level, the evaporation was terminated. Prior to cesium evaporation, the monitoring photodiode was replaced by a Ar(Hg)-lamp, illuminating the photocathode substrate from above; alternatively, the UV-LED, whose narrow spectral emission around 375 nm roughly coincides with the sensitivity peak of mono- and bi-alkali photocathodes, was used. The use of the UV-LED allows better focusing of the incident light onto the PC's active area and provides less light reflected at various inner chamber parts be incident on the PC. During Cesium evaporation, the PC substrate was connected to a picoampermeter for monitoring the photocurrent I_{PC}. The photoelectrons were collected at the anode cylinder located below the PC substrate, biased at 300V (figure 4.3(a) and figure 4.2). Sb activation with Cs vapors was carried out at a substrate temperature of 150-180C; it lasted until a maximum photocurrent value was reached; usually the photocurrent tended to drop rapidly at this point. Experience showed that if the Cs dispenser's power is stopped (with the shutter kept open) before a 10-30% drop of the PC current, the latter will return to its maximal value. In some cases, the PC current did not reach its maximum value after Cs evaporation was stopped, indicating an overdose of Cs. Cesium excess could be removed by heating up the PC substrate to 180-200^{0}C; the heating was stopped when the PC current

returned to its maximal value. An alternative method for Cs_3Sb PC production consisted of evaporating an excessive amount of Cs, followed by photocurrent maximization by heating the substrate. After Cs evaporation, the PC was cooled down to about 150^0C and was kept at this temperature for about 20 minutes, monitoring its photocurrent. The last step permitted forming the semiconductor-PC structure. In cases where during this process the PC current dropped, it could be re-gained by some additional evaporation steps of Sb and/or Cs.

The Cs_3Sb PCs are characterized by rather low surface resistance of about $3 \cdot 10^7$ $\Omega/\square$ [27] as compared to that of other alkali-antimonide PCs. Note that, if the resistivity of the photocathode material is ρ, for a square of side dimension d, and thickness t, the resistance R is given by

$$R = \frac{\rho \cdot d}{d \cdot t},$$

where $d \cdot t$ is the cross-section area. Thus, the resistance per square $\Omega/\square$ is independent of the side dimension. The low surface resistance is an attractive feature, if large-area active surface is required; though, the dark emission current of about 0,3 fA/cm^2 [27] is higher compared to other alkali-antimonides.

4.3.3 K_2CsSb photocathodes

The production technology of K_2CsSb PC is considerably more complex then that of Cs_3Sb; however, due to their lower ($\sim$10-fold) by thermo-emission currents ($\leq$0.02 fA/cm^2 [27]) and higher quantum yield ($\sim$40% at 370-410 nm), these PCs are widely employed in photon detectors. A drawback of K_2CsSb is the high surface resistance ($6 \cdot 10^9$ $\Omega/\square$ [27]); a transparent conductive film or a conductive grid should be deposited onto the PC substrate prior to the evaporation of large-area photocathodes.

The first step in their production process is similar to that of Cs_3Sb. A thin Sb film was evaporated onto the substrate as described above. Then the photodiode on the top quartz window (figure 4.2(a)) was replaced by a Ar(Hg)-lamp or a UV-LED illuminating

the photocathode substrate from above. During potassium evaporation, the substrate was constantly kept at 170-200^{0}C, with quartz lamps. By applying high current (4-5 A) to the K-dispensers, potassium was evaporated onto the photocathode substrate, forming a K_3Sb photocathode of which the photocurrent was monitored. Following 1-3 minutes of evaporation, the photocurrent, and therefore the QE of the K_3Sb PC, reached a plateau and eventually started dropping. Experience showed that a sufficient K amount was deposited when I_{PC} dropped to $\sim 90\%$ of its maximum value. The formation of the K_3Sb PC was followed by cesium activation.

There are several methods of activating K_3Sb with cesium vapors. One of them consists of keeping the K_3Sb PC at 250-280^{0}C for 5-10 min in order to decrease the amount of potassium in the PC, leaving room for cesium atoms. It is followed by cesium evaporation at 160-180^{0}C, until I_{PC} reaches a peak; the process is terminated when I_{PC} drops to $\sim 90\%$ of its maximum value. The formation of the K_2CsSb compound continues for some time after the evaporation is stopped; the resulting increase in QE is reflected by a rising photocurrent I_{PC}, typically exceeding (by 10-20%) the maximum value reached during the evaporation process. Repeated Cs evaporation steps (so called yo-yo treatment) usually yielded considerably higher QE values compared to a single evaporation step.

An alternative method based on exposing the K_3Sb PC alternately to cesium and antimony (the yo-yo technique) at 180-220^{0}C until the maximum photocurrent is reached. A combination of both methods is also possible.

During the study, we could not found any considerable advantage of one production method over the other one and the two methods permitted fabrication of highly efficient PCs.

Another method for fabrication of K_2CsSb PCs is so-called co-evaporation process [88]. In this method, the K_3Sb PC is formed by simultaneous evaporation of K and Sb; then it is treated in Cs vapor until the maximum photocurrent is reached. Our present setup does not permit using of co-evaporation process.

4.3.4 Na_2KSb photocathodes

The Na_2KSb PC is known for a number of unique properties like very low thermo-emission ($\leq 10^{-19}$ A/cm^2 [27]), capability of operating at high temperatures, up to 200^0C, and the lowest-known surface resistance of $\sim 2 \cdot 10^5$ $\Omega/\Box$ among alkali-antimonides. Its production technique is quite similar to that of K_2CsSb described above. The difference is in the last stage; after the formation of K_3Sb one proceeds with the evaporation of sodium instead of cesium. It is carried out at 220^0C, carefully monitoring the PC current. Once it rises up, the process of replacement of potassium atoms in K_3Sb with sodium ones takes place. This process is hard to control. Sometimes we found it difficult to stop it at the optimal ratio of 1:2 between K and Na atoms. Therefore, Na evaporation should be stopped upon a decrease in the speed of the photocurrent rise; an excess of Sodium will result in a poor-quality PC. In the following step, one proceeds with alternating (yo-yo) additions of antimony and potassium at 160-180^{0}C, until reaching the maximum photocurrent value. The formation of the Na_2KSb compounds continues for some time after the evaporation is stopped. It should be kept for some 20-30 minutes at 150-160^{0}C.

4.3.5 Photocathodes characterization

After the photocathode has cooled down to room temperature (typically 10 hours in vacuum), it is moved to the characterization position and a positive voltage of 300 V is applied on the anode's cylinder (figure 4.5). The photocathode is illuminated from above with the monochromator (figure 4.5); its photocurrent, $I_{PC}(\lambda)$ and that on the reference photodiode, $I_{PD}(\lambda)$, are measured as a function of the wavelength. The absolute QE is given by the following relation:

$$QE(\lambda) = \frac{I_{PC}(\lambda) - I_{PC}^{dark}}{I_{PMTtrans}(\lambda) - I_{PMTtrans}^{dark}} \cdot \frac{I_{PDtrans}(\lambda) - I_{PDtrans}^{dark}}{I_{PD}(\lambda) - I_{PD}^{dark}} \cdot T_W(\lambda) \cdot QE_{PMT}(\lambda) \quad (4.1)$$

where

$QE(\lambda)$ - photocathode quantum efficiency

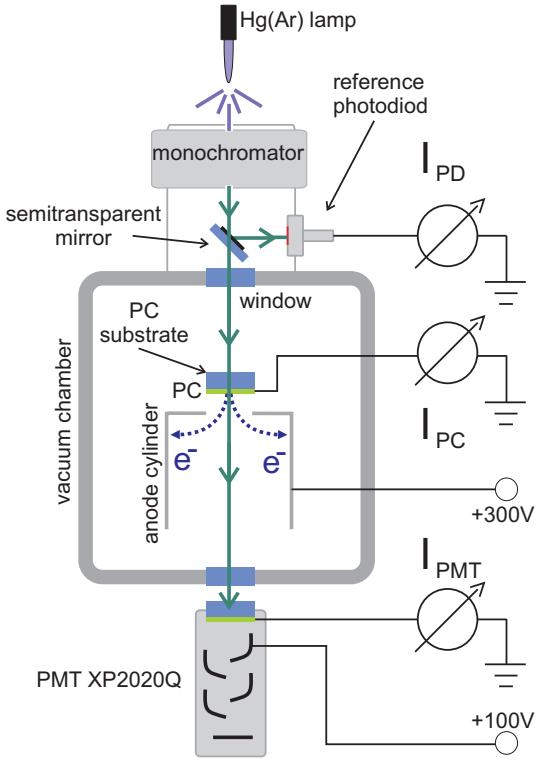

Figure 4.5: Schematic illustration of the setup for PC characterization. The PC substrate transparency is measured in the same setup prior to the PC evaporation.

$I_{PC}(\lambda)$ - photocurrent measured on the photocathode

I_{PC}^{dark} - dark-current measured on the photocathode with the monochromator lamp switched off

$I_{PD}(\lambda)$ - current measured on the monitoring photodiode

I_{PD}^{dark} - dark-current measured on the monitoring photodiode with the monochromator lamp switched off

$I_{PMTtrans}(\lambda)$ - current on the PMT from the substrate's transmission measurement

$I_{PMTtrans}^{dark}$ - dark-current on the PMT from the substrate's transmission measurement with the monochromator lamp switched off

$I_{PDtrans}(\lambda)$ - current on the monitoring photodiode from the substrate's transmission measurement

$I_{PDtrans}^{dark}$ - dark-current on the monitoring photodiode from the substrate's transmission

λ [nm]	312	365	405	435	546
QE_{PMT} [%]	28.22	29.38	28.00	24.74	6.29
T_W	0.8	0.8	0.8	0.8	0.8

Table 4.1: XP2020Q PMT quantum efficiency and light transmission through the sapphire window for the characteristic wavelengths of the Hg(Ar)-lamp.

measurement with the monochromator's lamp switched off

$QE_{PMT}(\lambda)$ - mean PMT quantum efficiency as supplied by manufacturer (see table 4.1)

$T_W(\lambda)$ - sapphire window light transmission as supplied by manufacturer (see table 4.1)

From the XP2020Q PMT current one calculates the light transmission $T_{PC}(\lambda)$ of the photocathode, as follows

$$T_{PC}(\lambda) = \frac{(I_{PMT}(\lambda) - I_{PMT}^{dark})/(I_{PD}(\lambda) - I_{PD}^{dark})}{(I_{PMTtrans}(\lambda) - I_{PMTtrans}^{dark})/(I_{PDtrans}(\lambda) - I_{PDtrans}^{dark})}. \tag{4.2}$$

where $I_{PMT}(\lambda)$ is the current on the PMT measured without the PC substrate.

Chapter 5

Results

5.1 Alkali-antimonide photocathodes

The development of efficient visible-sensitive GPMs required mastering the in-house production technology of alkali-antimonide PCs and understanding their operation in gas environment. In the following section, the PC operation in vacuum and in gas is discussed for various alkali-antimonide PCs produced in our laboratory.

5.1.1 Photoemission characteristics of alkali-antimonide PCs produced in our laboratory

In figure 5.1 we present typical plots of QE (measured in vacuum) vs wavelength for our Cs_3Sb, K_2CsSb and Na_2KSb PCs in the spectral range between 313 nm and 546 nm. The 5% error indicated in the plots is due to a discrepancy in catalog QE values for the reference PMT. The distribution of the peak (highest) QE-values of a large number K_2CsSb photocathodes prepared in our setup is shown in figure 5.2; it indicates the fluctuations in the photo-emissive properties, with an average QE of about 28%. As can be seen in figure 5.2, out of 28 PCs produced, 23 had QE-values exceeding 20%; the 5 PCs with QE below 20% were mostly produced at the early stages of our studies, before mastering the production technology. The QE values increased at later stages: most of the PCs had over 20% QE; some of them had values close to 50% at a wavelength of 360-380 nm. Beside

K_2CsSb PCs, we also produced 6 Na_2KSb PCs with peak QE varying from 15 to 25% and 7 Cs_3Sb PCs with peak QE varying between 10 to 40%.

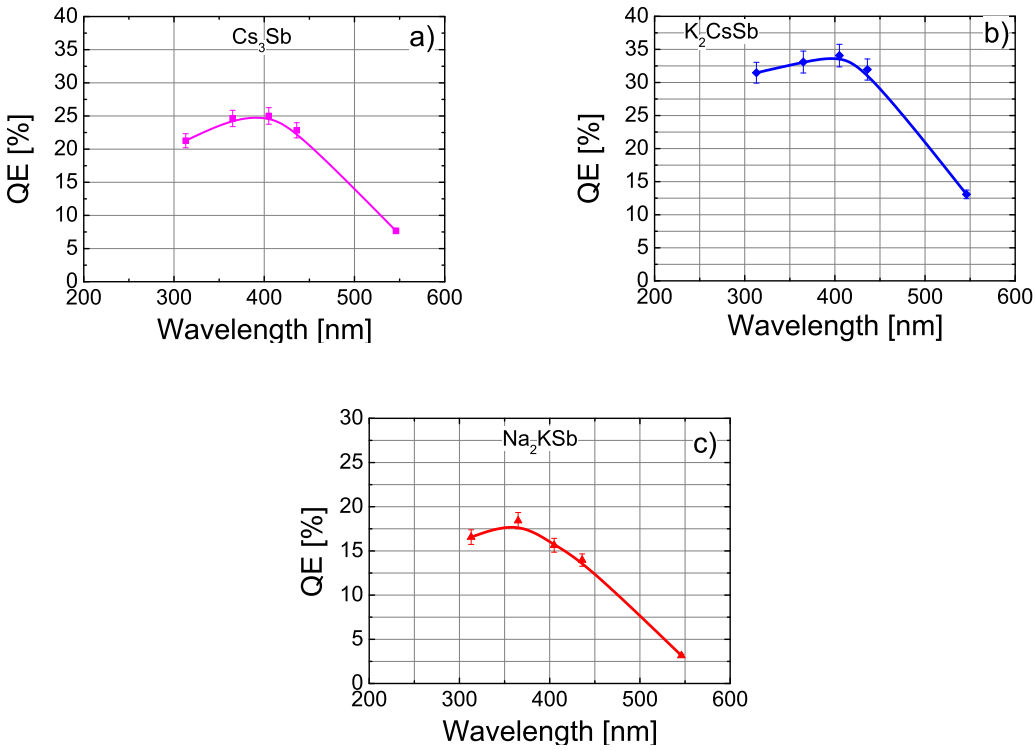

Figure 5.1: Typical QE vs wavelength plots measured in vacuum for Cs_3Sb a), K_2CsSb b) and SbK_2Na c) produced in our laboratory.

The thicknesses of different PCs can be compared by measuring their light transmission $T_{PC}(\lambda)$. In figure 5.3, two photocathodes with different thickness are compared; the thicker PC has lower light transmission as compared to the thinner one. The difference in the PC thicknesses resulted in a variation of the photoemission properties. The thicker PC had better response in the green spectral region, while the thinner PC was more sensitive in the UV-range. The peak QE of the thicker PCs is shifted towards the red while the peak QE of the thinner PCs is shifted towards the UV-region.

It is interesting to compare our PCs with that of leading PMT manufacturers. In figure 5.4, the QE vs wavelength plots are presented for newly developed high QE "Super

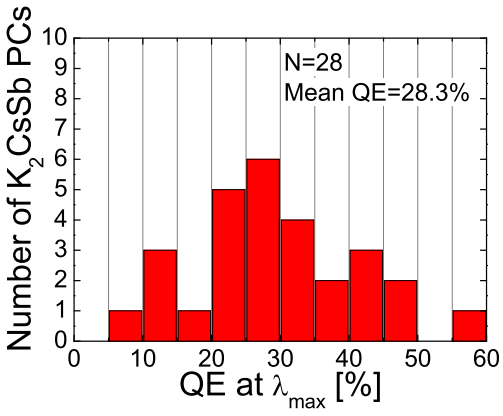

Figure 5.2: Distribution of the peak quantum efficiency values of K_2CsSb PCs prepared in our lab; the average QE of all the produced PCs is about 28% (at wavelengths of 360-400 nm)

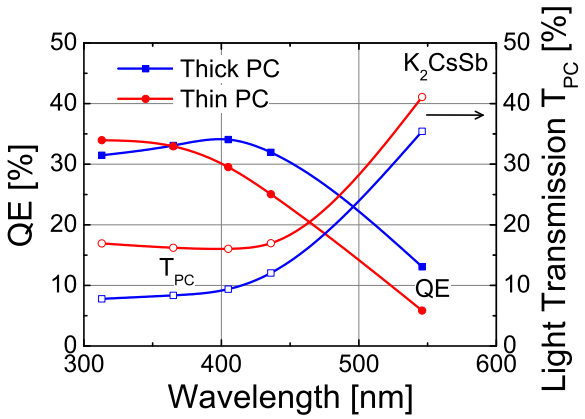

Figure 5.3: QE vs wavelength plots for thick and thin K_2CsSb PCs. The light transmission as a function of wavelength $T_{PC}(\lambda)$ for each PC is also presented.

Bi-Alkali" (SBA) and "Ultra Bi-Alkali" UBA PCs by Hamamatsu Photonics Inc. [26] in comparison with those for the K_2CsSb PCs produced in our laboratory. The best K_2CsSb PC ever made in our UHV setup had a peak QE approaching 58% (figure 5.4) at 365 nm; **this peak QE value probably constitutes a world record for bi-alkali PCs**.

Despite the fact, that the photoemission characteristics of some our PCs superior to those produced by Hamamatsu, it has to be mentioned that the reproducibility of high-QE ($> 40\%$) PCs is rather low. This could be attributed to a rather poor manual control of

the fabrication process. Though, the reproducibility of moderate-QE PCs (between 30% and 40%) is quite high; out of 10 K_2CsSb PCs recently produced in our lab, 8 had peak QE exceeding 30%.

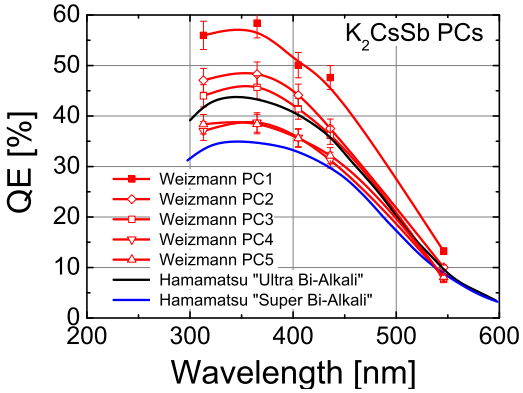

Figure 5.4: QE (in vacuum) vs wavelength plots for K_2CsSb PCs produced in our lab compared with those for SBA and UBA of Hamamatsu (taken from [23]).

5.1.2 Photocathodes stability in gas media

The present Cs_3Sb and K_2CsSb PCs were found to be stable when kept in the activation chamber filled with high-purity Ar/CH_4 (95/5) at 700 Torr, for about a month. figure 5.5 shows the evolution in time of the QE in Ar/CH_4 (95/5) of a Cs_3Sb PC figure 5.5(a) with an initial vacuum QE-value of ∼25% and of a K_2CsSb PC figure 5.5(b) with an initial vacuum QE-value of ∼30%. As shown in figure 5.5, no appreciable change in QE was observed after 28 days for the Cs_3Sb PC. The K_2CsSb PC was stable in gas for 83 days two months without any noticeable PC degradation. The small decrease in QE observed, is within the measurement accuracy. A sealed device is naturally expected to have very low impurity-levels and thus, even better stability.

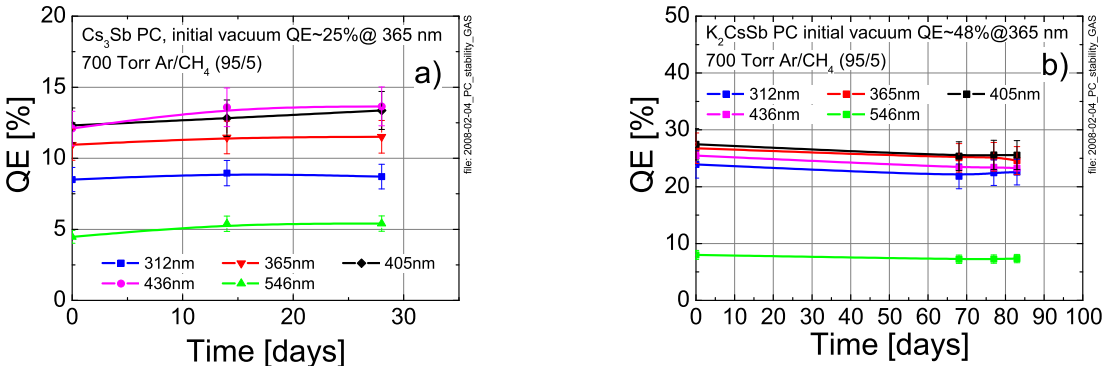

Figure 5.5: The time-evolution of the QE at different wavelengths of Cs_3Sb a) and K_2CsSb b) photocathodes in high purity Ar/CH_4 (95/5) at 700 Torr.

5.1.3 Photoemission from the photocathodes into gas media

The efficiency ε_{extr} of electron extraction from the PC or the fraction of photoelectrons surmounting the backscattering on gas molecules was measured in the experimental setup of figure 4.5 with a fine stainless steel anode mesh placed on top of the metal cylinder to provide a uniform electric field in the gap between the PC and the mesh. The electric field was established in the gap by applying positive voltage to the mesh. The extraction efficiency was derived as a ratio of photocurrents recorded at the PC in gas and in vacuum. The K_2CsSb PC was illuminated with a monochromatic light of various wavelengths.

The dependence of ε_{extr} on the electric field in the Ar/CH_4 (95/5) mixture and in pure CH_4 both at 700 Torr was measured for photon wavelengths 254.6, 312.5, 365.0, 404.6, 435.8 and 546.0 nm (figure 5.6). As expected, in pure CH_4 the backscattering probability is lower, resulting in higher ε_{extr}. Above field values of 500 V/cm the extraction efficiency ε_{extr} raised moderately; this value was chosen in all gases for subsequent measurements and the corresponding ε_{extr} could therefore be assumed constant throughout the measurements.

The variation of photoelectron extraction with photon wavelength at a constant electric field is shown in figure 5.7. At an electric field of 500 V/cm, the ε_{extr} values for K_2CsSb PCs into Ar/CH_4 (95/5) at 700 Torr range between ~40% at 313 nm and ~80% at 546 nm.

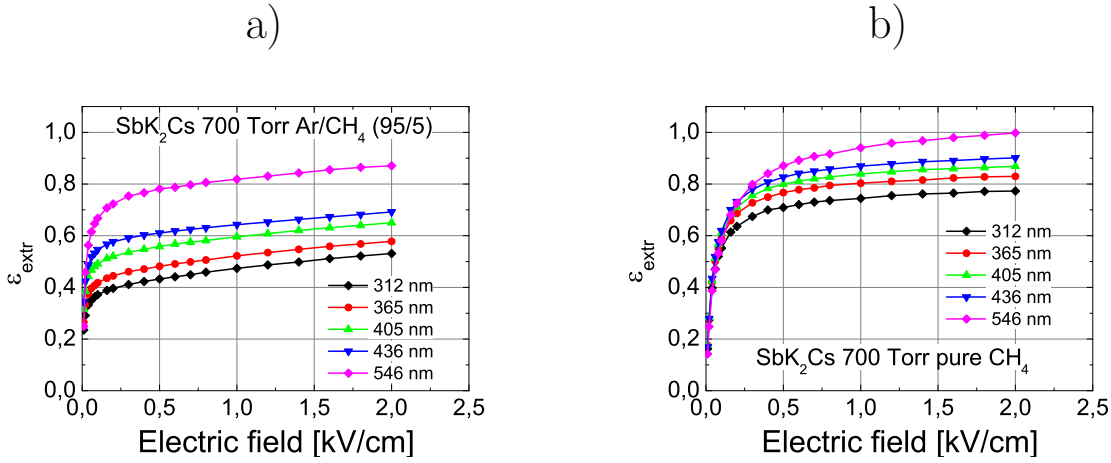

Figure 5.6: The extraction efficiency ε_{extr} as a function of electric field for the Ar/CH_4 a) mixture and pure CH_4 b) measured at various photon wavelengths. The pressure in all cases was 700 torr.

The QE distribution in vacuum and the effective QE in gas (corrected for backscattering) are depicted.

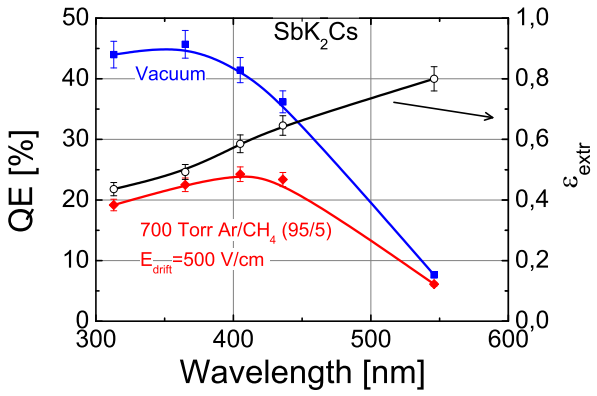

Figure 5.7: An illustration of photoelectron backscattering effect in 700 Torr Ar/CH_4 (95/5) gas at an electric field of 500V/cm for a K_2CsSb PC. The QE was measured as a function of wavelength in vacuum (squares) and in the gas (diamonds). The fraction ε_{extr} of photoelectrons surmounted backscattering as a function of photon wavelength is also presented (open circles).

5.1.4 Photocathode ageing under gas avalanche

The ageing of semitransparent K_2CsSb PCs under avalanche-ion impact is of great concern in visible-sensitive GPMs, and was recently investigated. For each PC, the QE was measured upon production, in vacuum and then in the high-purity gas; the photocathode was coupled either to a 4-GEM multiplier or to a single-mesh electrode which formed a parallel-plate multiplier. The number of ions hitting the PC in each configuration was tuned by varying the multiplier's gain. The PC was illuminated with a focussed UV-LED light (375 nm) at a photon flux of $3 \cdot 10^9$ photons/(mm^{2}s). Photocurrent measurements at two separate spots on the PC, one illuminated and subject to avalanche-ion flux and the other obscured, provided the ion-induced aging - corrected for the decay by chemical processes due to gas impurities. Each ageing measurement lasted for the time required to accumulate 10-20 μC/mm^2 ion charge at the photocathode. Aging results of the K_2CsSb PCs coupled to a 4-GEM cascaded multiplier operated in 700 Torr of Ar/CH_4 (95/5) mixture and in parallel-plate multiplier configuration operated in 100 Tor with the same mixture are presented in figure 5.8. A decay of CsI PC under avalanche-ion bombardment in a parallel-plate detector is also presented for comparison. In the case of 4-GEM GPM, the photocurrent (the QE) decayed to ∼80% of its initial value after an accumulated ion charge of ∼2 μC/mm^2, while in the case of parallel-plate GPM the ∼80% drop of photocurrent was observed after an accumulated ion charge of ∼1μC/mm^2 at the PC. With the CsI PC, similar decay occurred at ∼10μC/mm^2.

5.1.5 Discussion on alkali-antimonide PCs

We described in details the deposition methods of Cs_3Sb, K_2CsSb and Na_2KSb photocathodes, and reported on additional studies such as photoemission into gas media, operation stability etc. In total we have produced 6 Na_2KSb PCs with peak QE of 15 to 25%, 7 Cs_3Sb PCs with peak QE of 10 to 40% and 28 K_2CsSb PCs. While the average QE-value of the latter was 28%, most of the latest produced, after mastering the technology, had larger QE values - at the higher range of commercial photomultipliers in the spectral range

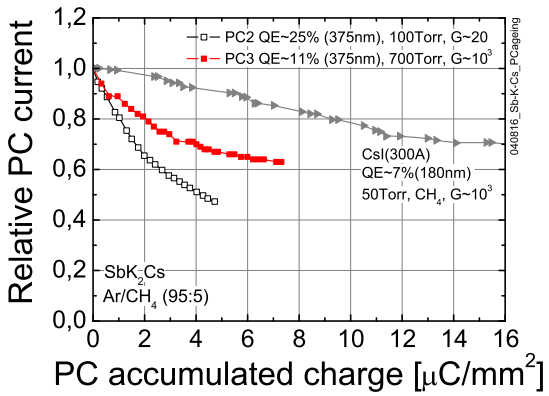

Figure 5.8: Ion-induced K_2CsSb photocathode decay in Ar/CH_2 (95:5) at different conditions; the ion induced ageing for a semitransparent CsI is also shown. Initial QE values and pressures are indicated.

of 313 - 546 nm. For instance, some of our K_2CsSb PC showed higher QE compared to that for the recently developed "Ultra Bi-Alkali" PCs by Hamamatsu Photonics. In one of our K_2CsSb PCs, a maximal QE of 58% at 365 nm was recorded; this peak QE value possibly constitutes a world record for bi-alkali PCs.

The stability of K_2CsSb and Cs_3Sb PCs was tested in somewhat unfavorable conditions (big volume chamber), yet, they showed stable QE over extended period of time: 28 days for Cs_3Sb PC and 83 days for K_2CsSb. By far better stability is expected in sealed devices.

The extraction efficiency ε_{extr} as a function of photon wavelength and electric field was investigated. Above a value of 500 V/cm the extraction efficiency ε_{extr} raised moderately, and therefore this value of the drift field E_{drift} was chosen in all GPM configurations further investigated. As in the case of CsI PCs [73], the electron emission from bi-alkali photocathodes into gas showed a significant dependence of the backscattering (and the resulting extraction efficiency ε_{extr}) on the wavelength, namely on the photoelectron energy. The extraction efficiency in Ar/CH_4 (95/5), at an electric field of 500 V/cm, rose linearly from ∼40% at 313 nm to ∼80% (relative to the vacuum value) at a wavelength of 546 nm. Due to backscattering the effective quantum efficiency QE_{eff} measured in gas was found

to be lower than the vacuum QE, as given by: $QE_{eff} = \varepsilon_{extr} \cdot QE$.

The ageing of semitransparent K_2CsSb PCs under avalanche-ion impact was investigated. In all experiments, one observed faster decay rate in K_2CsSb PCs compared to that in CsI PC. For K_2CsSb PCs, the decay rate in a 4-GEM GPM was two-fold slower than that in the parallel-plate GPM. In the 4-GEM GPM, the photocurrent (the QE) decayed to ∼80% of its initial value after an accumulated ion charge of ∼2 μC/mm^2, while in the case of parallel-plate GPM the ∼80% drop was observed after ∼ 1μC/mm^2 at the PC. This could be attributed to higher energy of the impinging ions in the parallel-plate GPM configuration.

5.2 Ion-Induced Secondary Electron Emission (IISEE) from alkali-antimonide PCs

As discussed in the section 3.5.3, the avalanche-induced ions drifting back to PC, impinge on the PC surface releasing secondary electrons. The latter initiate secondary avalanches, known as ion-feedback, limiting the gain by diverging into discharge.

The secondary electron emission into gas differs from that in vacuum as the electrons emitted from the PC are subject to back-scattering from gas molecules; the value of ion-induced secondary-electron emission (IISEE) coefficient in the gas media is lower than that in vacuum. The effect depends on the gas type, due to difference in the scattering cross-sections for various gases. The backscattering effect is smaller for a gas with a complex molecular structure; e.g. it is very strong in atomic gases while it is rather weak in organic compound gases. The same backscattering effect described in section 5.1.3 is responsible for affecting the quantum efficiency (photoelectron emission) in the gas to be smaller than that in vacuum. (It should be noted, however, that because photoelectrons and ion-induced secondary electrons do not have the same energy, the corresponding backscattering effect may differ in value).

In GPMs, it is essential to maintain the two contradicting conditions: to allow for

the highest possible quantum efficiency, while at the same time to reduce to minimum the ion feedback probability. For that purpose it is desirable to decrease the back-flow of avalanche ions to a level which, together with the given IISEE probability, will not cause gain divergence to discharge. The IISEE probability from bi-alkali PCs has not been reported yet. Its value is important for estimating the maximum attainable multiplication factors or, alternatively the IBF fraction required for stable operation of gaseous GPMs.

In this section we investigated the IISEE from Cs_3Sb , K_2CsSb and Na_2KSb PCs, both experimentally and theoretically. Measurements were carried out with PCs coupled to a double gaseous electron multiplier (double-GEM). The ion-induced secondary emission probabilities were deduced from the experimental gain-curves' shapes of the multiplier. The experimental data were validated by a theoretical model for ion-induced secondary electron emission from solids.

5.2.1 Experimental setup and methods

The GPM assembled for the IISEE studies comprised a double-GEM cascaded multiplier coupled to different visible-sensitive semitransparent PCs; the latter, bi- or mono-alkali ones, were vacuum deposited on a glass substrate as described in section 4.3.

The assembled multiplier was mounted in the detection chamber of our UHV system described in section 4.2. Following the introduction of the multiplier into the detector's chamber, the entire system was baked at 150^0C for 5 days in high vacuum. The PC was deposited and characterized under vacuum in the preparation chamber; next both the preparation and detector's chambers were filled, through a purifier, with Ar/CH_4 (95/5) gas mixture to a pressure of 700 Torr. The PC was then transferred in-situ and placed in the detector's chamber, 8 mm above the multiplier, to constitute a GPM.

The GPM was irradiated continuously with a UV-LED (NSHU590A, Nichia Corp., 375nm peak wavelength) focused onto the PC by means of a small lens through a quartz window. The detector and the electric scheme are shown in figure 5.9. Photoelectrons were transported into GEM1 holes under a drift field E_{drift}; following a gas-multiplication

process in the holes, avalanche electrons were transferred under a transfer field, E_{tans}, into the second multiplier GEM2, for further multiplication; charges induced by the two-stage multiplication were collected on an anode, interconnected with the "bottom" face of GEM2 to assure full charge collection. The multiplication (gain) curves of the GPM were deduced from the ratio of the anode current (I_A) to the photocurrent emitted, without multiplication, from the PC (I_{PC0}). The avalanche-induced IBF fraction is defined as a ratio of the anode current I_A to the avalanche ion-induced current at the PC I_{PC} (see figure 5.9).

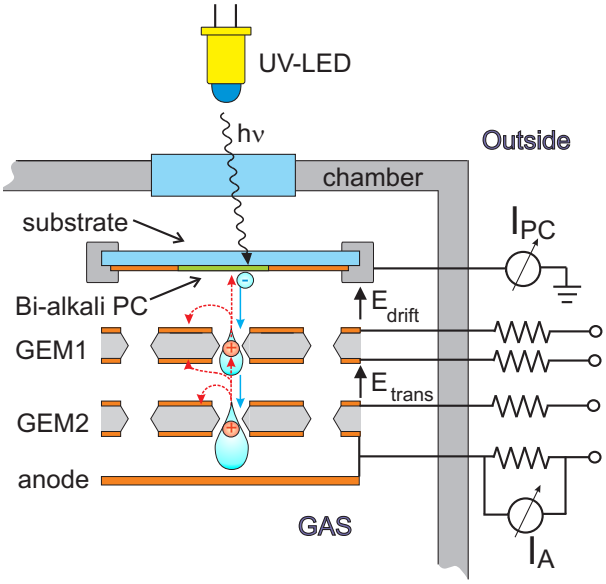

Figure 5.9: Schematic view of a double-GEM GPM with a semitransparent photocathode. Photoelectrons are extracted from the photocathode into the gas, they are focused into the holes of GEM1, multiplied and transferred into GEM2 holes for further multiplication. The avalanche ions (their possible paths are depicted by dotted arrows), in turn, drift back following the same electric field lines. The majority of ions are captured by the GEM electrodes and only a fraction reaches the PC. The GPM's gain and ion back-flow are established by recording currents at the anode (interconnected with the GEM2 bottom) and at the PC.

5.2.2 Theoretical evaluation of the ion-induced secondary emission effects

Estimation of the secondary emission coefficient

In ionized gas mixtures, an effective process of charge exchange takes place, substituting ions of high ionization potentials, as they drift towards the PC, by ions with lower ionization potentials. As mentioned in [46], it takes between 100 and 1000 collisions for an ion to transfer its charge to a molecule having a lower ionization potential. Since the mean-free-path λ for ion collisions with gas molecules is of the order of 10^{-5} cm at room temperature and atmospheric pressure [46], one can assume that after a drift length of $10^{-3} \cdot p^{-1}$ to $10^{-2} \cdot p^{-1}$ cm, (where p is the fraction of molecules with the lowest ionization potential in the mixture), the charge-exchange mechanism will leave only one species of ions drifting in the gas. In Ar/CH_4 (95/5) mixture used in this work, the distances for complete charge exchange are between 0.2 and 2 mm; they are therefore several times smaller then the 8 mm drift gap kept between the PC and the multiplier. The effective charge exchange in Ar/CH_4 was also confirmed experimentally in [10], through the similarity of ion-induced secondary emission coefficients measured from K_2CsSb PC into CH_4 and Ar/CH_4. Hereafter in the calculations we will consider only CH_4 ions.

In typical operating conditions of GPMs the electric field at the PC surface (E_{drift}) is 0.2-1 kV/cm [89]. Under these conditions, and due to collisions in the gas, the back-flowing ions have rather low kinetic energy (below 1 eV), which is too small for kinetic induction of secondary-electron emission [75, 90].

The most favorable ion-induced electron emission process is the Auger neutralization process, as discussed in [91]. The theory of Auger neutralization of noble gas ions at semiconductor surfaces was thoroughly described in [91, 92] Therefore, we shall focus here only on the main aspects of this phenomenon; all notations used below are those of [91].

In the vicinity of the PC surface, an ion induces polarization of the PC material, which can be formulated as an image charge. Due to the interaction of the ion with the image

Notation	Meaning
$E_i^{'}$	effective ionization energy at a distance s_m from the PC surface
$\varepsilon^{'}$, $\varepsilon^{''}$	initial energies in valence band of electrons participating in Auger neutralization
ε_v	valence band maximum energy
ε_c	conduction band minimum energy
ε_0	vacuum level energy
ε_k	energy of the excited Auger electron inside the PC
$E_k = \varepsilon_k - \varepsilon_0$	kinetic energy of the excited Auger electron outside the PC

Table 5.1: Notations used in the text and in figure 5.10

charge, the ionization potential of the ion shifts by

$$\Delta E_i = -\frac{(\kappa - 1) \cdot e^2}{(\kappa + 1) \cdot 4 \cdot s} \tag{5.1}$$

where κ is the dielectric constant of the PC material, s is the distance between the ion and PC surface, e is the electron charge.

The resulting effective ionization potential is given by $E_i^{'} = E_i - \Delta E_i$, where E_i is the free space ionization potential (e.g. 12.6 eV for methane). As an ion with effective ionization potential $E_i^{'}$ approaches the surface of the PC, the probability to get neutralized by an electron from the valence band of the PC increases up to a maximum at a distance s_m from the PC surface [91]. The distance s_m can be approximated as the average of the nearest-neighbor distance, a_{nn}, in the semiconductor (PC) and the molecular diameter of the gas (e.g. methane) molecule, d_{gas}:

$$s_m = \frac{a_{nn} + d_{gas}}{2} \tag{5.2}$$

The values of the parameters κ, a_{nn}, s_m for some PC materials used in our calculations are listed in Table 5.2; the molecular diameter of methane is assumed to be 3.8 $\mathring{A}$ [93]. The energy diagram of the electron transitions in the Auger Neutralization process is depicted in figure 5.10, with the notations listed in 5.1. The energies inside the solid are indicated

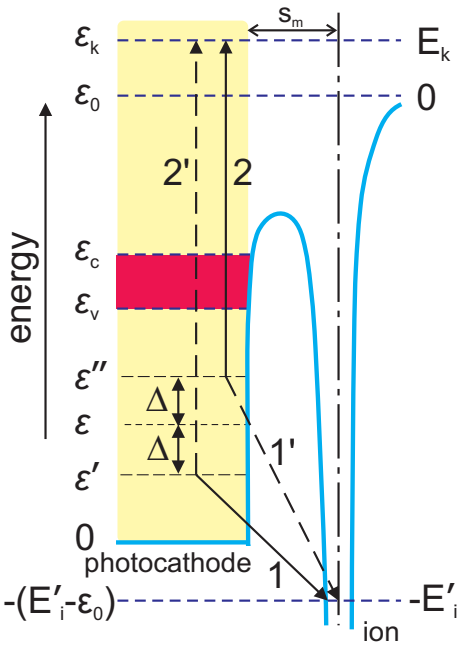

Figure 5.10: Energy-level diagram of the Auger neutralization process. Two sets of transitions are shown (1+2 and 1'+2'), to delineate the energy range in which the process is possible. The energies indicated on the left side of the drawing are inside the solid (e.g. bi-alkali PC) with zero at the bottom of the valence band; those on the right side of the drawing are outside the solid with zero level corresponding to vacuum level or to the energy of free electron at rest at an infinite distance from both ion and solid.

on the left side of the diagram; those outside the solid are shown on its right side. The valence band extends from zero to ε_v; the conduction band minimum is at ε_c; the bands are separated by a gap of $\varepsilon_c - \varepsilon_v$; the vacuum level is at ε_0. Two electrons in the valence band, with initial energies $\varepsilon^{'}$ and $\varepsilon^{''}$, are involved in the Auger transition: one electron will neutralize the ion and occupy the vacant ground level of the ion; the other electron will be excited by the released energy and will jump to an energy state ε_k in the conduction band. If it surmounts the surface barrier ε_0, it becomes an ion-induced secondary electron with an energy $E_k = \varepsilon_k - \varepsilon_0$.

figure 5.10 depicts two possible processes of this type, 1+2 and 1'+2'.

Energy conservation requires:

$$\varepsilon^{'} + \varepsilon^{''} = 2 \cdot \varepsilon = \varepsilon_k + \varepsilon_0 - E_k = E_k + 2 \cdot \varepsilon_0 - E_i^{'} \tag{5.3}$$

and by definition $\varepsilon_k = E_k + \varepsilon_0$. The maximal $(E_k)_{max}$ and minimal $(E_k)_{min}$ kinetic energy of the excited electron may now be evaluated from equation 5.3. The maximal kinetic energy is reached when $\varepsilon = \varepsilon_v$; it is given by:

$$\begin{aligned} (\varepsilon_k)_{max} &= E_i^{'} - \varepsilon_0 + 2 \cdot \varepsilon_v, \quad or \\ (E_k)_{max} &= E_i^{'} - 2 \cdot (\varepsilon_0 - \varepsilon_v) \end{aligned} \tag{5.4}$$

The minimum of the kinetic energy is reached when $\varepsilon = 0$; it is given by:

$$\begin{aligned} &(\varepsilon_k)_{min} = E_i^{'} - \varepsilon_0 \quad for \quad E_i^{'} - \varepsilon_0 > \varepsilon_c; \quad (\varepsilon_k)_{min} = \varepsilon_c \quad for \quad E_i^{'} - \varepsilon_0 \leq \varepsilon_c, \quad and \\ &(E_k)_{min} = E_i^{'} - 2 \cdot \varepsilon_0 \quad for \quad E_i^{'} - \varepsilon_0 > \varepsilon_c; \quad (E_k)_{min} = 0 \quad for \quad E_i^{'} - \varepsilon_0 \leq \varepsilon_c \end{aligned} \tag{5.5}$$

PC type	a_{nn} [$\mathring{A}$]	s_m [$\mathring{A}$]	κ	ε_v [eV]	$\varepsilon_c - \varepsilon_v$ [eV]	$\varepsilon_0 - \varepsilon_v$ [eV]
K_2CsSb	3.73[1]	3.76	9[2]	1.27[1]	1[3]	1.1[3]
Na_2KSb	3.35[4]	3.57	4.66[5]	2.34[4]	1[3]	1[3]
Cs_3Sb	3.95[6]	3.88	3.24[3]	1.31[7]	1.6[3]	0.45[3]

Table 5.2: Parameters used in theoretical calculations for K_2CsSb, Na_2KSb and Cs_3Sb photocathodes

[1]Ref. [94]
[2]Ref. [95]
[3]Ref. [17]
[4]Ref. [96]
[5]Ref. [97]
[6]Ref. [98]
[7]Ref. [99]

To calculate the secondary emission coefficient we used the electronic state density function $N_v(\varepsilon)$ in the valence band, which is assumed to be entirely filled. The valence-band state density functions $N_v(\varepsilon)$ for K_2CsSb, Na_2KSb and Cs_3Sb bi-alkali compounds, were calculated in [94, 96, 99] correspondingly and are schematically depicted in figure 5.11. The energy distribution function $N_i(\varepsilon_k)$ of Auger excited electrons inside the PC is proportional to the product of $N_c(\varepsilon)$, the state density function in empty conduction band, times an Auger transform $T(\varepsilon)$, which represents the probability to have two electrons in the valence band that can be involved in the process. The latter is thus the integral over the product of state densities $N_v(\varepsilon^{'}) \cdot N_v(\varepsilon^{''})$ in the regions $d\varepsilon^{'}$ and $d\varepsilon^{''}$ at all pairs of energies $\varepsilon^{'}$ and $\varepsilon^{''}$ which are both located at a distance Δ from ε in the valence band (figure 5.10). With a substitution: $\varepsilon^{'} = \varepsilon - \Delta$, $\varepsilon^{''} = \varepsilon + \Delta$ the Auger transform is then given by:

$$T(\varepsilon) = \int_0^\infty N_v(\varepsilon - \Delta) \cdot N_v(\varepsilon + \Delta) \cdot d\Delta \tag{5.6}$$

Though the integration limit goes to infinity, the integration actually stops when either $\varepsilon - \Delta$ or $\varepsilon + \Delta$ is out of the valence band's boundaries. The state density function $N_c(\varepsilon)$ in the conduction band is assumed to be proportional to the free electron state density function, $(\varepsilon_k - \varepsilon_c)^{1/2}$, for $\varepsilon_k > \varepsilon_c$; it is zero for $\varepsilon_k \leq \varepsilon_c$. Thus, the expression for the energy distribution of Auger excited electrons inside the PC may be written as:

$$N_i(\varepsilon_k) = K \cdot N_c(\varepsilon_k) \cdot T(\frac{\varepsilon_k + \varepsilon_0 - E_i^{'}}{2}), \tag{5.7}$$

where K is a proportionality constant and $\varepsilon = \frac{\varepsilon_k + \varepsilon_0 - E_i^{'}}{2}$ is taken from equation 5.3. K can be evaluated from the normalization of the distribution $N_i(\varepsilon_k)$ to an integral of one electron per Auger neutralized ion:

$$\int_{\varepsilon_c}^\infty N_i(\varepsilon_k) = 1 \tag{5.8}$$

The shape of $N_i(\varepsilon_k)$ for K_2CsSb, Na_2KSb and Cs_3Sb PCs is shown figure 5.11.

We proceed with a calculation of energy distribution $N_0(\varepsilon_k)$ of electrons which leave the PC surface. This calculation requires knowledge about the probability for an excited electron inside the PC to surmount the surface barrier and about the anisotropy of the electron angular distribution inside the PC. The escape probability as a function of kinetic energy is defined as follows [91]:

$$\begin{aligned} P_e(\varepsilon_k) = \frac{1}{2} \cdot \frac{1 - (\varepsilon_0/\varepsilon_k)^{1/2}}{1 - \alpha \cdot (\varepsilon_0/\varepsilon_k)^{1/2}}, \quad & \varepsilon_k > \varepsilon_0 \\ = 0, \quad & \varepsilon_k < \varepsilon_0 \end{aligned} \tag{5.9}$$

where ε_0 is the height of the surface barrier and the coefficient α reflects the anisotropy of the angular distribution for exited electrons. Hagstrum [91] has determined α to be 0.956 by fitting the theoretical model and experimental data for the case of helium ions neutralized at a Ge surface. The same anisotropy parameters were used by Hagstrum for Ne and Ar ions interacting with either Ge or Si surfaces, thus we use the same value in the following calculations. The escape probability $P_e(\varepsilon_k)$ is plotted in figure 5.11 for all PC types used in the calculations.

The energy distribution of electrons which escape the PC bulk $N_0(\varepsilon_k)$ is equal to the product of the energy distribution of Auger excited electrons inside the PC $N_i(\varepsilon_k)$ and the probability $P_e(\varepsilon_k)$ to surmount the surface barrier of hight ε_0:

$$N_0(\varepsilon_k) = N_i(\varepsilon_k) \cdot P_e(\varepsilon_k). \tag{5.10}$$

The shape of $N_0(\varepsilon_k)$ for K_2CsSb, Na_2KSb and Cs_3Sb PCs is shown in figure 5.11.

Finally, the secondary emission probability is expressed as an integral of $N_0(\varepsilon_k)$ over kinetic energies:

$$\gamma_+ = \int_{\varepsilon_0}^{\infty} N_0(\varepsilon_k) \cdot d\varepsilon_k = \int_0^{\infty} N_0(E_k) \cdot dE_k, \tag{5.11}$$

where $E_k = \varepsilon_k - \varepsilon_0$ is the kinetic energy of electrons as they leave the PC.

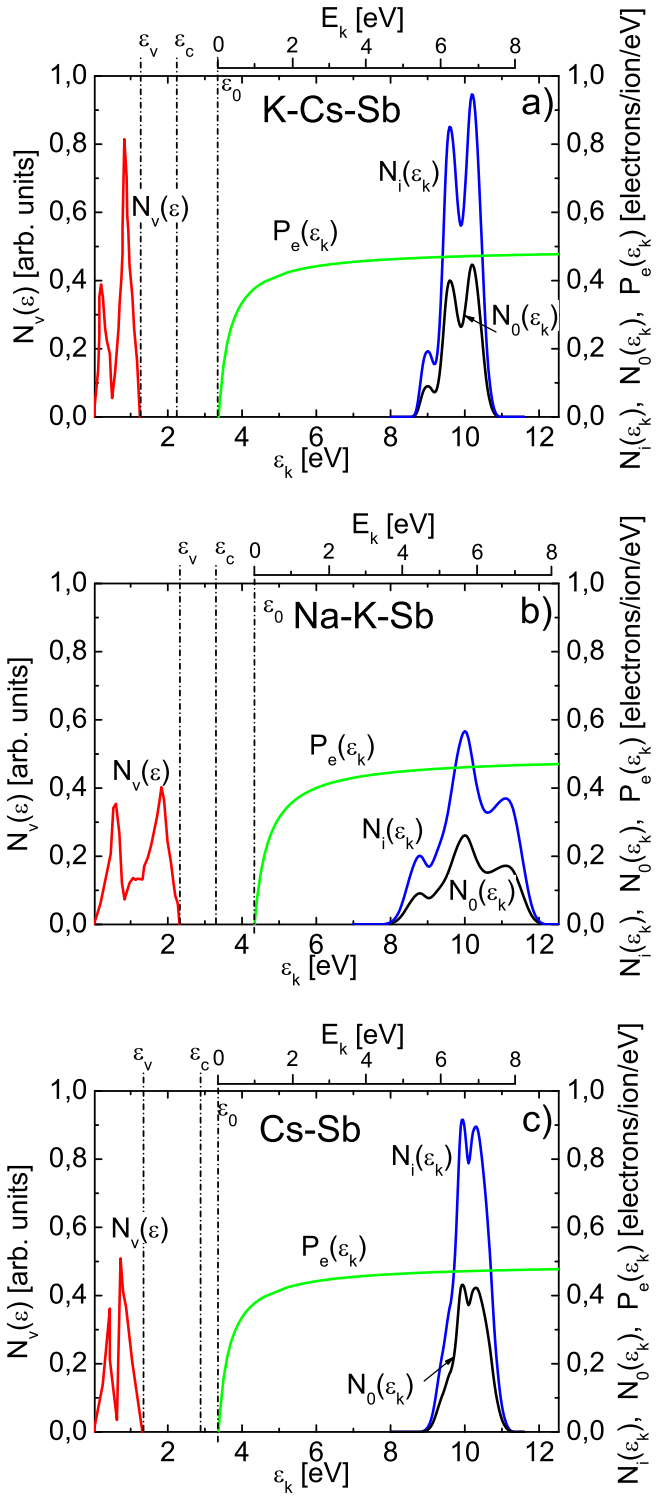

Figure 5.11: Plots of density of states $N_v(\varepsilon)$ in the valance band of the semiconductor, kinetic energy distributions $N_i(\varepsilon_k)$ for Auger electrons inside the semiconductor, probability to surmount the vacuum barrier $P_e(\varepsilon_k)$ for Auger electrons as a function of their energies and energy distribution of Auger electrons that escape from the semiconductor $N_0(\varepsilon_k)$. The upper scale indicates kinetic energies of Auger electrons outside the semiconductor $E_k = \varepsilon_k - \varepsilon_0$. The plots are shown for: a) K_2CsSb, b) SbK_2Na and c) Cs_3Sb semiconductor materials.

Thus, we are able to calculate $N_0(\varepsilon_k)$ and γ_+ as a function of the effective ionization potential of the incident ion, the electronic state density function $N_v(\varepsilon)$ in the valence band and the energy-band parameters ε_v, ε_c and ε_0 of the semiconductor (see table 5.2).

Clearly, the secondary emission coefficient calculated above is referred to vacuum environment. For PC operation in gas media, the measured secondary emission coefficient will be different, due to the scattering of the Auger electrons by gas molecules back to the PC [89, 10]. We denote the ion-induced secondary emission coefficient in a gas media as γ_+^{eff}; it is given by:

$$\gamma_+^{eff} = \gamma_+ \cdot \varepsilon_{extr} \tag{5.12}$$

where ε_{extr} is the fraction of secondary Auger electrons which were not backscattered. Thompson equation [100, 101] estimates the fraction ε_{extr} as

$$\varepsilon_{extr} = \frac{4 \cdot v_d}{\overline{v_{ae}} + 4 \cdot v_d} \tag{5.13}$$

where v_d is the electron drift velocity in the gas ($v_d = 2.34 \cdot 10^4$ m/s [102] in Ar/CH_4 (95/5) gas mixture for 273K and 700 Torr at an electric field of 0.5 kV/cm) and $\overline{v_{ae}}$ is the mean velocity of secondary Auger electrons emitted from the PC. This expression provides a fair estimate if the average kinetic energy of the emitted electrons is higher than the average equilibrium kinetic energy of electrons in the gas [100, 103]. In the case of Ar/CH_4 (95/5) at 700 Torr and drift field of 0.5 kV/cm, the average equilibrium kinetic energy for electrons is about 2 eV [104] which is smaller than the average kinetic energy of Auger electrons for the PCs investigated (figure 5.11); therefore equation 5.13 is valid and should provide a good estimate for ε_{extr}. The average velocity of the emitted Auger electrons was evaluated from the $N_0(\varepsilon_k)$ energy distributions: first the average kinetic energy $\overline{E_k}$ was calculated by the equation

$$\overline{E_k} = \int_0^\infty N_0(E_k) \cdot E_k \cdot dE_k / \int_0^\infty N_0(E_k) \cdot dE_k \ ;$$

the average velocity is then given by:

$$\overline{v_{ae}} = \sqrt{\frac{2 \cdot \overline{E_k}}{m_e}} \tag{5.14}$$

where m_e is the electron mass. The calculated average velocities for Auger electrons are: $1,51 \cdot 10^6$ m/s for K-Cs-Sb, $1,43 \cdot 10^6$ for Na-K-Sb and $1,54 \cdot 10^6$ m/s for Cs-Sb. The calculated values of ε_{extr} and γ_+^{eff} for K-Cs-Sb, Na-K-Sb and Cs-Sb PCs are listed in Table 5.3.

PC type	$E_i^{'}[eV]$	γ_+	ε_{extr}	γ_+^{eff}
K_2CsSb	11.83	0.47	0.058	0.027
Na_2KSb	11.95	0.49	0.061	0.03
Cs_3Sb	12.11	0.47	0.057	0.027

Table 5.3: Calculated $E_i^{'}$, γ_+, ε_{extr} and γ_+^{eff} values for K_2CsSb, Na_2KSb and Cs_3Sb photocathodes.

The calculated values ε_{extr} (Table 5.3) indicates that about 94% of Auger electrons are scattered back to the PC in Ar/CH_4 (95/5) at 700 mbar and 0.5kV/cm.

Equation 5.13 is not applicable for the photoelectron case as their average kinetic energies are approximately between 0.7 eV and 1.2 eV [105], a range which is lower than the average equilibrium kinetic energy (∼2 eV) of electrons in the gas at the conditions mentioned above. Data on the backscattering probability of photoelectrons in various gases may be found in [89, 73, 106].

Estimation of IISEE effects in visible-sensitive GPMs

The contribution of IISEE to the anode current recorded in a GPM can be estimated from the electron multiplication and the secondary electron emission. We assume that the PC is illuminated with a constant light flux. The average multiplication coefficient (gain) is denoted by G and the fraction of avalanche-induced ions flowing back to the PC is denoted by IBF; both are characteristics of the multiplier's structure and operation voltages. The

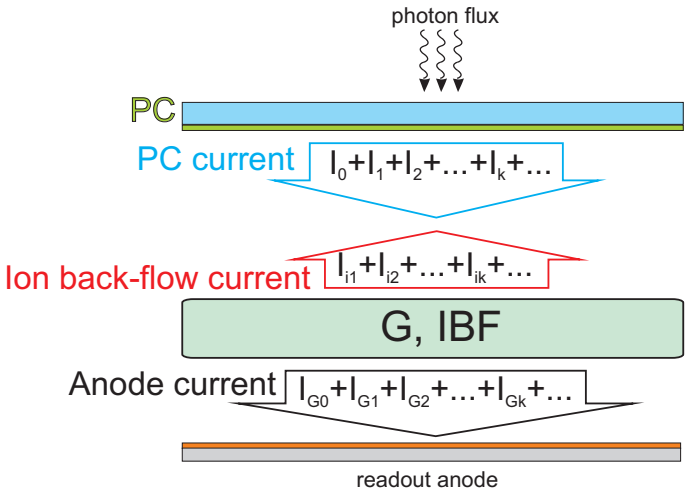

Figure 5.12: Operation of a visible sensitive GPM: a gaseous multiplier characterized by a multiplication factor G and a fraction of avalanche ions reaching the PC (IBF) is coupled to a visible sensitive PC. The PC is constantly illuminated by a light source inducing a primary photoelectron current I_0; as the photoelectrons are multiplied in the multiplier, a current I_{G0} is read at the readout anode while the primary current of avalanche ions I_{i1} is read at the PC.

light induces a photo-current I_0 at the PC, which, assuming full photoelectron collection to the multiplier (usually the case in GEM multipliers), yields after multiplication a current equal to $I_{G0} = I_0 \cdot G$ at the anode (see figure 5.12). The current of back-flowing ions reaching the PC, which are produced by these avalanches, is $I_{i1} = I_0 \cdot G \cdot IBF$. These ions impinging on the PC surface have a probability γ_+ to produce secondary Auger electrons; a fraction ε_{extr} of them will be emitted from the PC and initiate, after multiplication, a secondary-electron anode current $I_{G1} = I_0 \cdot G^2 \cdot IBF \cdot \gamma_+ \cdot \varepsilon_{extr}$. This, in turn, induces a second generation of back-drifting ions, further Auger-electrons production at the PC, etc.; the process results in a decreasing geometric series of currents ($I_{G1} = I_0 \cdot G^2 \cdot IBF^2 \cdot \gamma_+ \cdot \varepsilon_{extr}$, $I_{G3} = I_0 \cdot G^3 \cdot (IBF \cdot \gamma_+ \cdot \varepsilon_{extr})^2$, and so on (see figure 5.12). A condition: $IBF \cdot \gamma_+ \cdot \varepsilon_{extr} \cdot G < 1$ is required to avoid the series divergence. The k-th contribution of the IISEE can be formulated as $I_{Gk} = I_0 \cdot G^{k+1} \cdot (IBF \cdot \gamma_+ \cdot \varepsilon_{extr})^k$. The total anode current equals to the

sum of all contributions, given by:

$$I_A = I_{G0} + I_{G1} + I_{G2}... = \sum_{k=1}^{\infty} I_{Gk} = I_0 \cdot G \cdot \sum_{k=1}^{\infty} (G \cdot IBF \cdot \gamma_+ \cdot \varepsilon_{extr})^k \tag{5.15}$$

which may be also written as:

$$I_A = I_0 \cdot G \cdot \sum_{k=1}^{\infty} (G \cdot IBF \cdot \gamma_+ \cdot \varepsilon_{extr})^k = I_0 \cdot \frac{G}{1 - G \cdot IBF \cdot \gamma_+ \cdot \varepsilon_{extr}}, \tag{5.16}$$

or, in terms of gain,

$$G_{meas} = \frac{G}{1 - G \cdot IBF \cdot \gamma_+ \cdot \varepsilon_{extr}}, \tag{5.17}$$

where the measured gain, G_{meas} is the ratio of the measured anode current I_A to the primary photocurrent I_0 (figure 5.9 and figure 5.12), and I_0 is the multiplier's gain in the absence of ion feedback. To remind, IBF, the fraction of avalanche ions reaching the PC, is measured by the ratio of the PC current I_{PC} under avalanche multiplication to the anode current I_A (figure 5.9 and figure 5.12).

5.2.3 Experimental determination of the IISEE effects

The effective probability of IISEE defined above, γ_+^{eff}, can be extracted from the measured gain with IISEE, G_{meas}, if G (measured gain without IISEE) and IBF are known. Normally, G is an exponential curve, and the IISEE will be manifested as a deviation from this exponent (equation 5.17). As an example, figure 5.13 shows a gain curve obtained with a double-GEM coupled to a semi-transparent K_2CsSb PC, as function of ΔV_{GEM} (figure 5.9). Up to $\Delta V_{GEM} = 280$ V the gain increases exponentially and above 300V it diverges. At this point the quantity $G \cdot IBF \cdot \gamma_+ \cdot \varepsilon_{extr}$ in equation equation 5.17 approaches unity, leading to detector's break-down. For comparison, a second gain curve (dashed line) is plotted in figure 5.13, obtained with the same detector under the same operation conditions, but coupled to a semi-transparent CsI PC; the parameter G as a function of ΔV_{GEM} can be derived from this curve. As IISEE in CsI is negligible, due to a very wide band-gap of about

6 eV, the gain curve grows exponentially even at the highest operation potentials. The IBF as a function of GEM voltage was measured in the same detector (geometry, gas and voltages), with a CsI PC, and was plotted in figure 5.14 as function of ΔV_{GEM}. The data points in figure 5.14 were fitted with an exponential function, which seems to appropriately describe the dependence of IBF on the GEM voltage. With the known dependence of IBF and G (properties of the multiplier that are independent of the PC) on the GEM voltage ΔV_{GEM}, the parameter could be derived (using equation 5.17) from the gain-voltage curve of the same multiplier coupled to a visible-sensitive PC. This procedure, however, had a large uncertainty; namely, an inaccuracy in adjustment of the total gain, which was very sensitive to small voltage deviations, resulted in ∼30% error in γ_+^{eff}.

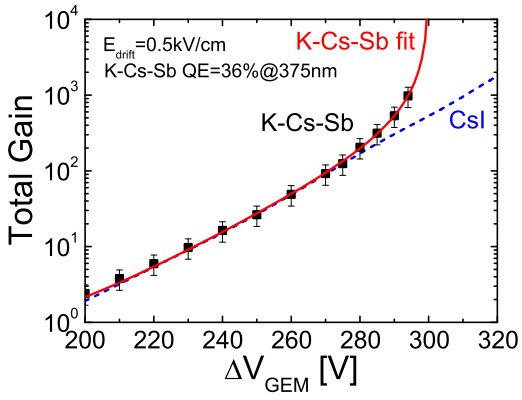

Figure 5.13: Gain-voltage characteristics measured in the GPM of figure 5.9 (see conditions in the figure, QE refers to vacuum) with CsI (dashed line) and K_2CsSb (open circles) photocathodes. The divergence from exponential with K_2CsSb is due to ion-induced secondary electron emission. The solid line is a fit to the experimental data points using equation 5.17.

The gain-voltage curves were measured for several samples of various visible-sensitive PCs: eight K_2CsSb samples, six Na_2KSb samples and three Cs_3Sb PCs. As the emission properties of a given PC type varied from sample to sample, we could establish a significant data base of γ_+^{eff} - values as function of the QE. The correlation is shown in figure 5.15. As one can see, γ_+^{eff} increases with QE, reaching a value of about 0.03 electrons/ion for

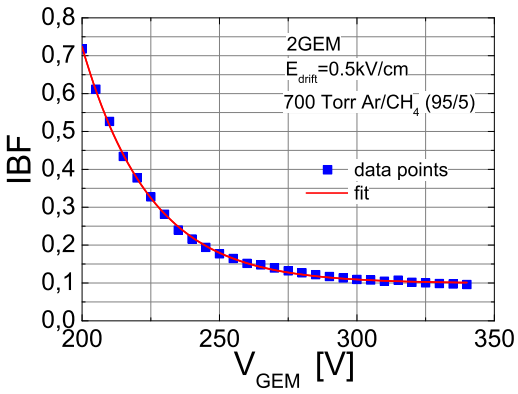

Figure 5.14: Ion back-flow fraction (IBF) as a function of GEM voltage for the double-GEM multiplier shown in figure 5.9, measured in 700 Torr of Ar/CH_4 (95/5). The solid line is a fit to the data points.

the most efficient PCs; its value is independent of the PC type.

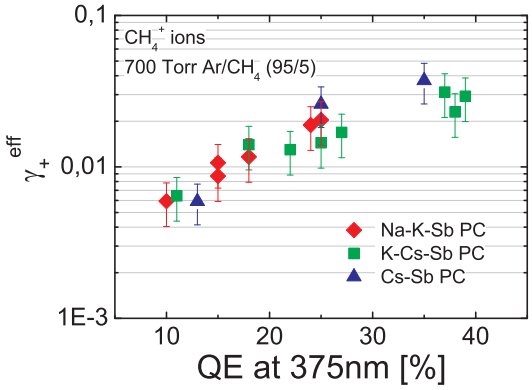

Figure 5.15: Measured effective probability of the ion-induced secondary electron emission coefficient for K_2CsSb, Na_2KSb and Cs_3Sb PCs as a function of their quantum efficiency values (QEs).

5.2.4 Discussion on IISEE from alkali-antimonide photocathodes

Experimental and theoretical approaches were undertaken to estimate the probability of ion-induced secondary electron emission in a gas medium; the research work is within our ongoing efforts to develop gas-avalanche photomultipliers sensitive to single photons in the visible spectral range.

A simple theoretical model was adopted for calculating the ion-induced secondary emission coefficient γ_+^{eff} from bi- and mono-alkali photocathodes. We assumed the Auger neutralization process as the main mechanism for the secondary electron emission and used basic properties of semiconductors to evaluate the emission probability. The input parameters for the calculation were the effective ionization potential $E_i^{'}$ of the incident ion, the density of states in the valence band and the energy-band parameters ε_v, ε_c and ε_0 of the semiconductor (the PC). γ_+ was calculated to be 0.47, 0.49 and 0.47 for K-Cs-Sb, Na-K-Sb and Cs-Sb PCs, correspondingly. The calculated values of γ_+ are quite similar for the three PCs, which can be explained by the similarity of their energy-band parameters. The bi- and mono-alkali PC materials used here have a very narrow valence band (1-2 eV) as compared to the effective ionization energy of methane ions ($\sim$12 eV). This leads to narrow (2-4 eV) energy distributions of the Auger electrons (figure 5.11), peaking at a rather high energy of about 6 eV (top scale of figure 5.11) the energies of Auger electrons are in a range from 4 eV to 8 eV.

The effective secondary emission coefficient γ_+^{eff}, namely the one corrected for the backscattering, in Ar/CH_4 (95/5) at 700 mbar and field 0.5 kV/cm was calculated from the theoretical model to be 0.027 for Cs-Sb and K-Cs-Sb PCs and 0.03 for Na-K-Sb PC.

A simple method for experimental extraction of γ_+^{eff} from measured voltage-gain curves was introduced. It is based on recording and comparing avalanche currents on the PC and anode of a double-GEM multiplier coupled to CsI and visible-sensitive PCs, under the same operation conditions. CsI, with no ion feedback, provided the multiplication factor and the ion back-flow fraction, while the visible-sensitive PCs provided the effective secondary emission coefficient into gas, γ_+^{eff}, derived from a fit of the gain-voltage curve through equa-

tion 5.17. γ_+^{eff} in Ar/CH_4 (95/5) at 700 Torr were between 0.02 and 0.03 Auger electrons per incident ion for Na-K-Sb, K-Cs-Sb and Cs-Sb photocathodes; it is in good agreement with our theoretical estimations, despite the fact that the experimental PC surfaces were most probably not perfect ones from the point of view of stoichiometry [9], defects and traps. For all three PCs investigated, γ_+^{eff} increased with the PC's QE, regardless of the PC type. It is therefore reasonable to believe that the theoretical calculations yielded a reasonable estimate of γ_+^{eff} only for the highest QE-values.

Further reduction of the IISEE coefficient, γ_+, for these bi- and mono-alkali photocathodes, could only be envisaged by using other gases, with lower effective ionization energy than Ar/CH_4 (95/5). As an illustration, the dependence of γ_+ for K-Cs-Sb on the effective ionization energy of the ion was calculated using the above model, and is presented in figure 5.16. A two-fold reduction of γ_+, as compared to the value of 0.47 calculated for methane ions, would require a gas with effective ionization energy of about 6 eV. Some low ionization potential photosensitive vapors like triethylamine (TEA, ionization potential 7.5 eV) [107, 108], tetrakis(dimethylamine)ethylene (TMAE, ionization potential 5.36 eV) [109] and ethyl ferrocene (EF, ionization potential 6.1 eV) [110] employed in some gaseous detectors could be admixed to the GPM's gas filling in order to decrease the IISEE probability. For example, EF yielded stable operation of a detector with CsI photocathode [111]. It was shown [112] that in the GPM filled with He/CH_4 comprised of Cs-Sb PC and a capillary plate, an addition of EF vapor to the gas mixture slightly improved the PC's QE and the maximal achievable gain of the device. Other gases with low ionization potentials ($\sim$10 eV) employed in detectors are long-chain hydrocarbons, e.g. iso-butane. The ions of such gases have a high probability for dissociation, creating free radicals; they are known to induce aging in gas avalanche detectors. The photocathodes may suffer from enhanced chemical aging when operated in such an environment.

A further reduction of the effective secondary emission coefficient $\gamma_+^{eff} = \gamma_+ \cdot \varepsilon_{extr}$, (the fraction of Auger electrons that surmounted the backscattering with gas molecules) may be obtained by increasing the Auger electrons' backscattering, while keeping it low for photoelectrons. Due to the significant difference in the energy spectrum of Auger- and

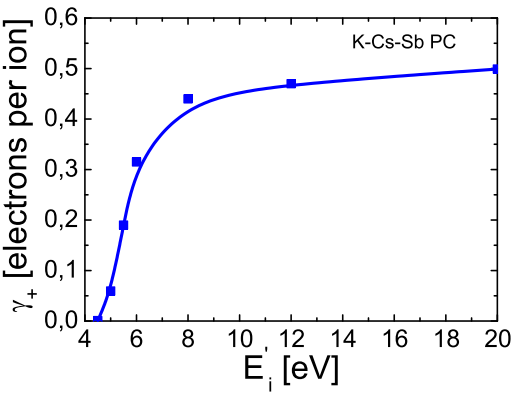

Figure 5.16: Calculated dependence of the secondary emission coefficient in K_2CsSb on the effective ionization energy.

photo-electrons, it might be possible to choose a gas that complies to this requirement, as indicated in figure 5.17.

In the corresponding kinetic energy range between 4 eV and 8 eV, the fraction of Auger electrons which scattered back to the PC following collisions with gas molecules was estimated with the model to be rather high, about ∼94% in Ar/CH_4 (95/5) at 700 Torr, under a drift field of 0.5kV/cm; for comparison, the photoelectrons (induced by UV-to-visible light photons in the range between 2.2 eV and 4 eV) backscattering in the same conditions was measured to be in a range between 60% and 20% for K-Cs-Sb PC (see figure 5.7 in section 5.1.3). The large difference in backscattering for Auger electrons and photoelectrons is apparently due to the difference in their initial kinetic energies. The kinetic energy distributions for photoelectrons originated from K-Cs-Sb by visible-range photons (2.1 eV to 3.1 eV) are peaked between 0.7 eV and 1.2 eV, extending from 0.2 to 1.7 eV [105]; the distributions for Na-K-Sb and Cs-Sb are assumed to be essentially similar. The Auger electrons induced by ions are more energetic according to our calculations and their energies extend between 4 and 8 eV (see figure 5.11). On the other hand, the electron scattering cross-sections for argon and methane are functions of the electron's kinetic energy; they are depicted in figure 5.17(a) and figure 5.17(b). For noble gases, higher

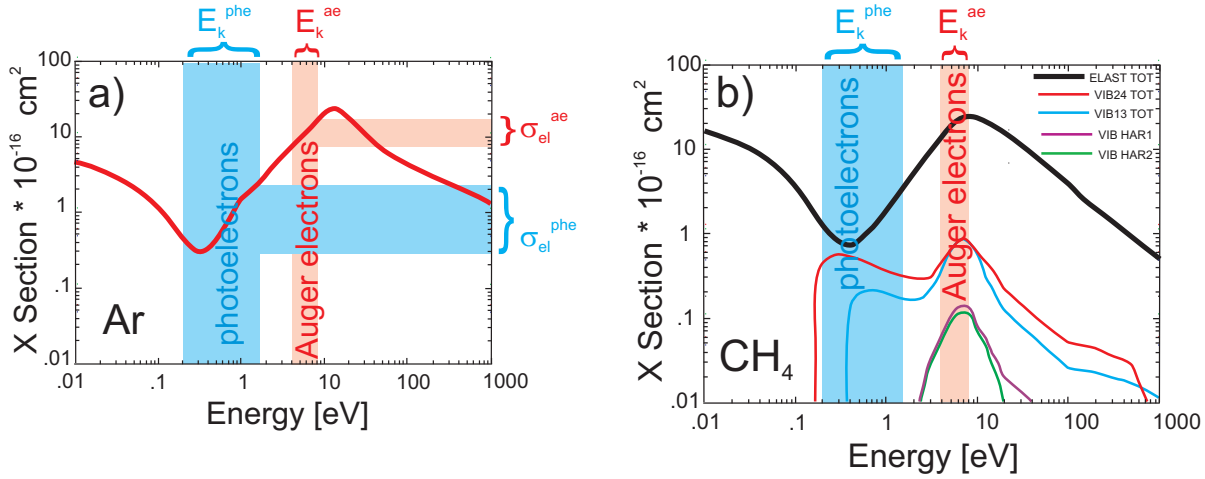

Figure 5.17: a) Elastic scattering cross-sections for argon. The photoelectron's energies are in the Ramsauer minimum of the elastic cross-section curves, while the Auger electrons energies correspond to rather high cross-sections. b) Elastic and inelastic cross-sections for methane. The photoelectron E_k^{phe} and Auger electron E_k^{ae} energy spreads are shown. The ratio of elastic/inelastic cross-sections is much smaller for photoelectrons than that for Auger electrons. The plots were taken from an open cross-section database at [113].

backscattering is related to higher elastic scattering cross-section (and to smaller energy loss in elastic collisions, when going from light to heavy gas); for more complex molecules, the backscattering behaves as the ratio of elastic-to-inelastic scattering, vibrational excitation collisions playing an important role in cooling down the energy of the photoelectrons in the gas [74, 114, 73].

In the energy range between 4 and 8 eV (Auger electrons) either the elastic scattering cross-sections (argon) or the ratios of elastic-to-inelastic scattering cross-sections (methane) are rather large and so is the backscattering; photoelectrons of energies ranging between 0.2 and 1.7 eV fall into the region of Ramsauer minimum of elastic cross-sections for argon; in methane there is also a Ramsauer minimum at about the same energy as in argon, in the vicinity of which the ratio of elastic/inelastic cross-sections is small; the corresponding back-scattering is several times smaller than that for Auger electrons.

Choosing a GPM's operating gas in which backscattering is high for Auger electrons and low for photoelectrons will result in good photoelectron extraction (high effective QE) and reduced probability of ion-induced secondary effects. This point to a choice of gases with pronounced Ramsauer minimum located close to the energy range of photoelectrons induced by visible light photons. Examples are heavy noble gases, namely Xe, Kr, Ar and methane. A gas mixture of Ar and CH_4 exhibiting this property, was used in the present work.

5.3 Requirements on IBF in gaseous multipliers

Based on our γ_+^{eff} - values estimated in the previous section, we can analyze the requirements from any type of gaseous multiplier used in combination with a visible-sensitive PC (in the present gas); other gases would require the calculation of the electron backscattering coefficients. In particular, the ion back-flow fraction, IBF, and gain permitting stable continuous-mode operation of visible-sensitive gaseous photomultipliers can be estimated, through equation 5.17. To avoid avalanche divergence into a spark it should fulfill the condition: $G \cdot IBF \cdot \gamma_+ \cdot \varepsilon_{extr} < 1$. Thus, a gain of 10^5 (e.g. required for high single-photon sensitivity) and γ_+^{eff}=0.03 implies $IBF < 3,3 \cdot 10^{-4}$. However, as explained in section 3.6, the lowest IBF-values reached so far were by two orders of magnitude above this requirement. In the following sections we will present multiplier configurations in which this requirement is fulfilled.

5.4 IBF reduction in micro-hole gaseous multipliers

This section describes new solutions for efficient ion blocking in cascaded micro-hole multipliers comprising GEMs and other patterned electrodes.

5.4.1 The R-MHSP and F-R-MHSP concepts

Following by a success in IBF reduction by incorporating in a cascade the MHSP elements (see figure 3.12 section 3.6), it was further proposed [115] to reverse the roles of the MHSP's anode and cathode strips, in an attempt to trap ions originating from consecutive multiplication elements in the cascade, preventing them to flow through the holes. figure 5.18(a) and figure 5.18(b) show the field configuration in the immediate proximity of the MHSP hole, for these two different modes of MHSP operation, defined here as the *normal* (MHSP) and the *reversed* (R-MHSP) modes (the small arrows point at the field direction, namely to the ion drift direction). Note that in the normal MHSP mode, the narrow strip-electrodes act as anodes; they are biased more positive than the broader (cathode) strips surrounding the holes; in this case double-stage multiplication takes place within the holes and at the anode strips (figure 5.18(a)). In the reversed R-MHSP mode, the narrow strips are biased more negative than the broader ones; charge multiplication occurs only within the holes while the more-negative narrow cathode-strips only collect a fraction of the ions (figure 5.18(b)). The operation mode of the MHSP permits its use either as a stand-alone detector [72, 116] or as the last element in a cascaded multiplier [12]. On the other hand, the R-MHSP, with its hole-multiplication, can be used anywhere in the cascade, and especially as a first element, trapping back-flowing ions from all successive elements (as shown below).

In the present thesis work, the new concept was suggested of "Flipped" Reversed-bias Micro-Hole & Strip Plate (F-R-MHSP) electrodes in which strips are pointing up towards the drift region of the multiplier. The negatively charged strips trap ions originated from successive multiplying elements. However, like in a GEM, avalanche-ions created within the R-MHSP holes remain uncollected and reach the drift volume (or the PC). The idea of flipping the R-MHSP with its patterned strips pointing towards the drift volume (or the PC), aims at collecting all back-drifting ions, including those originating from its own hole-avalanches. The flipped R-MHSP (F-R-MHSP) is shown schematically in figure 5.18(c). Like in the R-MHSP mode, the narrow ion-collection strips are biased more negative than

the broader ones; the multiplication occurs only within the holes. The F-R-MHSP can be inserted anywhere along the cascaded multiplier, but its best performance is expected when used as the first multiplying element in the cascade.

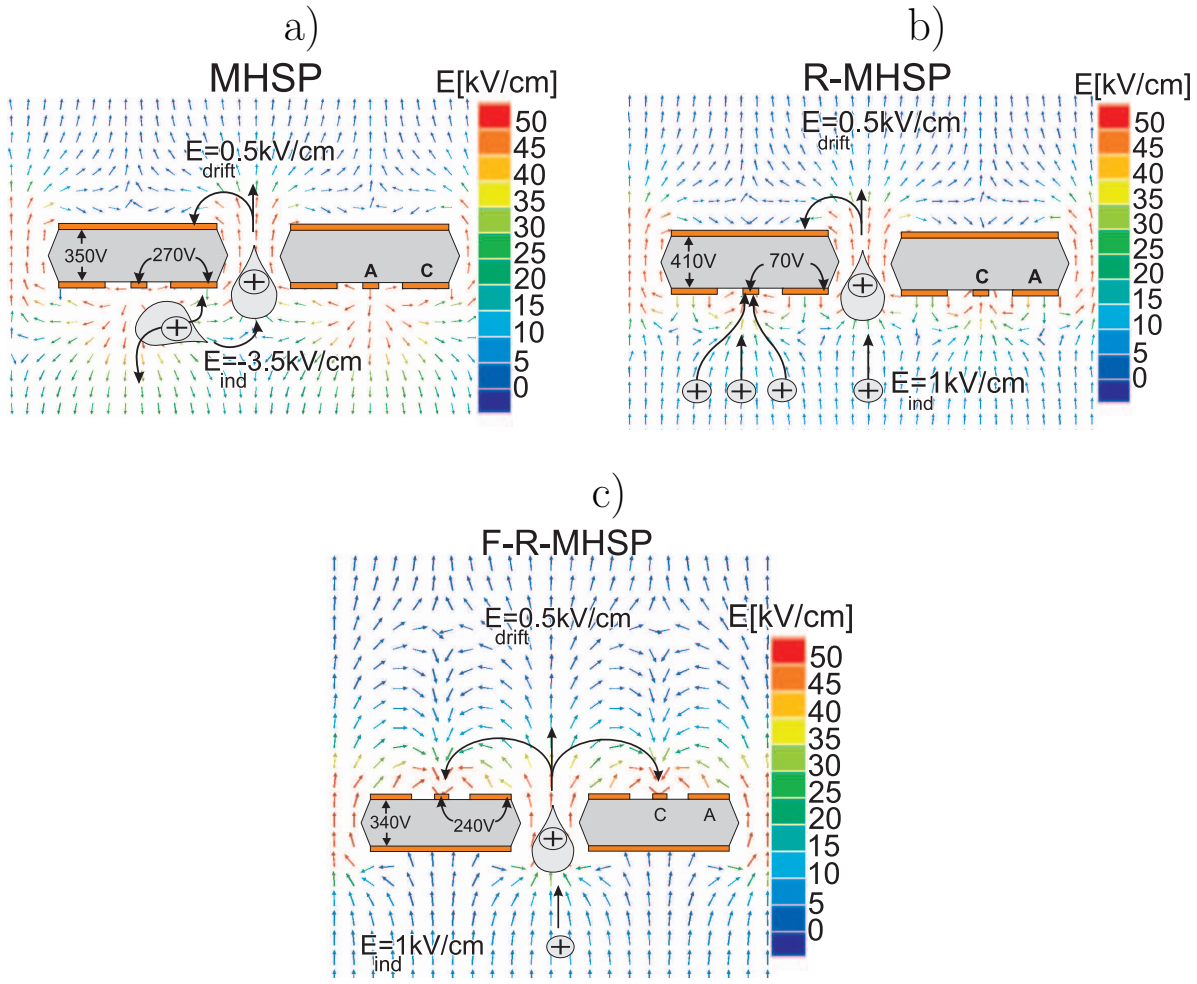

Figure 5.18: *The electric-field vectorial maps calculated by MAXWELL software package in the vicinity of the electrodes and schematic views of the operation principles for: a) normal MHSP b) reversed-biased R-MHSP and c) flipped reversed biased F-R-MHSP. The potentials selected for the field-map calculations and the color code of the fields are shown in the figures.*

5.4.2 The "Cobra" concept

A new patterned micro-hole electrode named Cobra (figure 5.19) was developed with a geometry that is expected to improve the ion divergence away from the holes. It has thin anode electrodes surrounding the holes and creating strong electric field inside the holes (required for charge amplification); the more negatively biased cathode electrodes cover a large fraction of the area for better ion-collection as compared to the F-R-MHSP described above. The Cobra electrode was designed as a first element in the cascade with the patterned area pointing towards the photocathode.

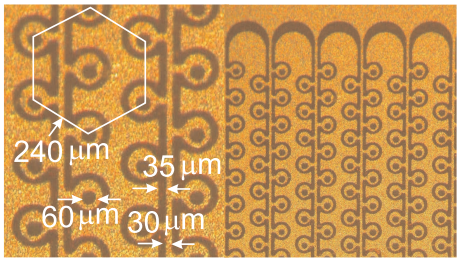

Figure 5.19: Microscope photograph (two magnifications) of one face of a "Cobra" micro-hole electrode with dimensions given in the figure. The other face is identical to a GEM (e. g. figure 3.9).

5.4.3 Single-electron detection efficiency of micro-hole multipliers

Two conditions have to be fulfilled for reaching full detection efficiency of single photoelectrons emitted from a photocathode, or of ionization electrons radiation-induced within the drift volume:

- The electron's collection efficiency into holes, particularly in the application to single-photon GPMs, has to be close to unity; as confirmed for GEMs [69];
- The visible gain (defined as the number of electrons, per single initial electron, transferred from a given multiplier element into a consecutive electrode [117]), of the first

element in the cascade should be large enough to ensure full efficiency of the event's detection by the following elements in the cascade.

These two conditions are of prime importance, because an electron lost at the first multiplication element due to inefficient focusing, insufficient multiplication or inefficient extraction and transfer into the next multiplication stage, cannot be recovered. In the R-MHSP, the biasing scheme could cause a reduction of the extraction efficiency of the avalanche electrons from the holes towards the next element in the cascade, thus reducing the visible gain of this multiplier. In the F-R-MHSP and the Cobra the patterned side is facing the PC and could affect photoelectron focusing into the holes; therefore, the focusing efficiency has to be carefully determined.

The photon detection efficiency in GPMs, ε_{photon}, depends on both: the PC's quantum efficiency (QE) and on the single-photoelectron detection efficiency ε_{det}; it is defined as:

$$\varepsilon_{photon} = \mathrm{QE} \cdot \varepsilon_{det}. \tag{5.18}$$

ε_{det} depends on many parameters: the detector geometry, the gas mixture, the electric field conditions, the multiplier gain, the electronics system etc. Once emitted from the photocathode surface into the gas, the photoelectron has to be focused into the first amplifying stage of the detector, namely into the holes. The mechanism of electron extraction, transfer and multiplication in cascaded GEMs for hole-voltage values exceeding 320V across holes were extensively studied in [69].

While the operation properties of the MHSP were well established [12], those of R-MHSP, F-R-MHSP, Cobra and GEM required some more basic studies. The studies of single-electron detection efficiency for the R-MHSP, the F-R-MHSP and the Cobra were designed to yield better understanding of the role of the various potentials and of the conditions for reaching minimal IBF values while keeping minimal electron losses.

The parameters affecting the R-MHSP, F-R-MHSP and Cobra operation are:

1. the hole voltage (V_{hole}); it controls the multiplication and the IBF values of the first multiplying element;

2. the anode-to-cathode strip voltage (ΔV_{AC}); it reduces the visible gain of a single R-MHSP; it could affect the focusing properties of the F-R-MHSP and the Cobra and reduce the IBF from successive elements and from its own avalanches;

3. the transfer field below the R-MHSP the F-R-MHSP or the Cobra (E_{trans} in figure 5.18(a) and figure 5.18(b)); it could, in principle, affect both the IBF from successive elements and the visible gain of the R-MHSP, the F-R-MHSP or the Cobra;

It should be noted that except the second condition, similar remarks also apply to a GEM.

In a GPM, the possible fate of the photoelectron after its emission from the photocathode is schematically shown in figure 5.20.

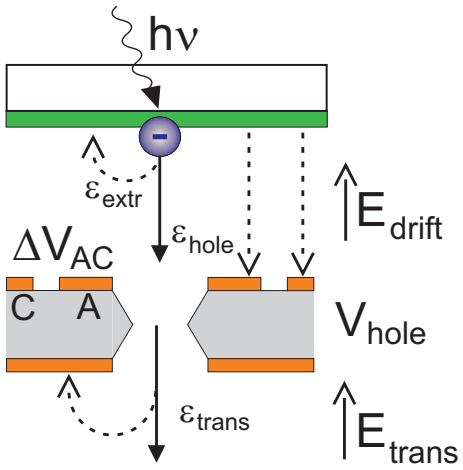

Figure 5.20: Electron transfer through a F-R-MHSP. Photoelectrons emitted from a PC are extracted with an efficiency ε_{extr}, guided into the apertures of the F-R-MHSP with an efficiency ε_{hole}. A fraction of the avalanche electrons is extracted from the hole and transferred into a following element with an efficiency ε_{trans}; another fraction is lost to the bottom electrode. The electron transfer through any other hole multiplier can be described the same way.

The single-photoelectron detection efficiency can thus be described as:

$$\varepsilon_{det} = \varepsilon_{extr} \cdot \varepsilon_{hole} \cdot \varepsilon_{trans} \tag{5.19}$$

Here ε_{det} is the probability to detect a single photoelectron, ε_{extr} is the probability to extract a photoelectron from the PC, ε_{hole} is the probability to get this electron into the hole and ε_{trans} is the probability to transfer an avalanche electron to the next multiplication stage.

As mentioned above, all the measurements were performed in $Ar/CH_4(95/5)$ under atmospheric pressure. In all the measurements presented below we assumed $\varepsilon_{extr} = 1$ in equation (5.19). Realistic ε_{extr} values are well known, and were previously measured for CsI PCs as function of the drift field above a photocathode for a variety of gas mixtures [66] and for bi-alkali PCs as a function of the drift field and photon wavelength (see section 5.1.3). Thus the measured electron detection efficiency in GPM conditions (high drift fields) can be straightforwardly corrected, using the known ε_{extr} at the corresponding drift field and gas mixture. For instance, in atmospheric Ar/CH_4 (95/5) used in all our measurements, ε_{extr}=70% for CsI PC at drift fields of 0.5 kV/cm.

Due to the statistical fluctuations in the amplification process of single electrons (see section 3.4), many events have only a small number of electrons at the exit of the holes of the first amplifying element. Continuous mode measurements (e.g. ratio of the current after multiplication to that of primary photoelectrons) are not sensitive to single-photoelectron losses or to events with small gain; the contribution of these to the total current is negligible when the detector is operated in multiplication mode. Current-mode measurements provide valid results for single-photoelectron transport, only if the detector is operated at unity gain. Under these conditions, the only way to assess the single-electron detection efficiency ε_{det}, is by event pulse-counting. A more detailed discussion on this subject can be found in [10].

We found it convenient to measure ε_{det} of the hole multipliers by comparing their event-rate to the one measured with a multi-wire proportional counter (MWPC). This strategy has been used in many of our previous studies, and was discussed in detail [69, 78, 118]. figure 5.21a shows the dedicated experimental setup. It consists of a UV-transparent quartz (Suprasil) window with CsI semitransparent PCs evaporated on both surfaces, sandwiched between the reference MWPC detector and the investigated multiplier (R-

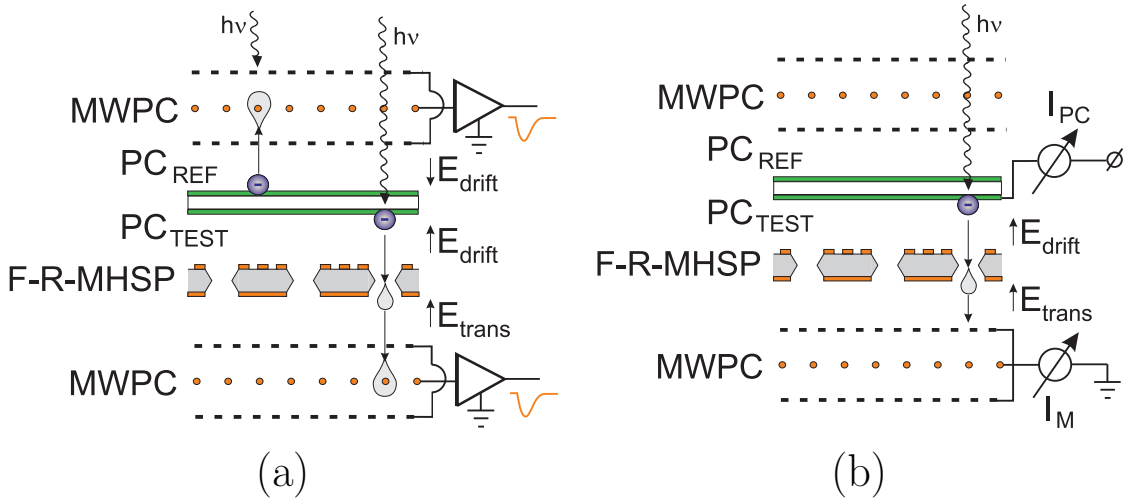

Figure 5.21: The schematic view of the experimental setup for measuring the single-electron detection efficiency of a F-R-MHSP (a) and its visible gain (b). Similar setups were used for measuring the same properties of a R-MHSP, a Cobra and a GEM

MHSP/MWPC, F-R-MHSP/MWPC, Cobra/MWPC or GEM/MWPC). Both, reference and investigated detectors operated at equal total gains; the MWPC following each investigated hole-multiplier was added to keep the total gain high enough for pulse counting. The exponential single-photoelectron spectra were recorded for the reference MWPC detector and for the investigated hole-multiplier (R-MHSP/MWPC, F-R-MHSP/MWPC, Cobra/MWPC or GEM/MWPC) at equal total gains and therefore, equal pulse-height distribution slopes (figure 5.22). The slopes were adjusted by voltage variation of the MWPC in each investigated multiplier. The number of detected events in each configuration was evaluated by the integration of the middle part of each pulse-height spectrum (see figure 5.22) in order to minimize possible errors due to electronic noise contribution (lower end of the spectrum) or to feedback effects (higher end). The ratio of the number of detected events, with equal electronic thresholds, multiplied by the ratio of initial photocurrents of the top-face and bottom-face PCs, provided the absolute single-electron detection efficiency of the the R-MHSP, the F-R-MHSP, the Cobra or GEM multipliers. This method can be naturally applied only in proportional-mode operation; it is no longer applicable in

conditions of charge saturation or with feedback effects - leading to spectra that deviate significantly from the exponential. A more detailed explanation on this method can be found elsewhere [78, 118].

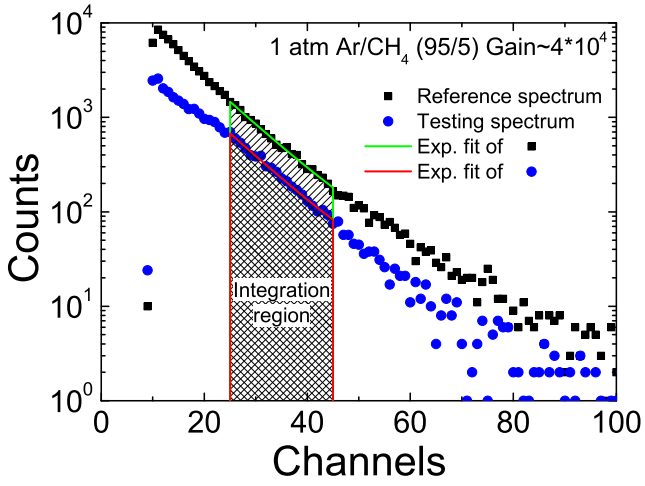

Figure 5.22: An example of two single-photoelectron spectra measured for the reference multiplier (MWPC) and for the investigated multiplier (R-MHSP/MWPC). The region in which the spectra were integrated is indicated.

Measurements with R-MHSP

The photoelectron detection efficiency of the R-MHSP as function of the inter-strip voltage (potential difference between the anode and cathode strips) ΔV_{AC} is presented in figure 5.23 at E_{drift}=0.5kV/cm. The measurements were performed at V_{hole} values of 360V, 380V and 400V. In all cases, the transfer field was set to 1 kV/cm. The visible gains as a function of the inter-strip voltage are also presented for each set of measurements. The visible gain G_{VIS} is derived from the ratio of the current I_M measured at the interconnected electrodes of bottom MWPC (see figure 5.21b), to the PC photocurrent I_{PC0}, measured in

photoelectron collection mode (no gain):

$$G_{VIS} = \frac{I_M}{I_{PC0}}. \tag{5.20}$$

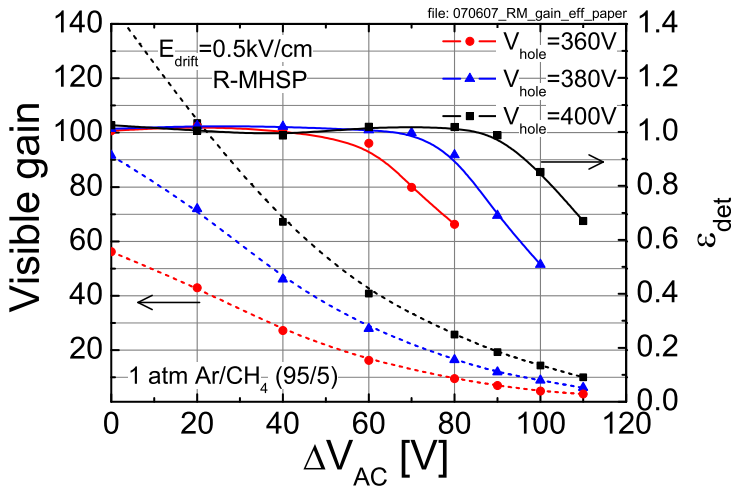

Figure 5.23: The visible gain (left y-axis, dashed lines) and the photoelectron detection efficiency (right y-axis, solid lines) as a function of the inter-strip voltage ΔV_{AC} of a R-MHSP. Measurements performed at different values of hole voltage at E_{drift}=0.5 kV/cm.

Although it is desirable to increase ΔV_{AC}, as to divert more ions towards the cathode strips, the drop in the visible gain (figure 5.23), and consequently in the detection efficiency, sets a limit to this parameter. ΔV_{AC} can be raised if the loss of electrons is compensated by a further increase of V_{hole}. For each hole-voltage, the maximal strip voltage could be found at which the photoelectron detection efficiency is close to unity. The maximal strip voltages at which the detection efficiency is ∼100% are 60V, 70V and 90V at corresponding hole voltages of 360V, 380V and 400V. These inter-strip voltages correspond to a visible gain of about 20 on the R-MHSP as can be seen in figure 5.23.

Measurements with F-R-MHSP

Measurements similar to that of the R-MHSP were performed for the F-R-MHSP. As mentioned above, in the F-R-MHSP configuration, the strips are facing towards the drift region or to the PC. Therefore, the electron transfer to the next amplification stage is expected to be unaffected by varying the strip voltage. However, the increase of the inter-strip voltage difference could, in principle, affect focusing of photo-electrons into the holes of the F-R-MHSP itself. As in the case of the R-MHSP, here too we need to optimize the strip- and hole-voltages. The inter-strip voltage has to be large enough for better ion collection, while the hole-voltage has to be low enough for reaching lower IBF values in this element; in addition, the condition of photoelectron detection efficiency close to unity has to be fulfilled.

In our setup, the transfer field was set to 1kV/cm. In figure 5.24, the photoelectron detection efficiency of the F-R-MHSP is shown (E_{drift}=0.5 kV/cm). In each regime, the measurements were performed at different hole voltages of 310V, 320V, 340V and 360V.

We can see in figure 5.24 that:

1. The visible gain of the F-R-MHSP does not depend on variations in the inter-strip voltage. This can be considered as a first indication of a good focusing of photoelectrons into the holes (independent on the inter-strip voltage).

2. The photoelectron detection efficiency is low for small inter-strip voltages. This can be attributed to a partial collection of photoelectrons by the narrow anode strips. As we increase the inter-strip voltage, the efficiency is rising up, reaching a plateau.

3. The minimal hole-voltage which provides close to full photoelectron detection efficiency was measured to be 320V. It corresponds to a visible gain of ∼10 (figure 5.24).

Measurements with Cobra

As in the F-R-MHSP configuration, the strips of the Cobra multiplier are facing towards the drift region or to the PC. Therefore, the electron transfer to the next amplification

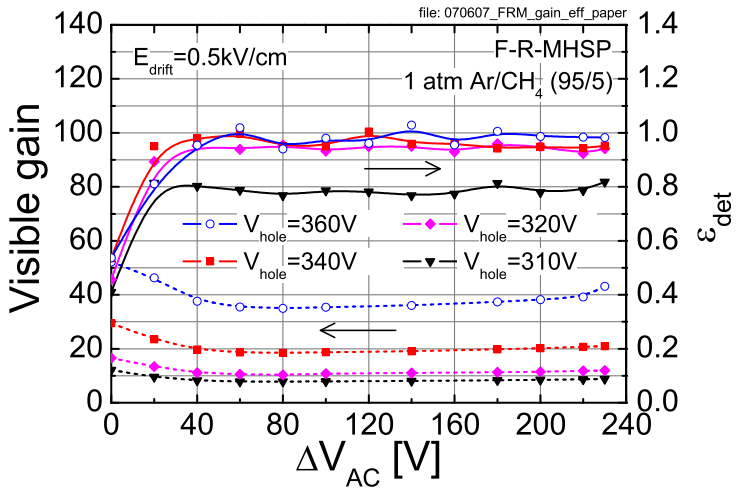

Figure 5.24: The visible gain (left y-axis, dashed lines) and the photoelectron detection efficiency (right y-axis, solid lines) as a function of the inter-strip voltage of a F-R-MHSP). Measurements performed at different values of hole voltage at E_{drift}=0.5 kV/cm.

stage is expected to be unaffected by varying the strip voltage. However, because of a sophisticated patterned electrodes on the top face, the increase of the inter-strip voltage difference could, in principle, affect focusing of photo-electrons into the holes of the Cobra itself. The inter-strip voltage has to be large enough for better ion collection, while the hole-voltage has to be low enough for reaching lower IBF values in this element; in addition, the condition of photoelectron detection efficiency close to unity has to be fulfilled.

In our setup, the transfer field was set to 1 kV/cm. In figure 5.25, the photoelectron detection efficiency of the Cobra is shown for E_{drift}=0.5 kV/cm; the measurements were performed at a hole voltage of 360V.

We can see in figure 5.25 that:

1. As in the R-MHSP multiplier, the visible gain of the Cobra decreases with the increase of inter-strip voltage.

2. The photoelectron detection efficiency is constantly low over the whole range of inter-

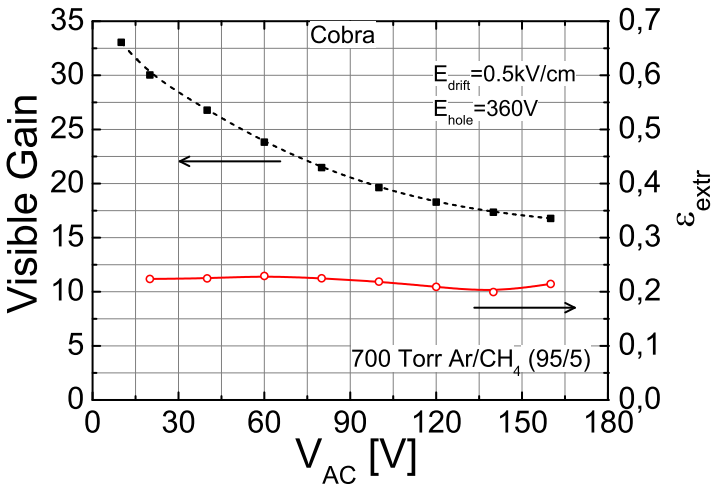

Figure 5.25: The visible gain (left y-axis, dashed line) and the photoelectron detection efficiency (right y-axis, solid line) as a function of the hole voltage of the Cobra (E_{drift} =0.5kV/cm).

strip voltages, reaching only 20%.

Measurements with GEM

The photoelectron detection efficiency of the GEM was not been measured earlier at a hole voltage lower than 320V [69]. The detection efficiency of a single GEM as a function of its visible gain is presented in figure 5.26. During measurements, the transfer field between the GEM and the MWPC was kept at 1kV/cm. It was found that the minimal hole voltage which permits the operation of the GEM at full detection efficiency for single electrons is around 280V. That corresponds to a visible gain of ∼10 on the GEM, that should permit the efficient transfer of at least a single electron from the hole avalanche.

5.4.4 Theoretical evaluation of single-photoelectron detection efficiency

In the setup for measurements of single-photoelectron detection efficiency (figure 5.21a), the investigated multiplier (either R-MHSP, F-R-MHSP, Cobra or GEM) was followed by a

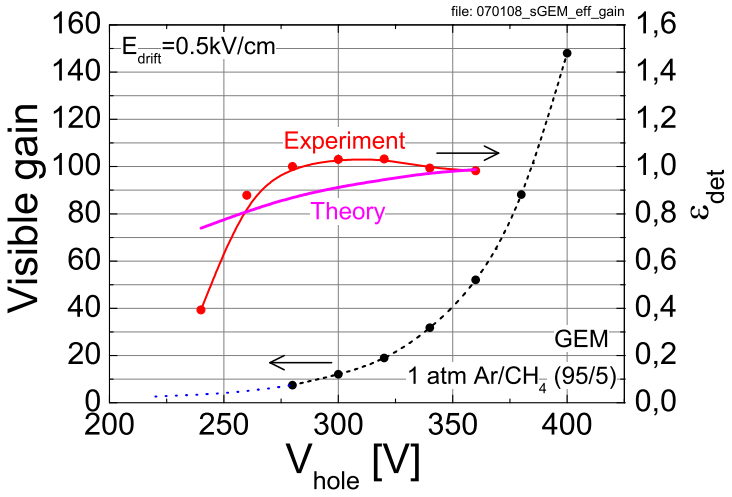

Figure 5.26: The visible gain (left y-axis, dashed line) and the photoelectron detection efficiency (right y-axis, thin solid line) as a function of the hole voltage of the GEM at E_{drift} =0.5kV/cm. For voltages below 280V (dotted line), the gain curve was extrapolated with an exponential function (dotted line). Thick solid line represents calculated ε_{det} values using equation 5.27.

reference MWPC multiplier with close to 100% electron detection efficiency as mentioned above. Therefore, one can assume that the photoelectron detection efficiency of either R-MHSP/MWPC, F-R-MHSP/MWPC, Cobra/MWPC or GEM/MWPC cascaded structures is simply the probability that at least one avalanche electron from the investigated multiplier is transferred to the MWPC. This probability $P_{trans}(N \geq 1)$ could be explicitly calculated.

In the setup depicted in figure 5.21a, let us consider a single photoelectron emitted from the PC. Following the direction of the drift field this electron enters the holes of the investigated multiplier with a probability ε_{hole} as indicated in equation 5.19. In the holes, the avalanche multiplication occurs; the probability $P(n)$ that the multiplication yielded n electrons is given by Furry probability function (equation 3.7 in section 3.4). After the multiplication, the avalanche electron charge is transferred to the MWPC with the probability ε_{trans} (equation 5.19), which represents a fraction of the avalanche electrons collected at the bottom electrode of the investigated multiplier.

Let us first calculate the probability that exactly one electron will be transferred to the MWPC from the investigated multiplier; it is given by the following expression:

$$P_{trans}(1) = P(1)\cdot\varepsilon_{trans} + 2\cdot P(2)\cdot\varepsilon_{trans}\cdot(1-\varepsilon_{trans}) + 3\cdot P(3)\cdot\varepsilon_{trans}\cdot(1-\varepsilon_{trans})^2 + ... \quad (5.21)$$

where $P(1)$, $P(2)$, $P(3)$, ... are Furry probabilities to create one, two, three, ... electrons in the avalanche occurring in the multiplier's holes. The first term, $P(1)\cdot\varepsilon_{trans}$, represents probability of transferring one electron to the MWPC from the avalanche that also yielded one electron. The second term, $2\cdot P(2)\cdot\varepsilon_{trans}\cdot(1-\varepsilon_{trans})$, is the probability that of two electrons produced in the avalanche, one will be transferred to the MWPC.

The successive terms in the equation 5.21 represent the probabilities that just one electron will be transferred to the MWPC from avalanches of various sizes. In equation 5.21 we assumed the $\varepsilon_{hole} = 1$ for simplicity.

The coefficients next to $P(1)$, $P(2)$, ... ,$P(l)$, ... are of binomial type $p(1|n) = \binom{n}{1}\cdot\varepsilon_{trans}\cdot(1-\varepsilon_{trans})^{n-1}$ with $n = 1, 2, ..., l, ...$; they represent the probability that only one electron out of n electrons created in the avalanche will be transferred to the MWPC.

In general case, the probability that k electrons, out of n electrons created in the avalanche, will be transferred to the MWPC is given by:

$$p(k|n) = \binom{n}{k}\cdot\varepsilon_{trans}^{k}\cdot(1-\varepsilon_{trans})^{n-k} \quad (5.22)$$

The total probability that N electrons will enter the MWPC after just one electron entered the testing multiplier could be written as follows:

$$P_{trans}(N) = \sum_{n=N}^{\infty} P(n)\cdot p(N|n) \quad or \quad substituting \quad 3.7 \quad and \quad 5.22$$

$$P_{trans}(N) = \sum_{n=N}^{\infty} \frac{1}{G}(1-\frac{1}{G})^{n-1}\cdot\binom{n}{N}\cdot\varepsilon_{trans}^{n}\cdot(1-\varepsilon_{trans})^{n-N} \quad (5.23)$$

where G is the multiplier's total gain. Here we sum over the different possibilities that will yield N electrons to be transferred to the MWPC. In equation 5.23, the condition $n \geq N$

has to be fulfilled. The sum can be computed utilizing the following relation:

$$\frac{1}{b!}\sum_{n=0}^{\infty}\frac{(\lambda+b)!}{\lambda!}\cdot a^{\lambda}=(1-a)^{-b-1}. \tag{5.24}$$

The probability that N avalanche electrons will be transferred to the MWPC is given by:

$$P_{trans}(N)=\frac{1}{G}\cdot\varepsilon_{trans}^{N}\cdot(1-\frac{1}{G})^{N-1}\cdot[1-(1-\frac{1}{G})\cdot(1-\varepsilon_{trans})]^{-N-1} \tag{5.25}$$

It is easy to show that at a large gain, which is the usual case in gaseous detectors, equation 5.25 could be approximated by:

$$\begin{aligned} P_{trans}(N)\cong\frac{1}{G\cdot\varepsilon_{trans}}\cdot exp(-\frac{N}{G\cdot\varepsilon_{trans}}) \quad or \\ P_{trans}(N)\cong\frac{1}{G_{vis}}\cdot exp(-\frac{N}{G_{vis}}) \end{aligned} \tag{5.26}$$

where $G_{vis}=G\cdot\varepsilon_{trans}$ is the visible gain by definition.

Finally, the probability $P_{trans}(N\geq 1)$ that at least one avalanche electron will be transferred to the MWPC is given by:

$$P_{trans}(N\geq 1)=1-P(0)=\frac{\varepsilon_{trans}\cdot(G+1)}{\varepsilon_{trans}\cdot G+1}\cong\varepsilon_{det} \tag{5.27}$$

It should reminded, that ε_{hole} was omitted. The correct probability $P_{trans}(N\geq 1)$ has to be multiplied by ε_{hole}. However, the ε_{hole} could be safely assumed to be unity for multipliers like GEM and R-MHSP at hole voltages exceeding 200V as indicated in [119, 84] and at low drift fields (as in our case).

Thus, we are able to calculate the probability $P_{trans}(N\geq 1)\cong\varepsilon_{det}$ as a function of the multiplier's total gain G and transfer efficiency ε_{trans} of avalanche electrons - quantities easily measurable in our setup in a current mode. The total gain G and transfer efficiency ε_{trans} were measured for GEM as a function of GEM voltage and for R-MHSP as a function of inter-strip voltage as shown in figure 5.27. The measurements were performed in the

setup shown in figure 5.21a with a transfer field of 1 kV/cm between the investigated multiplier (GEM or R-MHSP) and with the MWPC acting as an anode for charge collection. For the R-MHSP, the G and ε_{trans} were measured at hole voltages of 360V, 380V and 400V; the plot for 380V is presented, plots for different hole voltages look essentially similar.

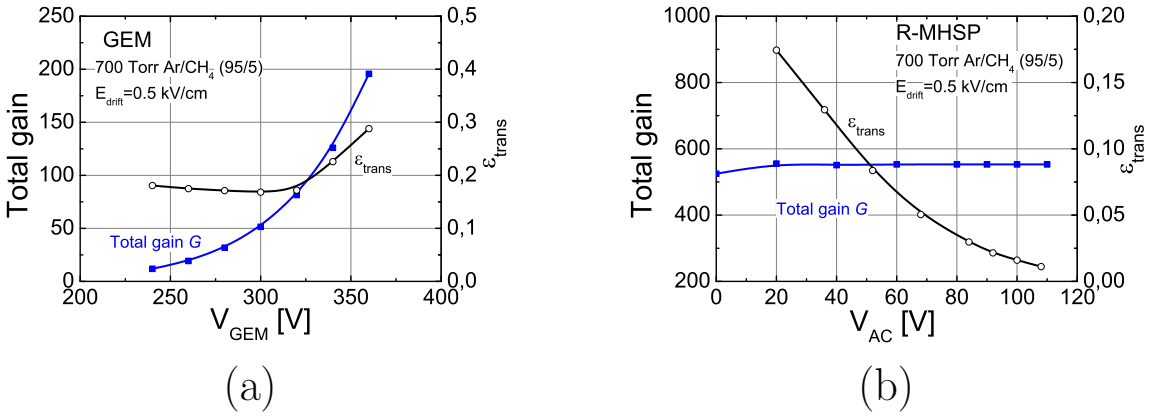

Figure 5.27: Total gain G and ε_{trans} as a functions of GEM voltage V_{GEM} a) and R-MHSP's inter-strip voltage V_{AC} b). In both cases, ε_{trans} was measured at E_{trans}=1 kV/cm.

The single photoelectron-detection efficiency ε_{det} estimated with equation 5.27 is plotted for GEM as a function of GEM voltage (figure 5.26) and for R-MHSP as a function of the inter-strip voltage (figure 5.28). The calculations for R-MHSP were performed at different values of hole voltage; those are indicated in the figure 5.28.

As seen in figure 5.26 and figure 5.28, the calculated ε_{det} values are in a reasonable agreement with the experiments. Similar calculations were not performed for Cobra and F-R-MHSP because the ε_{hole} for these multipliers can not be assumed to be unity.

5.4.5 Studies of ion blocking capability of the first element in a cascade

The IBF reduction capability of the first element was studied in a setup depicted in figure 5.29 with a first element being a GEM, a R-MHSP or a F-R-MHSP. It was followed by

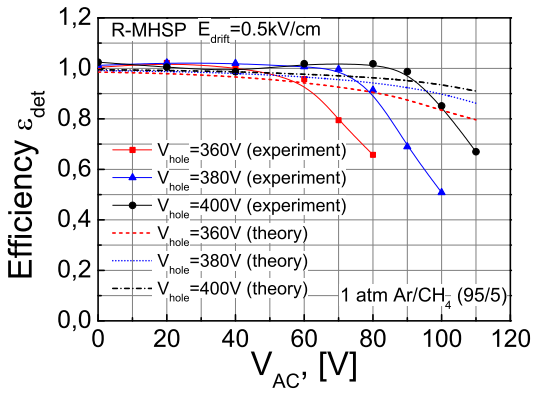

Figure 5.28: The measured (solid lines) and calculated (dashed lines) photoelectron detection efficiency as a function of the inter-strip voltage ΔV_{AC} of a R-MHSP at E_{drift}=0.5kV/cm. Measurements and calculations performed at different values of hole voltage.

a GEM, of which the avalanche acts as a source of back-flowing ions. This second GEM element was biased at 420V (gain ∼2000); the transfer field in the gap between the two elements was E_{trans}=1kV/cm and the drift field was E_{drift}=0.5kV/cm (figure 5.30).

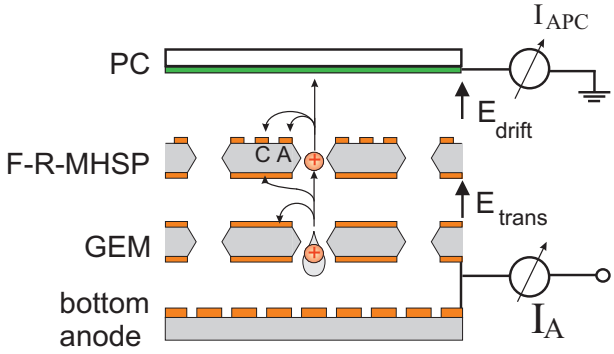

Figure 5.29: The schematic view of the setup for measurements of ion blocking capability of the F-R-MHSP. Here the GEM serves as a source of avalanche ions. The avalanche charge was collected at the interconnected GEM-bottom and bottom anode electrodes. Similar measurements were performed with R-MHSP, Cobra and GEM elements followed by a GEM.

The total avalanche current in this configuration was measured as the sum of currents from the bottom anode and the bottom GEM electrode (as shown in figure 5.29).

The IBF was calculated as the ratio of the PC avalanche current I_{APC} (under avalanche multiplication), to the total avalanche current I_A:

$$IBF = \frac{I_{APC}}{I_A} \tag{5.28}$$

Where the PC avalanche current I_{APC} was calculated as a difference of the total PC current under multiplication I_{TOTPC} and the initial I_{PC0} PC current: $I_{APC} = I_{TOTPC}$ - I_{PC0}.

The correlation between the IBF and the total gain (of both elements) measured in these conditions is presented in figure 5.30. The parameters (fixed and variable) in these measurements were the following:

- R-MHSP: the inter-strips voltage (ΔV_{AC}) varied from 0V to 60V and the hole voltage was set to 360V (following the results of previous section);
- F-R-MHSP: the inter-strips voltage (ΔV_{AC}) varied from 0V to 230V and the hole voltage was set to 320V (following results of the previous section);
- GEM, the hole voltage (V_{hole}) was varied in the range 280V-340V.

One can note that , the IBF measured with either the R-MHSP/GEM or the F-R-MHSP/GEM is 4-fold lower compared to that of a double-GEM, at a gain of $\sim 1.5 \cdot 10^4$ (figure 5.30). In these conditions, both the R-MHSP and the F-R-MHSP provided practically the same IBF values, of about 0.015.

5.4.6 IBF in cascaded multipliers incorporating R-MHSP, F-R-MHSP, "Cobra", GEM and MHSP elements

R-MHSP/GEM/MHSP and F-R-MHSP/GEM/MHSP cascaded multipliers

Systematic investigations were carried out in two types of cascades multipliers: the R-MHSP/GEM/MHSP (figure 5.31a) and F-R-MHSP/GEM/MHSP (figure 5.31b). The last

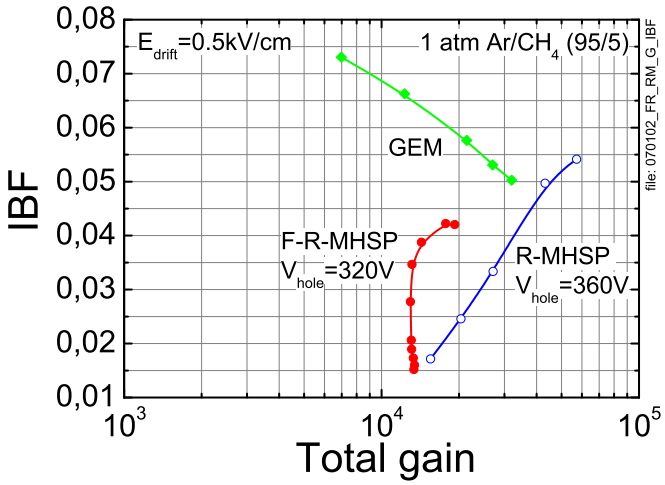

Figure 5.30: The IBF and total gain measured in the setup of figure 5.29 with R-MHSP/GEM, F-R-MHSP/GEM and 2GEM configurations at E_{drift}=0.5kV/cm. In the case of R-MHSP/GEM and F-R-MHSP/GEM the gain was varied by changing the inter-strip voltage from 0V to 60V and from 0V to 230V correspondingly; in the case of 2GEMs - by changing the hole voltage from 280V to 340V. The hole voltages of the R-MHSP and F-R-MHSP were fixed at the values indicated in the figure, to ensure full photoelectron detection efficiency.

MHSP element in each configuration was chosen based on its known 5-fold IBF reduction compared to a GEM [12], in addition to that of the two types of first-element multipliers investigated here. The optimized transfer- and induction-field configurations suggested in [12, 48] were combined with the insight from the F-R-MHSP and R-MHSP studies described above. The measurements were performed at E_{drift}=0.5kV/cm. The following parameters were chosen (see figure 5.31): E_{trans1}=1kV/cm; E_{trans2}=60V/cm (following [48]) and E_{ind}=-5kV/cm; the latter "reversed" field, permitted collecting most of the last-avalanche ions at the bottom mesh cathode (following [12]). The voltages across the holes and between strips for different elements were the following: The first-element voltages were chosen according to the results described above: V_{hole1}=320V; ΔV_{AC1}=230V for the F-R-MHSP and V_{hole1}=360V; ΔV_{AC1}=60V for the R-MHSP. The GEM and MHSP potentials were chosen as follows: for the F-R-MHSP/GEM/MHSP: V_{GEM1}=275V, E_{trans2}=75V/cm;

for the R-MHSP/GEM/MHSP: V_{GEM1}=300V, E_{trans2}=100V/cm.

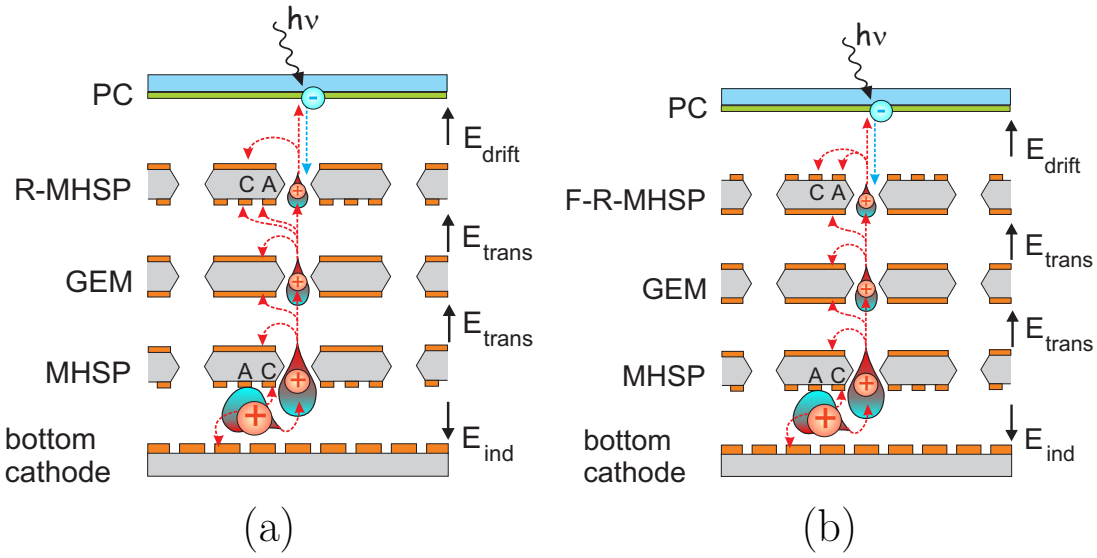

Figure 5.31: Schemes of cascaded R-MHSP/GEM/MHSP (a) and F-R-MHSP/GEM/MHSP (b) multipliers coupled to a semi-transparent photocathode; possible avalanche ions paths are also shown.

The last-element MHSP multiplier was polarized, in both setups, as follows: V_{hole2}=370V and ΔV_{AC2} was varied between 140V and 230V, to adjust the total gain of the whole cascaded detector.

The IBF distribution is presented in correlation with the total gain (figure 5.32). The lowest IBF value reached was $3{\cdot}10^{-4}$ for the F-R-MHSP/GEM/MHSP and $9{\cdot}10^{-4}$ for R-MHSP/GEM/MHSP, at a detector total gain of $\sim 10^5$. It means that per single-photon event, on the average, 30 or 90 ions reach the PC in a cascaded detector with a F-R-MHSP or a R-MHSP first-element multiplier, correspondingly.

Cobra/2GEM cascaded multiplier

The Cobra/2GEM cascaded multiplier shown in figure 5.33a was investigated. The voltages across the holes and between strips for different elements were the following: The

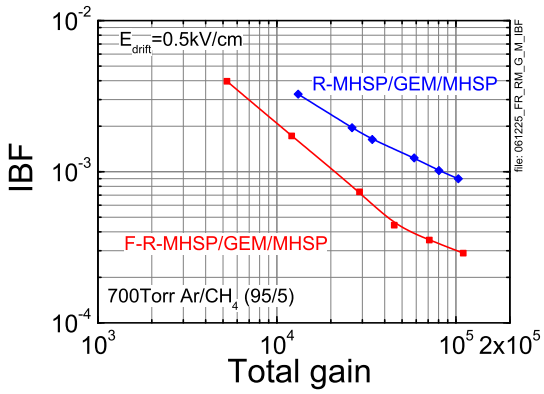

Figure 5.32: The IBF in correlation with the total gain of the R-MHSP/GEM/MHSP (figure 5.31a) and F-R-MHSP/GEM/MHSP (figure 5.31b) cascaded detectors, with semitransparent photocathodes; the IBF is plotted for a drift field of 0.5kV/cm.

Cobra voltages were chosen as follows: V_{hole1}=360V; ΔV_{AC1}=140V; both transfer fields were set to be 1kV/cm; the voltages on both GEMs were simultaneously varied between 200V and 340V, to adjust the total gain of the whole cascaded detector.

5.4.7 Discussion on IBF reduction in micro-hole multipliers

In this section we described the results on the systematic studies of IBF reduction in cascaded electron multipliers, searching for further improvements that will permit stable GPM operation.

Following the 5-fold IBF reduction of the MHSP as a last cascade-element [12], we studied the ion trapping properties of the Reversed-bias MHSP (R-MHSP). In the latter, the narrow strips are biased more negative than the broader ones; charge multiplication occurs only within the holes while the more-negative narrow cathode-strips only collect a fraction of the ions. The R-MHSP, with its hole-multiplication, can be used anywhere in the cascade, and especially as a first element, trapping back-flowing ions from all successive elements, but not its own ions. We also investigated here a third operation mode of the MHSP element: the "flipped Revered-bias Micro-Hole & Strip Plate" (F-R-MHSP)

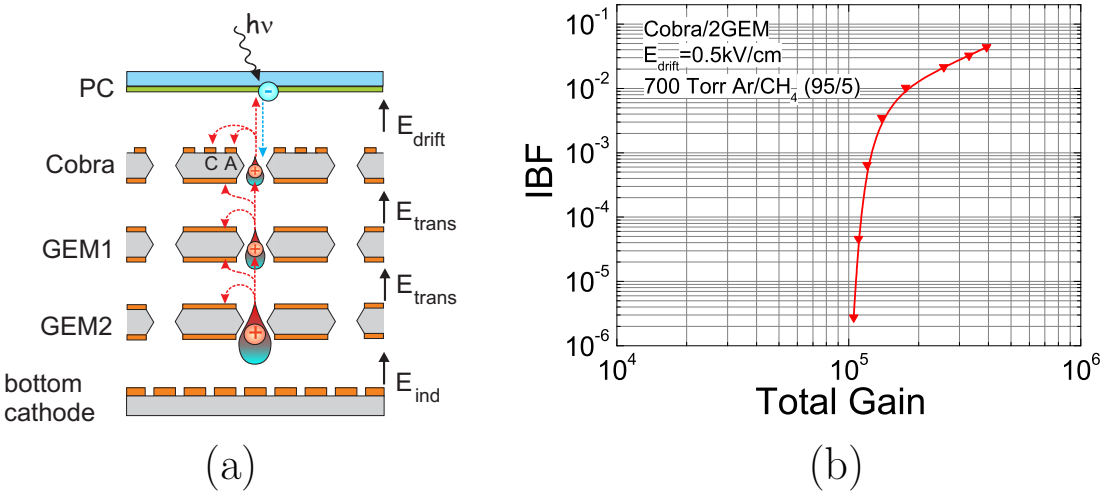

Figure 5.33: a) Scheme of cascaded Cobra/2GEM multiplier coupled to a semi-transparent photocathode; possible avalanche ions paths are also shown. b) The IBF in correlation with the total gain of the Cobra/2GEM cascaded detector, with semitransparent photocathode (E_{drift}=0.5kV/cm).

with the strips facing towards the drift region. This operation mode permitted uniquely capturing both: its own ions and that induced by the avalanches of the successive cascade elements. The F-R-MHSP is therefore best suitable as the first element of a cascaded multiplier.

A systematic comparative study of the F-R-MHSP, R-MHSP and GEM elements yielded operation conditions with full collection efficiency of primary electrons into the multiplying holes and the efficient avalanche-electrons transfer into the following elements of a cascade. Conditions were found in which the inter-strip potentials in the F-R-MHSP and R-MHSP were optimized for both: electron collection and ion blocking.

It was found that for R-MHSP at hole voltages of 360V, 380V and 400V, the inter-strip potential can be raised to 60V, 70V and 90V correspondingly, maintaining full single-electron detection efficiency. This was measured at a fixed transfer field of 1kV/cm. Further increase of the transfer field will allow further increase of the inter-strip voltages; this will

allow to divert more ions to the cathode strips, with no sacrifice to the photoelectron detection efficiency.

Field distortions in the drift region, at the hole vicinity, due to the applied F-R-MHSP inter-strip voltage, did not affect the electron focusing into the hole apertures under the current operation conditions (figure 5.24). This is due to the very intense focusing field in the hole vicinity which is effectively focusing the drifting electrons. It should be mentioned that, the drift field is not uniform within a small region of few hundred microns above the F-R-MHSP's top surface (figure 5.18(c)), in which the back-flowing ions are trapped. The main limitation on the detection efficiency of the F-R-MHSP arises from insufficient multiplication within the holes; full detection efficiency, in the present operation conditions, was reached for hole voltages exceeding 320V at a transfer fields of 1kV/cm.

A theoretical model was introduced for estimation of single-photoelectron detection efficiency ε_{det}. The input parameters of the model are total gain G and transfer efficiency ε_{trans}; they could be easily measured in continuous mode. The single-photoelectron detection efficiency was estimated with the model for the R-MHSP and for the GEM; the estimations were in a reasonable agreement with the experimental results.

The ion blocking capability was studied in cascaded detector configurations where a GEM, R-MHSP or F-R-MHSP was used as the first element, followed by a GEM; the latter served as the source of avalanche ions.

The experiment showed 4-fold lower IBF with either first-element R-MHSP or F-R-MHSP, compared with that of a standard GEM. It should be noted however that it was not possible to maintain both high gain (above 10^4) and low IBF in "GPM conditions", for the detector comprised of only two multiplication stages. Naturally, additional elements could be added to the cascade to provide higher total gains.

In the F-R-MHSP/GEM/MHSP detector with a semitransparent PC, the IBF value reached in a GPM mode (E_{drift}=0.5kV/cm), compatible with full single-electron detection efficiency, was $3{\cdot}10^{-4}$ at a total gain of $\sim 10^5$. This record IBF value seems to be sufficient for a stable operation of the multiplier in combination with a visible-light sensitive photocathode (e.g. bi-alkali) as **it fulfills our requirement that a gain of 10^5 required**

for high single-photon sensitivity in GPMs implies $IBF < 3,3 \cdot 10^{-4}$. With the resulting 30 ions impinging on the photocathode per single-photoelectron event, a bi-alkali PC will induce on the average 0.6 secondary electrons (calculated according to [10]). However, one should keep in mind that the number of secondary electrons can fluctuate, due to fluctuations of the number of electrons in individual avalanches; therefore there could be more than one secondary electron per avalanche. This phenomenon is well understood for low-pressure gases setting the condition for breakdown. The breakdown does not occur as far as the average number of secondary electrons liberated from the PC by the back-flowing avalanche ions is below one [50]. At high pressures this condition could not always be applicable, because of possible space charge formation [120] at the PC vicinity. It is probable, however, that at low IBF values, the space charge formation will be prevented and the above mentioned condition for breakdown will be held.

The concept of the Cobra electrode has been recently investigated. It was found that when introduced as a first element (with the patterned area pointing towards the photocathode), preceding two GEMs in the cascade, it drastically improved the ion trapping capability. With a drift field of 0.5 kV/cm, we measured IBF values of $3 \cdot 10^{-6}$ which is 10,000 times lower than that of cascaded triple GEMs. These are the lowest IBF values ever reached in gaseous detectors. However, while the F-R-MHSP yielded full photoelectron collection efficiency into the holes of the first cascade element, the Cobra, in its present geometry, had a limited electron collection efficiency of about 20%. This could be attributed to non-optimal geometrical parameters of the Cobra pattern. The photoelectron collection in the Cobra could be improved by increasing the fraction of the area covered by anode electrodes surrounding the holes and decreasing the area covered by more negatively biased cathode electrodes.

Further reduction of the IBF could be reached naturally with additional patterned hole multipliers in the cascade. We are presently investigating the idea of double-face patterned hole-multipliers, with ion-defocusing strips running on both faces

5.5 High-gain operation of visible-sensitive GPMs

Following the success in ion back-flow reduction, full understanding of ion-induced secondary emission process and after mastering the technique for production of highly efficient alkali-antimonide PCs, the next step the assembly and investigation of visible-sensitive GPMs capable of continuous-operation at a high gain. In this section we demonstrate, for the first time, the possibility of reaching gains of $\sim 10^5$ in continuous-mode operation in a visible-sensitive GPM.

5.5.1 GPMs assembly and experimental methods

F-R-MHSP/GEM/MHSP based GPM

A multiplier configuration comprising a F-R-MHSP followed by GEM and MHSP was coupled to a visible-sensitive semitransparent K_2CsSb PC on a glass substrate. The multiplier was installed in the *detection* chamber of the UHV system; the PC was prepared in the *activation* chamber and transferred to the detection chamber and placed on top of the multiplier (figure 4.4). The PC production procedure and the multiplier installation are described in section 4.2.

The detector and the electric scheme are shown in figure 5.34. Photoelectrons are efficiently focused into the F-R-MHSP holes under a drift field E_{drift}; following a multiplication process in the holes, avalanche electrons are transferred under a transfer field, E_{trans1}, into the GEM, for additional multiplication, the avalanche electrons are then extracted by the transfer field E_{trans2} from the GEM holes and transferred to the MHSP, an additional two-stage multiplication process occurs (see section 3.4.1). The total avalanche charge is collected at the anode of the MHSP. The avalanche ions, in turn, drift back following the same electric field lines; most of them are captured by the various electrodes and only a small fraction reaches the PC as shown in figure 5.34. The electrodes of the GPM were biased independently with HV power supplies (type CAEN N471A) through 40 MΩ resistors (figure 5.34); the PC was kept at ground potential. The multiplication

(gain) curves of the detectors were deduced from the ratio of the anode current (I_A) to the photocurrent emitted, without multiplication, from the PC (I_{PC}). The operation voltages applied to various electrodes of the multiplier were those indicated in section 5.4.6. We varied the inter-strip voltage on the bottom MHSP, to vary the total gain of the detector.

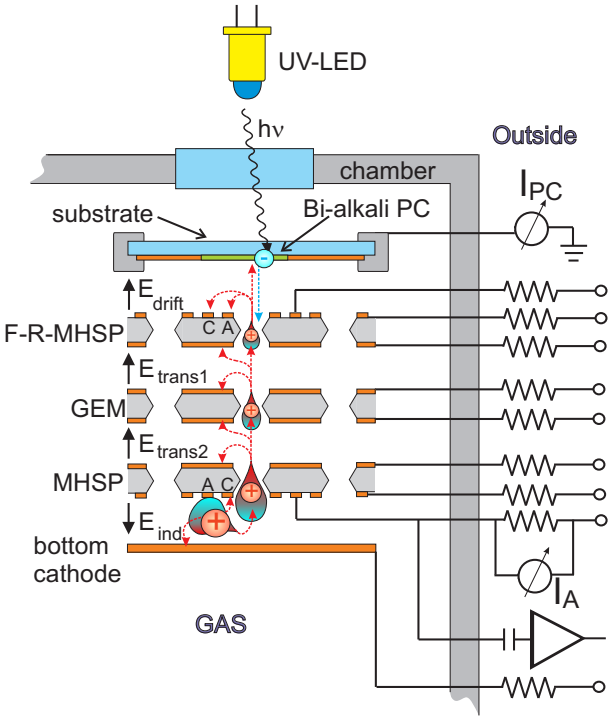

Figure 5.34: Schematic view of a F-R-MHSP/GEM/MHSP gaseous photomultiplier assembly in the detection chamber, with a semitransparent photocathode. Photoelectrons are extracted from the photocathode into gas; they are efficiently focused into the holes of F-R-MHSP and multiplied; avalanche electrons are transferred into the GEM holes and then to the MHSP for the final multiplication. The avalanche ions (their possible paths are depicted by dotted arrows), in turn, drift back following the same electric field lines; some of them are captured by various electrodes and only a minor fraction reaches the PC. The GPM's gain and ion back-flow were established in continuous operation mode by recording currents at the MHSP anode and at the PC; in the counting operation mode, the pulses were recorded at the MHSP anode, capacitively decoupled from a charge preamplifier.

Cobra/2GEM and 2GEM/Cobra/GEM based GPMs

A GPM comprising a Cobra multiplier followed by two GEMs was coupled to a semitransparent K_2CsSb PC as shown in figure 5.35a. The photoelectrons were focussed (inefficiently, with just 20% collection efficiency as pointed out in section 5.4.3) into the holes of the Cobra and pre-amplified; the avalanche electrons were extracted by the first transfer field and focussed into the double-GEM cascade for additional multiplication. The total avalanche charge was collected on the bottom electrode of the last GEM interconnected with the bottom anode plate. The avalanche ions of the whole cascade were trapped by the negatively-biased electrodes on the top face of the Cobra. The multiplication curves of the detectors were deduced from the ratio of the avalanche current (I_A) to the photocurrent emitted, without multiplication, from the PC (I_{PC}). The operation voltages applied to various electrodes of the multiplier were those indicated in section 5.4.6. We varied the hole-voltage on both GEMs simultaneously, to vary the total gain of the detector.

As mentioned above and in section 5.4.3, the multipliers having a Cobra as a first element in the cascade show poor detection efficiency for single photoelectrons. Therefore, another configuration was investigated, in which two GEMs were followed by a Cobra multiplier and by another GEM (figure 5.35b). The photoelectrons were efficiently collected by the first GEM and amplified by the second GEM; then the avalanche charge was transferred to the Cobra (though with low efficiency) and to the last GEM for additional multiplication. A grand majority of avalanche ions created in the last two elements of the cascade were trapped by Cobra, while those ions created in the first two GEMs were just partly blocked by the GEM electrodes. As in the previous case, the total avalanche charge was collected on the bottom electrode of the last GEM interconnected with the bottom anode plate. The multiplication (gain) curves of the detectors were deduced from the ratio of the avalanche current (I_A) to the photocurrent emitted, without multiplication, from the PC (I_{PC}). The operation voltages applied to various electrodes of the multiplier were the the following (figure 5.35b): drift field E_{drift}=0,5 kV/cm, first GEM hole voltage V_{GEM1}=280V, first transfer field E_{trans1}=2kV/cm, second GEM hole voltage V_{GEM2}=315V,

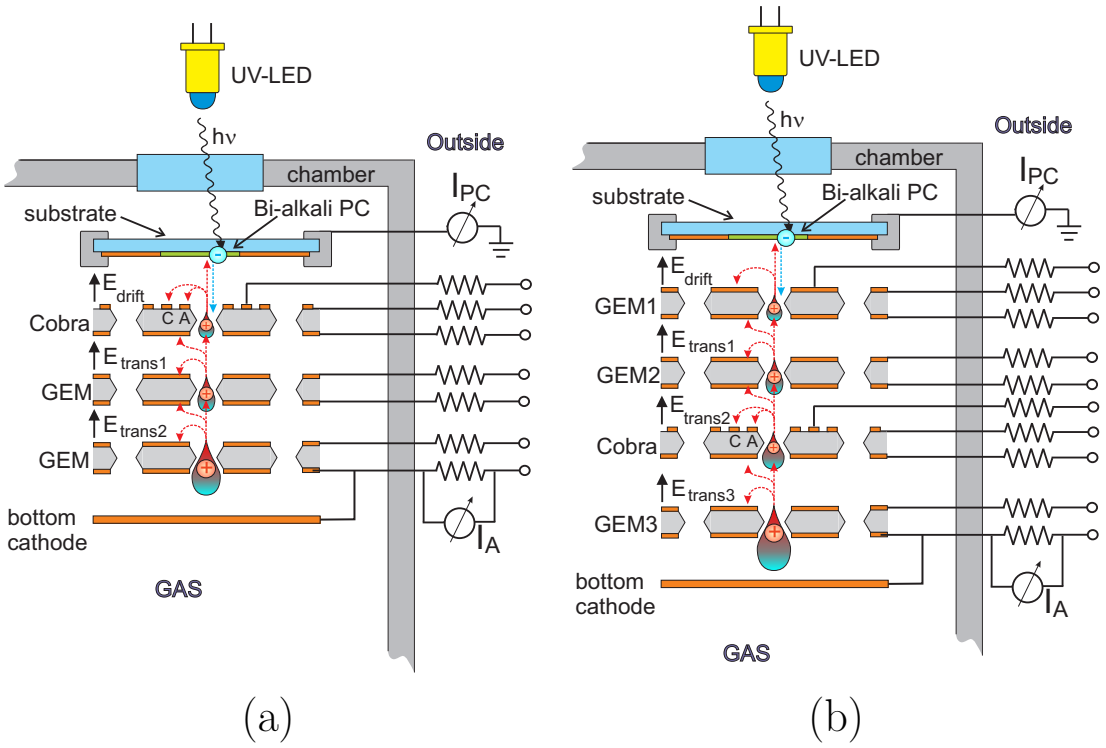

Figure 5.35: Schematic view of Cobra/2GEM and 2GEM/Cobra/GEM multipliers with a bi-alkali semitransparent PC for high gain operation in continuous mode. The electron multiplication in each cascade element and possible paths of the avalanche ions are also shown.

second transfer field E_{trans2}=1kV/cm, Cobra hole voltage V_{chole}=350V, Cobra inter-strip voltage V_{AC}=150V and third transfer field E_{trans3}=1kV/cm. To vary the total gain of the detector, we adjusted the hole voltage on the last GEM. In order to compensate for the loss of electrons entering the Cobra, the cascade of the first two GEMs operated at the conditions corresponding to a visible gain of 50 measured at the top face of the Cobra.

5.5.2 Operation in continuous mode

F-R-MHSP/GEM/MHSP based GPM

The QE as a function of photon wavelength for the semitransparent K_2CsSb PC of the GPM with the F-R-MHSP/GEM/MHSP multiplier was measured in vacuum and in Ar/CH_4

(95/5) at 700 Torr as shown in figure 5.36. Its QE value in vacuum approached 27% at 375 nm, while in the gas, with a drift-field of 0.5 kV/cm, it was reduced to about 12% due to backscattering.

In figure 5.37 we present gain-voltage characteristics for the cascaded GPM of figure 5.34, with K_2CsSb and CsI PCs, for comparison. The measurements were carried out in Ar/CH_4 (95/5) at 700 Torr. The GPM was constantly illuminated with a UV-LED as described in section 4.2. The gain-voltage curve measured with CsI PC (solid line in figure 5.37) shows exponential behavior; the data points for K_2CsSb PC coincide with the same curve. In both cases, with IBF-value of $3 \cdot 10^{-4}$, **the GPM could reach a gain of 10^5** with no divergence from an exponential gain-voltage characteristic, indicating upon full suppression of ion feed-back effects. There were no attempts made to reach higher gains.

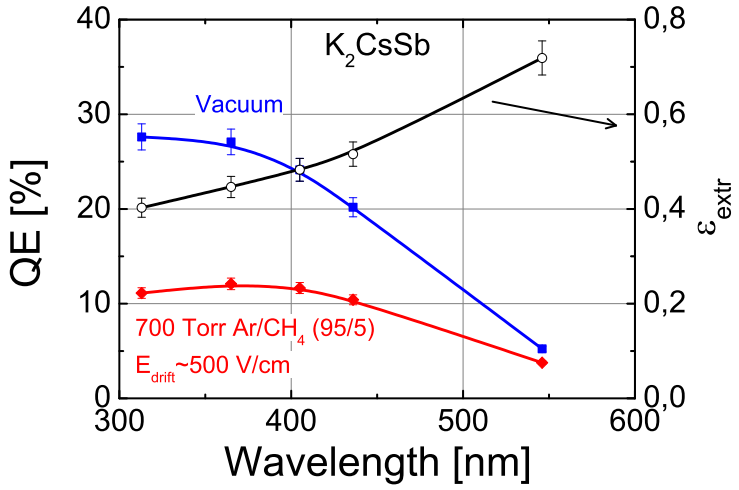

Figure 5.36: The QE as a function of wavelength in vacuum (squares) and in the gas (diamonds) for the K_2CsSb PC used for high gain continuous operation with the F-R-MHSP/GEM/MHSP multiplier. The fraction ε_{extr} of photoelectrons surmounted backscattering as a function of photon wavelength is also presented (open circles).

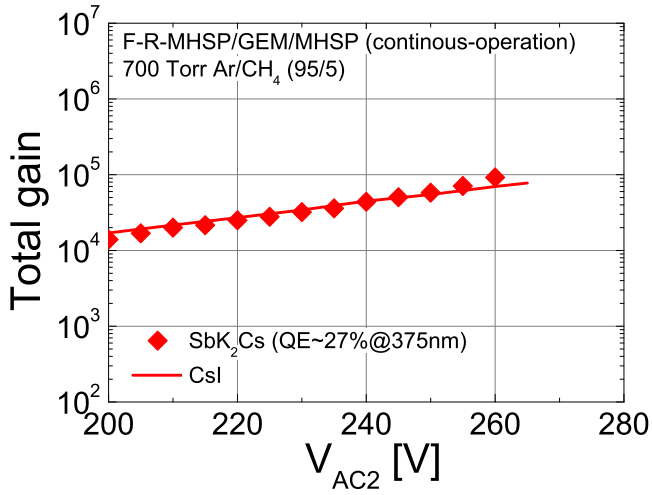

Figure 5.37: Gain-voltage characteristics of the detector shown in figure 5.34 with the K_2CsSb of figure 5.36 (diamonds) and CsI (straight line) photocathodes. The gain-voltage characteristic of CsI PC is known to have exponential behavior; the data points for K_2CsSb PC lie on the curve measured with CsI PC showing no divergence from exponential. 700 Torr Ar/CH_4 (95/5); E_{drift}=0.5 kV/cm.

Cobra/GEM/GEM and 2GEM/Cobra/GEM based GPMs

In the GPM with the Cobra/2GEM multiplier, the best ever fabricated K_2CsSb PC was employed. Prior to gas filling, it was stored in vacuum for half a day; during this period a minor QE decay was observed. The peak QE value of the decayed PC was measured to be 53% (figure 5.36) at 365 nm; the gas was introduced immediately after the QE measurement. The maximal effective QE in gas was ∼27%, as shown in figure 5.36.

The Cobra/2GEM detector with the K_2CsSb PC (figure 5.35a) was investigated in continuous operation mode; the gain-voltage plots are shown in figure 5.38b, in comparison with a CsI PC. The measurements were carried out in Ar/CH_4 (95/5) at 700 Torr. The exponential fits to the data points measured with K_2CsSb and CsI PC are represented by solid and dashed curves, correspondingly. As can be seen in figure 5.38b, gain exceeding 10^5 was achieved with both PC types. There were no feed-back effects (with the present

IBF-value of $3 \cdot 10^{-6}$) as can be seen from the exponential shape of the gain-voltage curve.

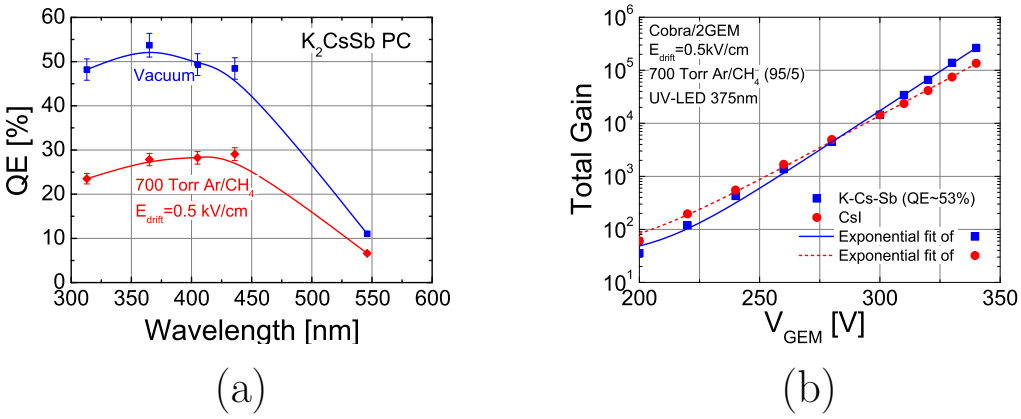

Figure 5.38: a) The QE as a function of wavelength for the K_2CsSb PC which was coupled to the Cobra/2GEM cascaded multiplier measured in vacuum (squares) and in 700 Torr Ar/CH_4 (95/5) (diamonds). b) Gain-voltage characteristics of the Cobra/2GEM cascaded GPM of figure 5.35a, with K-Cs-Sb (squares) and CsI (circles) photocathodes. The data were fitted with exponential functions. 700 Torr Ar/CH_4 (95/5); E_{drift}=0.5 kV/cm. QE refers to vacuum.

The gain-voltage characteristics of the 2GEM/Cobra/GEM multiplier coupled to a K_2CsSb PC (vacuum QE∼34%) and to a CsI PC are shown in figure 5.39. A gain-voltage curve shows no divergence from exponential up to a gain of 10^4; at higher gains the curve start diverging because of worse ion-blocking of the first two GEMs in the cascade (IBF∼ $8 \cdot 10^{-3}$). The primary photoelectrons were effectively collected in this multiplier configuration. The IBF as a function of gain of the 2GEM/Cobra/GEM multiplier is also shown in figure 5.39.

5.5.3 Operation in pulsed-illumination mode

Single photon sensitivity

In pulsed-illumination mode, the detector was illuminated with short light flashes from the UV-LED. In order to demonstrate single-photon sensitivity of the GPM, the amount

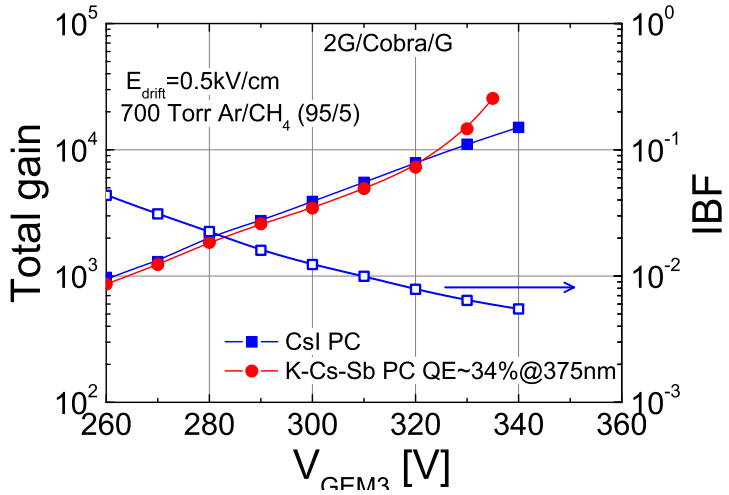

Figure 5.39: Gain-voltage characteristics of the 2GEM/Cobra/GEM multiplier shown in figure 5.35b with a K_2CsSb of (circles) and CsI (squares) photocathodes. The IBF as a function of gain is also shown (open squares). 700 Torr Ar/CH_4 (95/5); E_{drift}=0.5 kV/cm. QE refers to vacuum.

of photons was reduced to few photons per flash, with light absorbers and by adjustment of the pulse-width and amplitude. Pulse-height spectra of single-photon events were acquired with a F-R-MHSP/GEM/MHSP multiplier coupled to a K_2CsSb PC (vacuum peak QE∼27%) with different values of anode-to-cathode voltages ΔV_{AC} of the multiplier's MHSP. The single photon pulses were recorded at the MHSP anode capacitively decoupled from the high voltage by a charge-sensitive preamplifier followed by a pulse-shaping linear amplifier; they were then fed into a multi-channel analyzer, providing pulse-height spectra. The signal-readout electronics was calibrated with step-pulses of various heights. The spectra were recorded at ΔV_{AC}=265, 270 and 275V, corresponding to VSGPM gains of approximately $1.2 \cdot 10^5$, $1.5 \cdot 10^5$ and $1.8 \cdot 10^5$. The gains were estimated by fitting each pulse-height spectrum with an exponential function (figure 5.40). The noise spectrum for each anode-to-cathode voltage was recorded separately at the same conditions with the UV-LED switched off. The noise spectrum was later subtracted from the experimental one for each anode-to-cathode voltage. The resulting spectra are shown in figure 5.40. The exponential-shape of the spectra presented in figure 5.40 proves that the recorded pulses

indeed originate from single photoelectrons. The slightly peaked distributions at the lower pulse-heights, is probably due to an over estimated (subtracted) electronic noise.

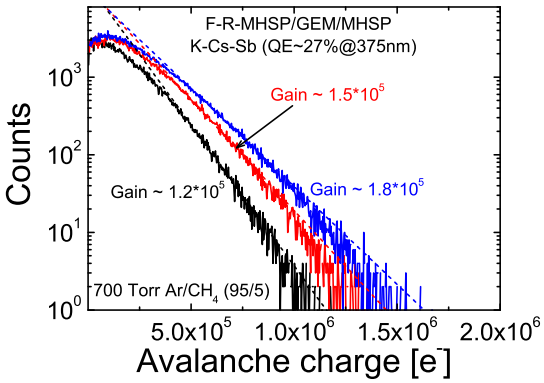

Figure 5.40: Single-electron pulse-height spectra obtained for a GPM comprised of F-R-MHSP/GEM/MHSP multiplier coupled to K_2CsSb PC of **??** with MHSP anode voltages ΔV_{AC}=265, 270 and 275V, corresponding to respective gains of $1.2 \cdot 10^5$, $1.5 \cdot 10^5$ and $1.8 \cdot 10^5$. Each spectrum was fitted with an exponential function.

Stability of GPM operation

The stability of the GPM was studied in the same setup. The F-R-MHSP/GEM/MHSP multiplier coupled to a K_2CsSb PC was illuminated with multiple-photon flashes from the UV-LED. It was illuminated for 14 hours at an average photon rate of ∼12kHz/mm^2 resulting in a total charge of ∼125 μC collected at the MHSP's anode at a gain of 10^5; no sparks were recorded during the operation time. Charge pulses were recorded at the detector's anode when starting the irradiation and after 14 hours of operation at a gain 10^5. The oscillogram of the detector signal recorded at the anode of the MHSP with the charge sensitive preamplifier followed by the linear amplifier is shown in figure 5.41: the initial detector signal is shown in figure 5.41a, the detector signal after 14 hours of operation at a gain 10^5 is shown in figure 5.41b. The electronic noise was filtered out by averaging over 64 frames. The signal's amplitude decreased by 14% of its initial value; this signal decay

could be related to gain variation due to initial charging up phenomena of the multiplier's polymer substrates, currently observed in micro-pattern multipliers [121, 122], and not by the PC decay. figure 5.42 indeed confirms the PC stability throughout the study; it depicts the QE of the K_2CsSb photocathode as a function of wavelength at different stages of the experiment. The QE was measured in vacuum for the freshly produced PC, then following gas introduction (at an electric field of 500 V/cm at the PC in 700 Torr Ar/CH_4 (95/5)) and after 14 hours of operation in the detection chamber with the F-R-MHSP/GEM/MHSP multiplier at a gain of 10^5. The QE was practically not affected during its operation with the multiplier; the small decrease in QE observed at 436 nm is within the measurement accuracy.

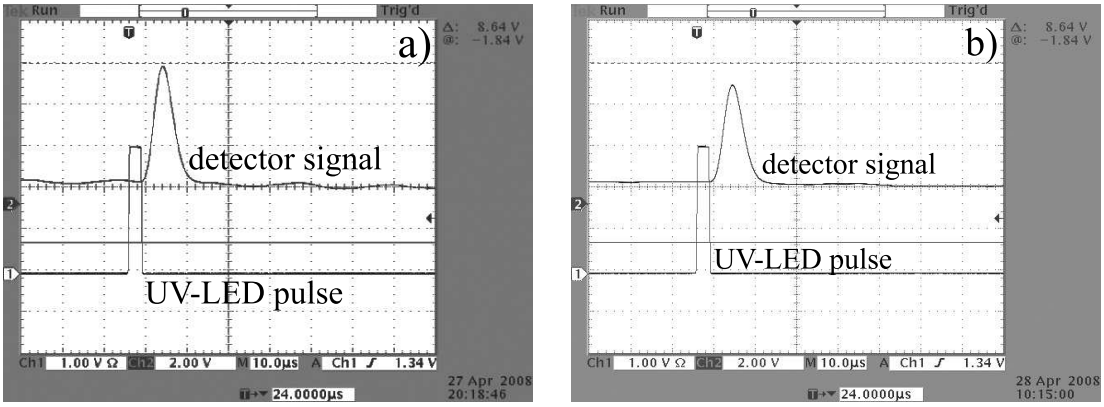

Figure 5.41: The output multiple photon pulse recorded for F-R-MHSP/GEM/MHSP multiplier coupled to K_2CsSb PC (the PC characteristics presented in figure 5.37) at conditions corresponding to a detector gain of 10^5; initial signal a), the signal after 14 hours of operation b). The PC was illuminated with UV-LED which was powered by the pulse generator; the output pulse of the generator is shown.

Output pulse

An example of a single pulse induced by a photon-flash, recorded in a GPM comprising the F-R-MHSP/GEM/MHSP multiplier coupled to a CsI PC, is shown in figure 5.43. The

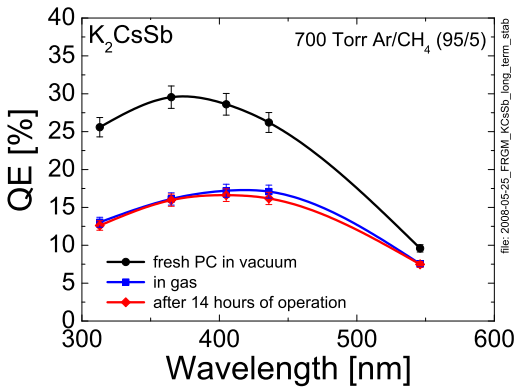

Figure 5.42: The QE of the K_2CsSb photocathode measured in vacuum (circles) at 700 Torr Ar/CH_4 (95/5), immediately after gas introduction (squares) and after 14 hours operation in detection chamber with F-R-MHSP/GEM/MHSP multiplier at a gain of 10^5 (diamonds).

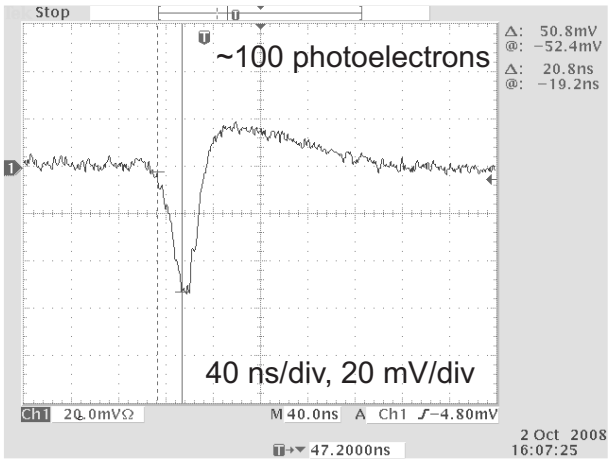

Figure 5.43: An example of a pulse recorded at the anode strips of MHSP of F-R-MHSP/GEM/MHSP multiplier.

pulses were recorded in the experimental setup described in 4.1 with a fast current-sensitive preamplifier (0.5 ns rise-time) connected directly to the MHSP anode. The GPM's PC was illuminated by light flashes from a H_2-filled discharge lamp. The pulses were recorded at a multiplier's gain of $\sim 3 \cdot 10^4$. The pulse in figure 5.43 is of ∼100 photoelectrons; it has a characteristic rise-time of ∼20 ns).

5.5.4 Discussion on the high-gain continuous operation of visible-sensitive GPMs

Three visible-sensitive GPM configurations with F-R-MHSP/GEM/MHSP, Cobra/2GEM and 2GEM/Cobra/GEM cascaded multipliers coupled to K_2CsSb PCs were investigated. **The GPMs with F-R-MHSP/GEM/MHSP and with Cobra/2GEM multipliers yielded, for the first time, stable operation at record gains of 10^5 in continuous operation mode, free of feedback effects.** The ultimate ion-blocking of the Cobra/2GEM multiplier, permitted operating the GPM with a highly-efficient K_2CsSb PC (peak vacuum QE of 53% at 365 nm) at high gain, but with low photoelectron collection efficiency. On the other hand, **GPM with F-R-MHSP/GEM/MHSP multiplier was operated with full photoelectron detection efficiency**. To avoid the loss of photoelectrons, we also investigated a GPM with a 2GEM/Cobra/GEM multiplier; a gain of 10^4 was reached in continuous operation mode, limited by ion-feedback due to insufficient ion blocking (IBF$\sim 8 \cdot 10^{-3}$ compared to $3 \cdot 10^{-4}$ in the optimal multiplier). However, this configuration assured the full photoelectron collection efficiency.

The performance of the visible-sensitive GPM with the F-R-MHSP/GEM/MHSP cascaded multiplier was studied also under pulsed-illumination with short light flashes, the latter could be reduced down to a single-photon levels. Single-photon sensitivity was demonstrated. A multiple photoelectron pulses were recorded with a fast current preamplifier; they had a typical rise-time of 20 nS, sufficient for providing timing properties in the ns range (similar to cascaded-GEM GPMs [10]). The detector's at a gain of 10^5 was demonstrated for 14 hours, at a photon rate of $\sim$12kHz/mm^2 resulting in $\sim 125\mu$C of a total charge collected at the MHSP's anode.

Chapter 6

Summary and conclusions

In this work we demonstrated, for the first time, the possibility of conceiving gas-avalanche photomultipliers (GPMs) for the visible spectral range, capable of operation at high multiplication gains, in a continuous (DC) mode. The novel GPMs combine thin-film alkali-antimonide photocathodes coupled to state-of-the-art cascaded gaseous electron multipliers.

These photon detectors, with single-photon sensitivity, have many attractive properties. Unlike vacuum PMTs, they operate at atmospheric pressure; this permits conceiving large-area detectors (up to m^2) with flat geometry; unlike vacuum, the gas multiplication provides immunity to high magnetic fields. The GPMs have a slower response (in the ns range), compared to PMTs, but a superior localization accuracy ($\sim$0.1 mm for single photons with standard gas-detector readout). They naturally compete with solid-state detectors in size, possibly in noise characteristics, but not in quantum efficiency (QE). Their effective quantum efficiency is lower than that of vacuum devices, due to photoelectron losses by backscattering on gas molecules. Best expected values are about 80% of the vacuum QE ones.

The success of the present research, following a few decades of tedious R&D by numerous groups, is due, among others, to two major factors:

1. A better understanding and studies of the processes involved in the avalanche-ions transport and impact on the photocathodes, and

2. The breakthrough reached in this work in avalanche-ion blocking, without photoelectron losses, with novel cascaded hole-multipliers having patterned ion-defocusing electrodes.

We found it convenient to discuss in detail the research results at each of the thesis sections; therefore only a more general summary is provided here.

Alkali-antimonide visible-sensitive photocathodes

In the visible-sensitive GPM we employed alkali-antimonide photocathodes; they were laboratory-produced by chemical vapor deposition, suitable for large-area active surfaces. We found optimal conditions for producing high-QE (exceeding 50% in vacuum at 360-400 nm) K_2CsSb photocathodes, exceeding sensitivity of the best industrially made ones. Other photocathodes, Cs_3Sb and Na_2KSb were produced and investigated.

Ion-induced secondary electron emission (IISEE) from alkali-antimonide photocathodes

Alkali-antimonide photocathodes have low emission threshold; therefore, operating under gas avalanche, they are susceptible to ion-induced secondary-electron emission (IISEE), resulting in ion-feedback effects (secondary avalanches), imposing severe limits on the maximum reachable gains. Comprehensive studies of the photocathodes operation under gas-avalanche multiplication, performed in this work, yielded the absolute values of the IISEE coefficients (γ_+^{eff} = 0.02-0.03) for the three photocathode materials investigated. These permitted setting the necessary limits for the ion back-flow fraction (IBF) to the photocathode, necessary for a feedback-free operation at GPM gains of 10^5 (needed for single-photon sensitivity). The resulting estimated IBF-value for stable operation in a continuous mode in Ar/CH_4 (95/5) is $3.3 \cdot 10^{-4}$.

Electron multipliers with high ion-blocking capabilities

It was demonstrated (section 3.6) that the required IBF value of $3 \cdot 10^{-4}$ was reached with a three-element F-R-MHSP/GEM/MHSP cascaded electron multiplier operated in atmospheric-pressure Ar/CH_4 (95/5), at total gain of $\sim 10^5$. This record ion blocking, due to ion deflection by strip-electrodes patterned on hole-multipliers, was reached at full photoelectron collection efficiency. High gain continuous-mode operation of visible-sensitive GPMs.

This work proved for the first time, that a GPM with visible-sensitive bi-alkali photocathodes can be successfully operated in continuous mode, at gains suitable for single-photon imaging. A Visible-sensitive GPM with a F-R-MHSP/GEM/MHSP cascaded multiplier and a K_2CsSb photocathode, yielded, for the first time, stable operation at gains of 10^5 in continuous mode with full photoelectron collection efficiency and without any noticeable feedback effects. This validated our predicted necessary IBF values resulting from the IISEE measurements. The main goal of the research proposal - to combine thin-film photocathodes sensitive in visible-spectral range with fast cascaded micro-patterned gas avalanche multipliers sensitive to single charges - was therefore reached. This achievement can be considered as a major breakthrough in the field of photon detectors.

The GPM stability

A long-term stability under gas-avalanche conditions is naturally a concern for visible-sensitive GPMs. To avoid chemical degradation of the photocathodes, the detector components must be made of UHV-compatible materials; the detector must operate in sealed mode filled with an ultra-pure gase. In this work, the research has been carried out in difficult unsealed-detector conditions (detector placed within a large vacuum vessel). It was shown however that alkali-antimonide photocathodes are stable in ultra-pure gases for over two months period; by far better stability is expected in sealed devices. A deep concern was the photocathode's ageing under gas avalanche. Photocathode aging studies under avalanche-ion bombardment provided a basis for estimating the lifetime of visible-sensitive

GPMs combining a F-R-MHSP/GEM/MHSP multiplier and a K_2CsSb photocathode. Our calculations indicate that a detector of this type will have a 20% QE decrease of its bi-alkali photocathode after an accumulated ion- charge of 2 $\mu C/mm^2$; this will however occur after $\sim$40 years of constant operation under a gain of $\sim 10^5$ at a photon flux of 5 kHz/mm^2 (QE=30%). For comparison, in a GPM with 4-GEM multiplier (IBF$\sim 3 \cdot 10^{-2}$) for the same operation conditions, the 20% PC aging will occur after $\sim$150 days.

Further developments

The present work paves the way for further developments, towards the conception of sealed visible-sensitive GPMs, with flat geometry and area in the 100-1000 cm^2 ranges. They are expected to have several virtues: Fast photon imaging with single-photon sensitivity, large areas, operation under intense photon flux and at high magnetic fields. visible-sensitive GPMs have the potential of competing with vacuum photon detectors in many fields of applications, such as in imaging Cherenkov light in particle physics and astrophysics, in large-area neutrino detectors, in recording scintillation information in particle physics and medical imaging, etc. they might serve in advanced image intensifiers, etc. Though having lower quantum yields due to the backscattering effect in gas, visible-sensitive GPMs may compete with solid-state photon detectors in size and cost, in single-photon sensitivity and in noise characteristics.

The extension of the small-area laboratory visible-sensitive GPM prototype to large-area sealed devices is a technological challenge. While the production of large-area photocathodes and large-detector sealing has been mastered since long by industry, the production of large-area MHSP electrodes is yet to be demonstrated; progress in the production of large-area Micropattern gaseous detectors has been reached lately within the CERN-RD51 collaboration [123]. Efforts should be undertaken to develop such or similar patterned hole-multipliers made of inert insulating materials; among possible candidates are glass, ceramic and silicon [124]. Low-radioactivity substrate materials could be used in experiments aiming at the detection of rare events; among UHV-compatible polymers, a possible

candidate would be Cirlex [125], investigated for thick-GEM (THGEM [126]) multipliers.

The visible-sensitive GPM's multiplier's performance in terms of ion blocking could possibly be further improved, replacing the last MHSP stage by a MICROMEGAS element (see section 3.4.1). The latter would ease the GPM's signal recording for imaging purposes.

An optimization of the gas filling could also reduce secondary effects, e.g. the addition of low ionization potential admixtures like Ethyl Ferrocene (EF) or TMAE could considerably reduce ion feedback. It was shown [112] that in a GPM filled with He/CH_4 comprising a Cs_3Sb PC and a capillary-plate multiplier, an addition of EF vapor to the gas mixture improved the maximal achievable gain of the device.

Large-area GPMs have many potential applications, particularly in large particle physics and astrophysics experiments; among them are imaging Cherenkov light, recording scintillation information etc.; large-area photon detectors could be useful in medical imaging and in other fields.

List of publications resulting from this work

1. A. Lyashenko, A. Breskin, R. Chechik, J. M. F. Dos Santos, F. D. Amaro, J. F. C. A. Veloso, *Development of high-gain gaseous photomultipliers for the visible spectral range*, arXiv:0905.0170, accepted for publication in JINST.

2. A. Lyashenko, A. Breskin, R. Chechik and T.H.V.T. Dias, *Ion-induced secondary electron emission from K-Cs-Sb, Na-K-Sb and Cs-Sb photocathodes and its relevance to the operation of gaseous avalanche photomultipliers*, arXiv:0904.4881, submitted to the Journal of Applied Physics.

3. A. Lyashenko, A. Breskin, R. Chechik, J. M. F. Dos Santos, F. D. Amaro, J. F. C. A. Veloso, *Further progress in ion back-flow reduction with patterned gaseous hole-multipliers*, **JINST 2 (2007)P08004**.

4. A. Lyashenko, A. Breskin, R. Chechik, J. M. F. Dos Santos, F. D. Amaro, J. F. C. A. Veloso, *Avalanche-ion back-flow reduction in gaseous electron multipliers based on GEM/MHSP*, **JINST 1 (2006) P10004**.

5. A. Lyashenko, A. Breskin, R. Chechik, J. M. F. Dos Santos, F. D. Amaro, J. F. C. A. Veloso, *Efficient ion blocking in gaseous detectors and its application to gas-avalanche photomultipliers sensitive in the visible-light range*, **Nucl. Instr. and Meth. A 598 (2009) 116**. Proceedings to 10-th International Conference On Instrumentation For Colliding Beam Physics, Budker Institute of Nuclear Physics, Novosibirsk, Russia, February 28 - March 5, 2008.

6. A. Lyashenko, A. Breskin, R. Chechik, J. M. F. Dos Santos, F. D. Amaro, J. F.

C. A. Veloso, *High-gain DC-mode operated Gaseous Photomultipliers for the visible spectral range*, arXiv:0808.1556, **Nucl. Instr. and Meth. A (2009)** article in press, Proceedings to the 5th International Conference on New Developments In Photodetection 2008, Aix-les-Bains, France, June 15-20, 2008.

7. A. Breskin, A. Lyashenko, D. Mörmann, R. Chechik, F. D. Amaro, J. M. Maia, J. F. C. A. Veloso, J.M.F. dos Santos, *Ion-induced effects in GEM and GEM/MHSP gaseous photomultipliers for the UV and the visible spectral range*, **Nucl. Instr. and Meth. A 553 (2005) 46**.

8. J. F. C. A. Veloso, F. Amaro, J. M. Maia, A. Lyashenko, A. Breskin, R. Chechik, J. M. F. dos Santos, O. Bouianov, M. Bouianov, *MHSP in reversed-bias operation mode for ion blocking in gas-avalanche multipliers*, **Nucl. Instr. and Meth. A 548 (2005) 375**.

9. J. F. C. A. Veloso, F. D. Amaro, J. M. F. dos Santos, A. Breskin, A. Lyashenko, R. Chechik, *The Photon-Assisted Cascaded Electron Multiplier: a concept for potential avalanche-ion blocking*, **JINST 1 (2006) P08003**.

10. J. F. C. A. Veloso, F. D. Amaro, C. D. R. Azevedo, J. M. F. dos Santos, A. Breskin, A. Lyashenko and R. Chechik, *PACEM: a new concept for high avalanche-ion blocking*, **Nucl. Instr. and Meth. A 581 (2007) 261**.

11. F. D. Amaro, J. F. C. A. Veloso, J. M. F. dos Santos, A. Breskin, R. Chechik, and A. Lyashenko, *The Photon-Assisted Cascaded Electron Multiplier Operation in CF_4 for Ion Back-flow Suppression*, **IEEE Trans. Nucl. Sci., Vol. 55, No. 3 (2008) 1652**.

Bibliography

[1] S. Eisenhardt, Hybrid photon detectors for the LHCb RICH, Nucl. Instr. and Meth. A 565 (2006) 234.

[2] Z. Sadygov, et al., Three advanced designs of micro-pixel avalanche photodiodes:their present status, maximum possibilities and limitations, Nucl. Instr. and Meth. A 567 (2006) 70.

[3] D. Renker, Geiger-mode avalanche photodiodes, history, properties and problems, Nucl. Instr. and Meth. A 567 (2006) 48, Proceedings of the 4th International Conference on New Developments in Photodetection - BEAUNE 2005, Fourth International Conference on New Developments in Photodetection.

[4] R. Chechik, A. Breskin, Advances in gaseous photomultipliers, Nucl. Instr. and Meth. A 595 (2008) 116.

[5] F. Piuz, et al., The CsI-based ring imaging detector for the ALICE experiment: technical description of a large prototype, Nucl. Instr. and Meth. A 433 (1999) 222.

[6] Z. Fraenkel, et al., A hadron blind detector for the PHENIX experiment at RHIC, Nucl. Instr. and Meth. A 546 (2005) 466.

[7] B. Ketzer, Micropattern gaseous detectors in the COMPASS tracker, Nucl. Instr. and Meth. A 494 (2002) 142.

[8] L. Periale, et al., Photosensitive gaseous detectors for cryogenic temperature applications, Nucl. Instr. and Meth. A in press.

[9] E. Shefer, Study of novel stable photocathode materials for gaseous photon detectors in the near-UV to the visible spectral range, Ph.D. thesis, Weizmann Institute of Science, Israel .

[10] D. Mörmann, Study of novel gaseous photomultipliers for UV and visible light, PhD thesis, Weizmann Institute of Science, Israel .

[11] D. Mörmann, et al., GEM-based gaseous photomultipliers for UV and visible photon imaging, Nucl. Instr. and Meth. A 504 (2003) 93.

[12] J. M. F. Maia, et al., Avalanche-ion back-flow reduction in gaseous electron multipliers based on GEM/MHSP, Nucl. Instr. and Meth. A 523 (2004) 334.

[13] M. Balcerzyk, et al., Methods of preparation and performance of sealed gas photomultipliers for visible light, IEEE Trans. Nucl. Sci. 50 (2003) 847.

[14] H. Hertz, Üeber einen Einfluss des ultravioletten Lichtes auf die electrische Entladung, Annalen der Physik 267 (1887) 983.

[15] A. Einstein, Über einen die Erzeugung und Verwandlung des Lichtes betreffenden heuristischen Gesichtspunkt, Annalen der Physik 17 (1887) 132.

[16] E. Spicer, Photoemissive, photoconductive, and optical absorption studies of alkali-antimony compounds, Phys. Rev. 112 (1958) 114.

[17] A. H. Sommer, Photoemissive materials, Robert E. Krieger Publishing Company, 1980.

[18] I. E. Tamm, Phys. Z. Soviet Union 1 (1932) 733.

[19] R. Martinelli, Infrared photoemission from silicon, Appl. Phys. Lett. 16 (1970) 261.

[20] I. L. Krainsky, et al., Negative-electron-affinity effect on the surface of chemical-vapor-deposited diamond polycrystalline films, Phys. Rev. B 53 (1996) R7650.

[21] R. L. Bell, Negative Electron Affinity Devices, Clarendon Press, Oxford, 1973.

[22] M. Suyama, et al., A hybrid photodetector (HPD) with a III-V photocathode, IEEE Nuclear Science Symposium 1 (1997) 795.

[23] PMT handbook,(2009) Hamamatsu Photonics Inc., Japan.

[24] M. Hayashida, et al., Developement of HPD with an 18-mm-diameter GaAsP photocathode for the MAGIC-II, IEEE Nuclear Science Symposium 567 (2006) 180.

[25] E. Shefer, et al., Laboratory production of efficient alkali-antimonide photocathodes, Nucl. Instr. and Meth. A 411 (1998) 383.

[26] UBA (Ultra Bialkali), SBA (Super Bialkali) Photomultiplier Tube Series,(2009) Hamamatsu Photonics Inc., Japan.

[27] R. Engstrom, Photomultiplier handbook, RCA Corp., 1980.

[28] E. Shefer, et al., Coated photocathodes for visible photon imaging with gaseous photomultipliers, Nucl. Instr. and Meth. A 433 (1999) 502.

[29] I. Rodionov, et al., Hybrid gaseous photomultipliers, Nucl. Instr. and Meth. A 478 (2002) 384.

[30] D. Renker, New developments on photosensors for particle physics, Nucl. Instr. and Meth. A 598 (2009) 207, Instrumentation for Collding Beam Physics - Proceedings of the 10th International Conference on Instrumentation for Colliding Beam Physics.

[31] R. Grazioso, et al., APD arrays for scintillating fiber readout, IEEE Nuclear Science Symposium 2 (1999) 722.

[32] E. Lorenz, et al., Test of a scintillating fibre readout with avalanche photodiodes, Nucl. Instr. and Meth. A 504 (2003) 154.

[33] I. Britvitch, et al., Avalanche photodiodes now and possible developments, Nucl. Instr. and Meth. A 535 (2004) 523, Proceedings of the 10th International Vienna Conference on Instrumentation.

[34] V. N. Solovov, et al., Detection of scintillation light of liquid xenon with a LAAPD, IEEE Nuclear Science Symposium Conference Record 1 (2000) 58.

[35] L. M. P. Fernandes, et al., Behaviour of large-area avalanche photodiodes under intense magnetic fields for VUV- visible- and X-ray photon detection, Nucl. Instr. and Meth. A 498 (2002) 362.

[36] Y. Musienko, Advances in multipixel Geiger-mode avalanche photodiodes (silicon photomultiplies), Nucl. Instr. and Meth. A 598 (2009) 213, Instrumentation for Collding Beam Physics - Proceedings of the 10th International Conference on Instrumentation for Colliding Beam Physics.

[37] T. Aushev, et al., Scintillator strip detector with mrs apd readout for the super belle, Nucl. Instr. and Meth. A 581 (2007) 447, VCI 2007 - Proceedings of the 11th International Vienna Conference on Instrumentation.

[38] D. Bailleux, et al., Hamamatsu APD for CMS ECAL: quality insurance, Nucl. Instr. and Meth. A 518 (2004) 622, Frontier Detectors for Frontier Physics: Proceedin.

[39] A. Biland, et al., First detection of air shower Cherenkov light by Geigermode-Avalanche Photodiodes, Nucl. Instr. and Meth. A 595 (2008) 165, RICH 2007 - Proceedings of the Sixth International Workshop on Ring Imaging Cherenkov Detectors.

[40] K. Föhl, et al., The DIRC detectors of the PANDA experiment at FAIR, Nucl. Instr. and Meth. A 595 (2008) 88, RICH 2007 - Proceedings of the Sixth International Workshop on Ring Imaging Cherenkov Detectors.

[41] T. Iijima, Development of RICH counters towards the KEKB/Belle upgrade, Nucl. Instr. and Meth. A 598 (2009) 138, Instrumentation for Collding Beam Physics -

Proceedings of the 10th International Conference on Instrumentation for Colliding Beam Physics.

[42] C. Damiani, et al., Magnetic field effects on Hybrid PhotoDiode single electron response, Nucl. Instr. and Meth. A 442 (2000) 136.

[43] E. Albrecht, et al., Performance of hybrid photon detector prototypes with 80 percent active area for the rich counters of LHCB, Nucl. Instr. and Meth. A 442 (2000) 164.

[44] A. Braem, et al., Novel design of a parallax free compton enhanced PET scanner, Nucl. Instr. and Meth. A 525 (2004) 268.

[45] A. Braem, et al., A large spherical HPD for a novel deep-sea neutrino experiment, Nucl. Instr. and Meth. A 553 (2005) 85.

[46] F. Sauli, Principles of operation of multiwire, proportional and drift chambers, Geneva, 1977.

[47] G. P. Guedes, et al., Two-dimensional GEM imaging detector with delay-line readout, Nucl. Instr. and Meth. A 513 (2003) 473.

[48] M. Killenberg, et al., Charge transfer and charge broadening of GEM structures in high magnetic fields, Nucl. Instr. and Meth. A 530 (2004) 251.

[49] S. Lotze, et al., Charge transfer of GEM structures in high magnetic fields, Nucl. Phys. B (Proc. Suppl.) 150 (2006) 155.

[50] R. A. Wijsman, et al., Breakdown probability of a low pressure gas discharge, Phys. Rev. 75 (1948) 833.

[51] N. Arley, Stochastic processes and cosmic radiation, John Wiley & sons Inc., New York, 1948.

[52] B. Singh, et al., CsBr and CsI UV photocathodes: new results on quantum efficiency and aging, Nucl. Instr. and Meth. A 454 (2004) 364.

[53] G. Charpak, et al., The use of mutiwire proportional counters to select and localize charged particles, Nucl. Instr. and Meth. A 62 (1968) 262.

[54] F. Piuz, CsI-photocathode and RICH detector, Nucl. Instr. and Meth. A 371 (1996) 96.

[55] E. Nappi, Trends in the development of large area photon detectors for Cherenkov light imaging applications, Nucl. Instr. and Meth. A 504 (2003) 70.

[56] M. Artuso, The ring imaging detector for CLEO III, Nucl. Instr. and Meth. A 371 (1996) 324.

[57] F. Piuz, Ring Imaging Cherenkov systems based on gaseous photo-detectors: trends and limits around particle accelerators, Nucl. Instr. and Meth. A 502 (2003) 76.

[58] Y. Giomataris, et al., MICROMEGAS: a high-granularity position-sensitive gaseous detector for high particle-flux environments, Nucl. Instr. and Meth. A 376 (1996) 29.

[59] J. Derré, et al., Fast signals and single electron detection with a MICROMEGAS photodetector, Nucl. Instr. and Meth. A 449 (2000) 314.

[60] J. Derré, et al., Recent experimental results with MICROMEGAS, Nucl. Instr. and Meth. A 477 (2002) 23.

[61] S. Anvar, et al., Large bulk MICROMEGAS detectors for TPC application, Nucl. Instr. and Meth. A article in press.

[62] S. Platchkov, et al., Large bulk MICROMEGAS detectors for TPC application, IEEE Nuclear Science Symposium Conference Record 1 (2002) 292.

[63] P. Colas, et al., Ion backflow in the MICROMEGAS TPC for the future linear collider, Nucl. Instr. and Meth. A 535 (2004) 226.

[64] F. Sauli, GEM: A new concept for electron amplification in gas detectors, Nucl. Instr. and Meth. A 386 (1997) 531.

[65] M. Titov, New developments and future perspectives of gaseous detectors, Nucl. Instr. and Meth. A 581 (2007) 25.

[66] A. Buzulutskov, et al., The GEM photomultiplier operated with noble gas mixtures, Nucl. Instr. and Meth. A 443 (2000) 164.

[67] D. Mörmann, et al., Operation principles and properties of the multi-GEM gaseous photomultiplier with reflective photocathode, Nucl. Instr. and Meth. A 530 (2004) 258.

[68] C. Richter, et al., Absolute electron transfer efficiency of GEM, Nucl. Instr. and Meth. A 461 (2001) 308.

[69] C. Richter, et al., On the efficient electron transfer through GEM, Nucl. Instr. and Meth. A 478 (2002) 538.

[70] F. Sauli, Novel cherenkov photon detectors, Nucl. Instr. and Meth. A 553 (2005) 18.

[71] I. Tserruya, et al., Development of a triple GEM UV-photon detector operated in pure CF_4 for the PHENIX experiment, Nucl. Instr. and Meth. A 523 (2004) 345.

[72] J. F. C. A. Veloso, et al., Micromegas, a multipurpose gaseous detector, Rev. Sci. Inst. A 71 (2000) 2371.

[73] J. Escada, et al., A Monte Carlo study of backscattering effects in the photoelectron emission from CsI into CH_4 and Ar-CH_4 mixtures, JINST 2 (2007) P08001.

[74] A. D. Mauro, et al., Photoelectron backscattering effects in photoemission from CsI into gas media, Nucl. Instr. and Meth. A 371 (1996) 137.

[75] M. Kaminsky, Atomic and ionic impact phenomena on metal surfaces, Springer Verlag, 1965.

[76] A. Breskin, et al., Ion-induced effects in GEM and GEM/MHSP gaseous photomultipliers for the UV and the visible spectral range, Nucl. Instr. and Meth. A 553 (2005) 46 and references therein.

[77] R. Chechik, et al., Progress in GEM-based gaseous photomultipliers, Nucl. Instr. and Meth. A 502 (2003) 195.

[78] D. Mörmann, et al., Evaluation and reduction of ion back-flow in multi-GEM detectors, Nucl. Instr. and Meth. A 516 (2004) 315.

[79] M. A. Biondi, L. M. Chanin, Mobilities of atomic and molecular ions in the noble gases, Phys. Rev. 94 (1954) 910.

[80] J. J. Lowke, J. James H. Parker, Theory of electron diffusion parallel to electric fields. II. application to real gases, Phys. Rev. 181 (1968) 302.

[81] C. Lakashminarasimha, J. Lucas, The ratio of radial diffusion coefficient to mobility for electrons in helium, argon, air, methane and nitric oxide, J. Phys. D: Appl. Phys. 10 (1977) 313.

[82] G. Seikora, et al., Transverse diffusion of Ar_+ and Ar_{2+} in Ar, Phys. Rev. A 29 (1984) 3379.

[83] A. Bondar, et al., Study of ion feedback in multi-GEM structures, Nucl. Instr. and Meth. A 496 (2003) 325.

[84] S. Bachmann, et al., Charge amplification and transfer processes in the gas electron multiplier, Nucl. Instr. and Meth. A 438 (1999) 376.

[85] R. Chechik, et al., Recent investigations of cascaded GEM and MHSP detectors, IEEE Trans. Nucl. Sci. 51 (2004) 2097.

[86] P. Némethy, et al., Gated time projection chamber, Nucl. Instr. and Meth. A 212 (1983) 273.

[87] A. Breskin, CsI UV photocathodes: history and mystery, Nucl. Instr. and Meth. A 371 (1996) 116.

[88] A. Braem, et al., Aging of large-area CsI photocathodes for the ALICE HMPID prototypes, Nucl. Instr. and Meth. A 515 (2003) 307.

[89] A. Breskin, et al., GEM photomultiplier operation in CF_4, Nucl. Instr. and Meth. A 483 (2002) 670.

[90] H. Raether, Electron avalanches and breakdown in gases, Butterworths, London, 1964.

[91] H. Hagstrum, Theory of Auger neutralization of ions at the surface of a diamond-type semiconductor, Phys. Rev. 122 (1961) 83.

[92] Y. Takeshi, Ejection of electrons from barium oxide by noble gas ions, J. Phys. Soc. Japan 17 (1962) 326.

[93] R. J. Mohr, et al., Pure and binary gas adsorption equilibria and kinetics of Methane and Nitrogen on 4A Zeolite by Isotope Exchange Technique, J. Phys.: Condens. Matter 5 (2) (1999) 145.

[94] A. R. H. F. Ettema, R. A. Groot, Electronic structure of Cs_2kSb and k_2CsSb, Phys. Rev. B 66 (2002) 115102.

[95] D. Motta, et al., Optical properties of bialkali photocathodes, Nucl. Instr. and Meth. A 539 (2005) 217.

[96] A. R. H. F. Ettema, R. A. Groot, Electronic structure of Na_3k and Na_2kSb, Phys. Rev. B 61 (2000) 10035.

[97] A. Ebina, T. Takahashi, Transmittance spectra and optical constants of alkali-antimony compounds K_3Sb, Na_3Sb, and Na_2KSb, Phys. Rev. B 7 (1973) 4712.

[98] S.-H. Wei, A. Zunger, Electronic structure of M_3^iSb-type filled tetrahedral semiconductors, Phys. Rev. B 35 (1986) 3952.

[99] M. Tezge, J. Hafner, Electronic structure of alkali-pnictide compounds, J. Phys.: Condens. Matter 4 (1992) 2449.

[100] J. K. Theobald, Investigation of back diffusion of photoelectrons in various standard gases as it affects secondary electron emission coefficients, J. Appl. Phys. 24 (1953) 123.

[101] O. Sahi, C. Lanza, Importance of the dependence of the secondary electron emission coefficient on E/p_0 for Paschen breakdown curves in ac plasma panels, J. Appl. Phys. 47 (1976) 1337.

[102] U. Becker, et al., Gas R&D Home Page .

[103] D. S. Burch, J. H. Whealton, Monte Carlo calculation of electron back diffusion in a Townsend discharge, J. Appl. Phys. 48 (6) (1977) 2213.

[104] A. A. Sebastian, J. M. Wadehra, Time-dependent behaviour of electron transport in methaneargon mixtures, J. Phys. D: Appl. Phys. 38 (2005) 1577.

[105] R. Nathan, C. H. B. Mee, The energy distribution of photoelectrons from the K_2CsSb photocathode, phys. stat. sol. (a) 2 (1970) 67.

[106] L. C. C. Coelho, et al., Measurement of the photoelectron-collection efficiency in noble gases and methane, Nucl. Instr. and Meth. A 581 (2007) 190.

[107] V. Peskov, Instr. Exp. Tech. 23 (1980) 507.

[108] G. Charpak, et al., Detection of far-ultraviolet photons with the multistep avalanche chamber. application to cherenkov light imaging and to some problems in high-energy physics, Nucl. Instr. and Meth. A 164 (1979) 419.

[109] D. Anderson, A xenon gas scintillation proportional counter coupled to a photoionization detector, Nucl. Instr. and Meth. A 178 (1980) 125.

[110] G. Charpak, et al., Ethyl ferrocene in gas, condensed, or adsorbed phases: three types of photosensitive elements for use in gaseous detectors, Nucl. Instr. and Meth. A 277 (1989) 537.

[111] G. Charpak, et al., Some studies of the applications of csi photocathodes in gaseous detectors, Nucl. Instr. and Meth. A 333 (1993) 391.

[112] V. Biteman, et al., Position sensitive gaseous photomultipliers, Nucl. Instr. and Meth. A 471 (2001) 205.

[113] The cross sections used by Magboltz 7.1 software .

[114] T. H. V. T. Dias, et al., Measurement of the photoelectron-collection efficiency in noble gases and methane, J. Phys. D: Appl. Phys. 37 (2004) 540.

[115] S. Roth, et al., Charge transfer of GEM structures in high magnetic fields, Nucl. Instr. and Meth. A 535 (2004) 330.

[116] J. F. C. A. Veloso, et al., Recent advances in X-ray detection with micro-hole and strip plate detector, Nucl. Instr. and Meth. A 524 (2004) 124.

[117] A. Lyashenko, et al., Avalanche-ion back-flow reduction in gaseous electron multipliers based on GEM/MHSP, JINST 1 (2006) P10004.

[118] C. Shalem, et al., Advances in thick GEM-like gaseous electron multiplierspart i: atmospheric pressure operation, Nucl. Instr. and Meth. A 558 (2006) 475.

[119] F. Sauli, et al., Electron Collection and Ion Feedback in GEM-Based Detectors, IEEE Trans. Nucl. Sci. 50 (2003) 803.

[120] L. B. Loeb, J. M. Meek, The Mechanism of Spark Discharge in Air at Atmospheric Pressure. I, J. Appl. Phys. 11 (1940) 438.

[121] S. Ahn, et al., GEM-type detectors using LIGA and etchable glass technologies, Lawrence Berkeley National Laboratory Paper LBNL-47782.

[122] B. Azmoun, et al., A study of gain stability and charging effects in GEM foils, IEEE Nuclear Science Symposium Conference Record 6 (2006) 3847.

[123] R. de Oliveira, Recent achievements and projects in Large MPGDs http://indico.cern.ch/getfile.py/access?contribid=0&resid=1&materialid=slides&confid=47406, Talk given at the 2nd RD-51 Collaboration Meeting .

[124] A. Breskin, et al., Recent advances in gaseous imaging photomultipliers, Nucl. Instr. and Meth. A 513 (2003) 250.

[125] M. Gai, et al., Toward Application of a Thick Gas Electron Multiplier (THGEM) Readout for a Dark Matter Detector .

[126] A. Breskin, et al., A concise review on THGEM detectors, Nucl. Instr. and Meth. A 598 (2009) 107.